Quantifying and Scaling Airplane Performance in Turbulence

by

Johnhenri R. Richardson

A dissertation submitted in partial fulfillment
of the requirements for the degree of
Doctor of Philosophy
(Applied Physics)
in the University of Michigan
2013

Doctoral Committee:

Associate Professor Ella M. Atkins, Co-Chair
Associate Professor Anouck R. Girard, Co-Chair
Professor Pierre T. Kabamba, Co-Chair
Professor Çagliyan Kurdak
Professor N. Harris McClamroch

An encounter with stochastic gusts

For my parents

ACKNOWLEDGEMENTS

First and foremost, thank you to Professors Anouck Girard, Ella Atkins, and Pierre Kabamba. Your guidance was instrumental to the success of this work and your mentoring was invaluable to my personal and professional growth. I truly enjoyed our collaborative advising arrangement and learned so much from the three very different perspectives you brought to our discussions. To my other committee members, thank you to Professor McClamroch. Your textbook provided the foundation upon which I built an understanding of the physics of airplane flight. Also, thank you to Professor Kurdak for your leadership in the Applied Physics Program, including agreeing to serve on my committee.

Thank you to my fellow members of the ARC Lab. We have done great work together, had a lot of fun, and shared in each other's experiences. In particular, thank you to Ricardo Bencatel, Zahid Hasan, Baro Hyun, Jonathan Las Fargeas, Moritz Niendorf, Christopher Orlowski, Dave Oyler, Weilin Wang, Jonathan White, Weijia Zhang, and Jinxin Zhao for your collaboration and camaraderie. Thank you to my officemates Justin Jackson and Susanta Ghosh for helping me work through some of the challenges I encountered along the way. Thank you to the staff in the Applied Physics Program, Department of Aerospace Engineering, and Rackham Graduate School for facilitating my studies. Also, thank you to the editors and reviewers of my articles. While I did not always appreciate your comments upon receiving them, they led to substantial improvements in my work.

Several institutions sponsored my graduate education and research. In decreasing

order of contributions, thank you to the Army Research Office, the Rackham Graduate School, the Department of Aerospace Engineering, the Air Force Office of Scientific Research, the Air Force Research Laboratory, the Applied Physics Program, and the Civil Air Patrol.

Thank you to all of the friends I made during my time in Ann Arbor, whether fellow students, roommates, Civil Air Patrol members, or the rest. You have supported me, entertained me, and taught me quite a bit on top of what I learned in school. Completing this research would not have been possible without the enjoyable life you created for me outside of my studies.

Finally, thank you to my family, especially my parents Leslie and Rudy. Your loving support has been and will continue to be the most important factor in my accomplishments.

TABLE OF CONTENTS

LIST OF FIGURES

Figure

LIST OF TABLES

Table

LIST OF APPENDICES

Appendix

LIST OF SYMBOLS

Symbol

$\mathbb{1}_n$	Identity matrix of dimension n
A	State matrix of Eq. (3.33)
A_{CL}	State matrix of the closed-loop dynamics of Eq. (3.39)
A_p	State matrix of the phugoid dynamics of Eq. (4.3)
$A_{v_{wx}}$	Sub-matrix of A_w corresponding to the longitudinal velocity component
A_w	State matrix of the gusts' coloring filter
B	Input matrix of Eq. (3.33)
$B_{v_{wx}}$	Sub-matrix of B_w corresponding to the longitudinal velocity component
E_w	Input matrix of the gusts' coloring filter
c	Control input vector
$\bar{c}$	Wing chord length
C_{CL}	Output matrix of the closed-loop dynamics of Eq. (3.39)
C_D	Drag coefficient
C_L	Lift coefficient
C_{L_0}	Zero angle of attack lift coefficient
C_{L_α}	Gradient of lift coefficient with respect to angle of attack
C_{meas}	Output matrix of Eq. (3.37) for feedback control measurements
C_{PCL}	Output matrix used to compute P in the closed-loop case
C_{POL}	Output matrix used to compute P in the open-loop case
$C_{v_{wx}}$	Sub-matrix of C_w corresponding to the longitudinal velocity component
C_w	Output matrix of the gusts' coloring filter, $\begin{pmatrix} C_{wv} & C_{w\omega} \end{pmatrix}^{\text{T}}$
C_{wv}	Terms of C_w that correspond to δv_w
D	Covariance matrix of the noise input $d(t)$
$d(t)$	White noise with distribution $\mathcal{N}(0, D)$ that drives the gusts' coloring filter
$\mathcal{E}$	Nonlinear function for $\dot{\epsilon}$ as a function of ω and ϵ
E	Disturbance input matrix of Eq. (3.33)
e	Oswald efficiency factor
E_{CL}	Disturbance input matrix of the closed-loop dynamics of Eq. (3.39)
E_p	Disturbance input matrix of the phugoig dynamics of Eq. (4.3)
F_a	Sum of the forces acting on the airplane that depend on the relative wind linear and angular velocities, i.e., aerodynamic forces
F_D	Magnitude of the force of drag
F_g	Gravitational force acting on the airplane

F_L	Magnitude of the force of lift
F_0	Sum of the forces acting on the airplane that neither depend on the relative wind nor are gravitational
g	Standard acceleration due to free fall
h	Angular momentum of the airplane
$H_\times$	Skew-symmetric matrix formed from h, see Eq. (3.9)
I	Moment of inertia matrix of the airplane
L_u	Characteristic length in the longitudinal turbulence power spectral density
m	Mass of the airplane
M_a	Sum of the moments acting on the airplane that depend on the relative wind linear and angular velocities, i.e., aerodynamic moments
M_0	Sum of the moments acting on the airplane that do not depend on the relative wind
N	Airplane length scale factor where the scale model's length is N times the full size airplane's
n	Normal load factor, $\frac{F_L}{mg}$
$n_{\max}$	Maximum load factor for safe airplane operation
$\mathcal{N}(\mu, \Sigma)$	Normal distribution with mean μ and covariance matrix Σ
P	Covariance matrix of $\begin{pmatrix}\delta v_t & \delta\alpha & \delta n\end{pmatrix}^{\mathrm{T}}$
P_{CL}	Covariance matrix of the state vector of the closed-loop dynamics of Eq. (3.39)
P_{OL}	Covariance matrix of the state vector in Eq. (3.33)
Q	Positive semidefinite weight matrix penalizing state deviations for the linear-quadratic regulator
q	Norm of Q
R	Positive definite weight matrix penalizing control deviations for the linear-quadratic regulator
S	Wing planform area
S_{meas}	Covariance matrix of the measurement noise $s(t)$
$s(t)$	Measurement noise with distribution $\mathcal{N}(0, S_{\mathrm{meas}})$
V	Magnitude of v_c
v_c	Center of mass velocity of the airplane, $\begin{pmatrix}u & v & w\end{pmatrix}^{\mathrm{T}}$
$V_{c\times}$	Skew-symmetric matrix formed from v_c, see Eq. (3.9)
v_t	True airspeed
v_w	Velocity of the wind relative to the inertial reference frame, $\begin{pmatrix}v_{wx} & v_{wy} & v_{wz}\end{pmatrix}^{\mathrm{T}}$
δv_{wx}	Longitudinal component of the wind disturbance
x	State vector of Eq. (3.33)
$\hat{x}$	Estimate of the state vector x
x_p	State vector of the phugoid dynamics of Eq. (4.3)
x_{des}	Desired state, used as an input for feedback control
y_{meas}	Output vector of the open-loop system
α	Angle of attack
γ	Flight path angle
δ_a	Perturbation of the aileron control input
δc	Perturbation of c, $\begin{pmatrix}\delta_a & \delta_e & \delta_r\end{pmatrix}^{\mathrm{T}}$

δ_e	Perturbation of the elevator control input
δF_a	Perturbation of F_a after perturbing wind
δF_L	Perturbation of F_L after perturbing wind
δF_g	Perturbation of F_g after perturbing wind
δM_a	Perturbation of M_a after perturbing wind
δn	Perturbation of n after perturbing wind
δ_r	Perturbation of the rudder control input
δv_c	Perturbation of v_c after perturbing wind
δv_{meas}	Measured velocity perturbation
δv_t	Perturbation of v_t after perturbing wind
δv_t^2	Perturbation of v_t^2 after perturbing wind
δv_w	Perturbation of the wind velocity
$\delta\epsilon$	Perturbation of ϵ after perturbing wind
$\delta\omega$	Perturbation of ω after perturbing wind
$\delta\omega_{\text{meas}}$	Measured angular velocity perturbation
$\delta\omega_w$	Perturbation of the wind angular velocity
$\delta\Omega_\times$	Skew-symmetric matrix formed from $\delta\omega$, see Eq. (3.9)
ϵ	Vector comprised of the roll and pitch Euler angles, $\begin{pmatrix}\phi & \theta\end{pmatrix}^{\mathrm{T}}$
ζ_p	Damping ratio of the phugoid mode
κ	Relative frequency of the airplane phugoid mode to the turbulence
$\hat{\mu}$	Logarithmic residence time
μ	Bank angle around the velocity vector
ξ_w	State vector of the gusts' coloring filter
$\xi_{v_{wx}}$	State variable of the gusts' coloring filter corresponding to the longitudinal velocity component
ρ	Air density
$\rho_{\text{A/C}}$	Density of the airplane
σ_n^2	Variance of the normal load factor
σ_u	Intensity of the longitudinal turbulence
$\sigma_{v_t}^2$	Variance of the true airspeed
σ_α^2	Variance of the angle of attack
Φ	Matrix transforming the angular velocity into the Euler rates
$\Omega_\times$	Skew-symmetric matrix formed from ω, see Eq. (3.9)
$\tilde{\Omega}_\times$	Skew-symmetric matrix formed from $\omega + \delta\omega$, see Eq. (3.9)
ω	Angular velocity of the airplane around its center of mass, $\begin{pmatrix}p & q & r\end{pmatrix}^{\mathrm{T}}$
ω_{np}	Natural frequency of the phugoid mode
ω_w	Angular velocity of the wind relative to the inertial reference frame, $\begin{pmatrix}p_w & q_w & r_w\end{pmatrix}^{\mathrm{T}}$

ABSTRACT

Quantifying and Scaling Airplane Performance in Turbulence

by

Johnhenri R. Richardson

Co-Chairs: Ella M. Atkins, Anouck R. Girard, and Pierre T. Kabamba

This dissertation studies the effects of turbulent wind on airplane airspeed and normal load factor, determining how these effects scale with airplane size and developing envelopes to account for them. The results have applications in design and control of aircraft, especially small scale aircraft, for robustness with respect to turbulence. Using linearized airplane dynamics and the Dryden gust model, this dissertation presents analytical and numerical scaling laws for airplane performance in gusts, safety margins that guarantee, with specified probability and logarithmic residence time, that steady flight can be maintained when stochastic wind gusts act upon an airplane, and envelopes to visualize these safety margins.

Presented here for the first time are scaling laws for the phugoid natural frequency, phugoid damping ratio, airspeed variance in turbulence, and flight path angle variance in turbulence. The results show that small aircraft are more susceptible to high frequency gusts, that the phugoid damping ratio does not depend directly on airplane size, that the airspeed and flight path angle variances can be parameterized by the ratio of the phugoid natural frequency to a characteristic turbulence frequency, and

that the coefficient of variation of the airspeed decreases with increasing airplane size. Accompanying numerical examples validate the results using eleven different airplanes models, focusing on NASA's hypothetical Boeing 757 analog the Generic Transport Model and its operational 5.5% scale model, the NASA T2.

Also presented here for the first time are stationary flight, where the flight state is a stationary random process, and the stationary flight envelope, an adjusted steady flight envelope to visualize safety margins for stationary flight. The dissertation shows that driving the linearized airplane equations of motion with stationary, stochastic gusts results in stationary flight. It also shows how feedback control can enlarge the stationary flight envelope by alleviating gust loads, though the enlargement is significantly limited by control surface saturation. The results end with a numerical example of a Navion general aviation aircraft performing various steady flight maneuvers in moderate turbulence, showing substantial reductions in the steady flight envelope for some combinations of maneuvers, turbulence, and safety margins.

CHAPTER I

Introduction

1.1 Motivation

Turbulence is a common factor in airplane accidents. In a review of over 4,000 reports on weather-related accidents between 1992 and 2001, 509, or 12%, listed weather-related turbulence as a cause or contributing factor [1]. In particular, loss of control in-flight is often associated with wind gusts, including turbulence. Among 126 loss of control accidents that occurred between 1979 and 2009, 14% listed wind shear, turbulence, or thunderstorms as a cause or contributing factor [2]. Loss of control in-flight is itself a leading cause of aviation accidents. In the years 2000–2009, 20 out of 89 investigated commercial jet accidents, or 22%, had loss of control in-flight identified as the primary cause [3]. An example from 2010 illustrates turbulence leading to an upset, loss of control, and ultimately an accident. According to the investigation, the autopilot of a Cirrus SR22 disengaged during a turbulent approach upon coming dangerously close to stalling. The pilot could not maintain control and ultimately deployed a parachute to slow the airplane's uncontrolled descent [4].

In addition to loss of control in-flight, turbulence contributes to accidents by causing substantial damage to aircraft and injuries to crew and passengers, sometimes fatal. In the same report on turbulence-related accidents, among air carriers, all but one of the 72 turbulence-related accidents caused "serious injuries" [1], but this

statistic is misleading because air carriers do not usually report accidents causing only minor injuries and do not usually suffer turbulence-related accidents causing substantial damage to the airplane but only minor injuries to passengers. However, for general aviation aircraft, the same report on weather-related accidents categorized turbulence-related accidents by severity of damage and injury. The review shows that for turbulence-related general aviation aircraft accidents, 98% resulted in "substantial damage" to or destruction of the aircraft, and 42% resulted in "serious injuries" or fatalities [1]. In many cases, turbulence damages the airplane directly by excessively loading the airframe. In a 2006 accident, an Aero Commander 690A broke up during cruise after encountering moderate turbulence [5].

This last statistic suggests the first aspect of turbulence-related accidents that this dissertation will address: the effects of turbulence on aircraft differ greatly based on aircraft size. To see this, we can normalize the number of turbulence-related accidents between 1992–2001 from the same report [1] by the total number of hours flown by air carriers and general aviation aircraft. Since the 2001 flight hours are readily available for air carriers [6] and general aviation aircraft [7], but the hours for the entire ten year period are not, we use ten times the 2001 flight hours for the normalization. Air carriers have a turbulence-related accident rate of 1.25×10^{-5} turbulence-related accidents per flight hour, while general aviation aircraft and air taxis have a rate of 1.41×10^{-3} turbulence-related accidents per flight hour, two orders of magnitude larger. While other factors besides size undoubtedly factor into this much higher turbulence accident rate among light aircraft, for example pilot proficiency and underreporting of general aviation flight hours, this dissertation shows how aircraft performance may explain this difference.

As shown in Chap. III, turbulence can be modeled as a disturbance in the airplane equations of motion, and the standard deviation of an airplane's airspeed can be computed based on the statistics of the turbulence. Dividing that standard devi-

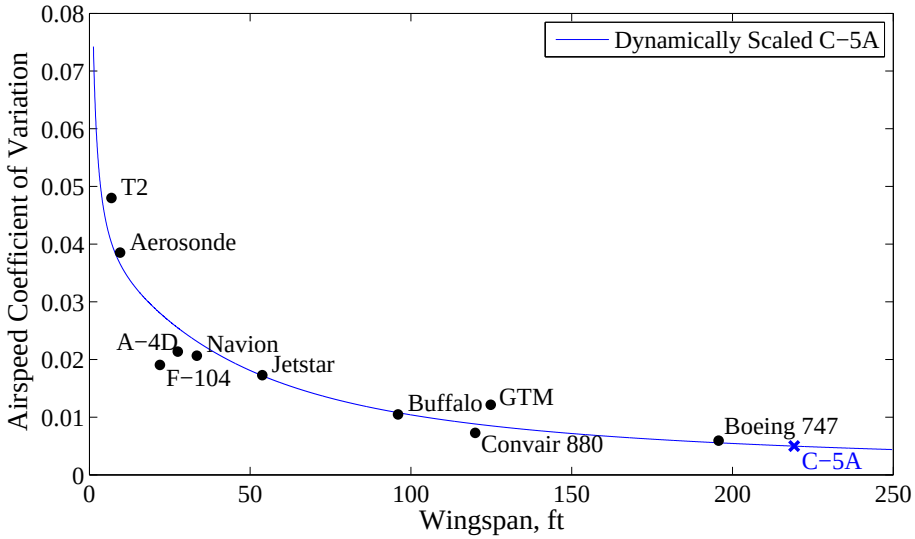

Figure 1.1: Plot of the dynamically scaled airspeed coefficient of variation versus wingspan. The corresponding values for the NASA GTM and T2 aircraft are marked.

ation by the average airspeed gives the airspeed coefficient of variation, a normalized measure of uncertainty in the airspeed. Figure 1.1 shows that the airspeed coefficient of variation for an airplane in moderate turbulence decreases with increasing airplane size, measured in this example by wingspan. The airplane scaled for this example is the Lockheed C-5A. Chapter IV explains dynamic scaling, but in essence the curve represents the performance of the C-5A if its wingspan were changed but its other dimensions, its weight, and its airspeed remained constant relative to the wingspan. Also marked on the figure are the coefficients of variation for ten other aircraft of various sizes. The figure is described in detail in Section 4.4, but the result is intuitive: the fractional change in airspeed due to turbulence is larger for small aircraft, in particular because larger aircraft tend to cruise at faster airspeeds.

The airplanes with the smallest wingspans in Fig. 1.1 are smaller than general aviation aircraft. A growing fleet of unmanned aircraft systems (UAS) can benefit from modeling of gust effects. By early 2010, the U.S. military had acquired more than 6,100 unmanned aircraft that each weighed 20 lbs or less [8]. Moreover, the U.S.

military classifies unmanned aerial vehicles over 5,000 lbs as "large" [9], while the Federal Aviation Administration (FAA) wake turbulence classifications designate airplanes lighter than 41,000 lbs as "small" [10]. Many of these aircraft utilize autopilots that rely on mathematical models of the airplane's dynamics and performance, much like the autopilot in the Cirrus SR22 accident described earlier. Nonmilitary use of UASs is not as well developed, but a wide range of potential civil and commercial applications of UASs have been identified. Examples include border and coastal patrol, fire detection and firefighting management, and ground transportation monitoring and control [11, 12].

When the airspeed changes due to turbulence, as demonstrated by Fig. 1.1, airplane upsets and flight envelope departures mentioned earlier can result. In the study of 126 loss of control accidents, investigations listed "stall/departure", meaning an excursion out of the flight envelope, as a causal or contributing factor in 49 cases, or 39%. Furthermore, 86% of accidents initiated by atmospheric disturbances led to an upset flight condition, of which stall/departure is the most common. 64% of these accidents also involved inappropriate crew response [2].

The flight envelope, the set of speeds, altitudes, flight path angles, and bank angles at which an airplane can maintain steady flight, is a useful tool in identifying when an airplane is prone to loss of control. The boundaries of the flight envelope are computed based on constraints limiting steady flight, namely maximum engine output, maximum angle of attack, and maximum normal load factor. Steady flight, where the airplane's linear and angular velocity vector components are constant in the body frame, is not conducive to loss of control because most airplanes are designed to fly stably or stabilizably when flying steadily. Nevertheless, models of steady flight assume nominal conditions that cannot be expected in turbulence. To cope with this environmental uncertainty, pilots are trained to fly more conservatively in turbulence than under nominal conditions, well within the steady flight envelope.

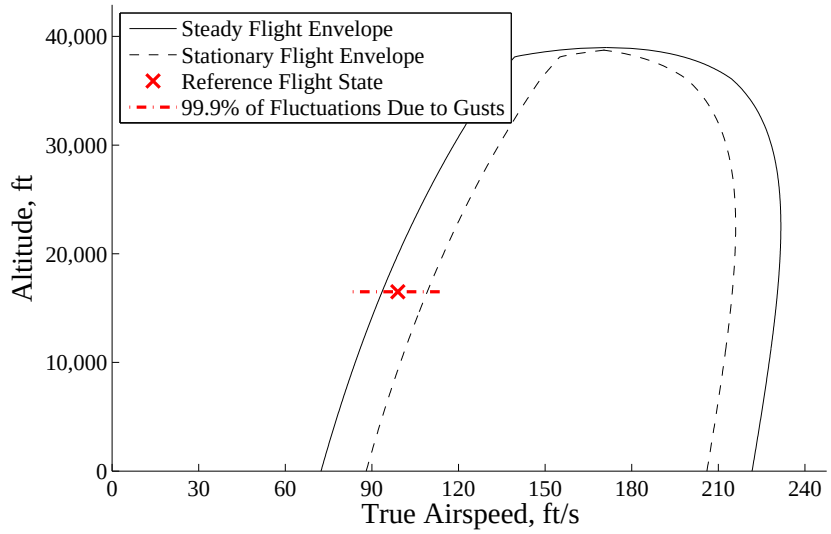

Figure 1.2: Illustration of the steady and stationary flight envelopes for an airplane flying through turbulence.

Consider an airplane operating at a low-speed condition close to stall. For example, the airplane might be climbing just after takeoff or on approach to land. If that airplane encountered turbulence, the airspeed and angle of attack would fluctuate. Under some circumstances, the airspeed could fluctuate below the stall speed, as depicted in Fig. 1.2. The figure shows a hypothetical case where turbulence causes fluctuations in airplane airspeed with a standard deviation of 10 ft/s. The dash-dot line shows three standard deviations worth of fluctuations around the steady flight state. Operating within the stationary flight envelope would ensure that the stall speed remained at least three standard deviations below the steady flight state, or that the airplane's airspeed remained above the stall speed 99.87% of the time, assuming a Gaussian distribution on the airspeed fluctuations. The stationary flight envelope is described in detail in Section 5.3.

The aim of this work is to provide new insight and modeling for airplane dynamic response to stochastic gusts in an effort to make airplanes, especially small airplanes, more robust with respect to turbulence. This aim is accomplished by quantifying

airplane performance in turbulence, by exploring how airplane performance in turbulence scales with airplane size, and by providing tools to help clarify the boundaries of the flight envelope under uncertain wind conditions. These tools can be used in design and control of airplanes, especially small, potentially unmanned airplanes, to better understand airplane capabilities and safe operating conditions in an uncertain environment.

1.2 Problem Statement & Technical Approach

This dissertation addresses the problem of quantifying airplane performance in stochastic gusts. Specifically, given an airplane, a desired steady flight state, and a turbulence intensity, this dissertation shows how to:

- Compute the variances of the airspeed and normal load factor
- Dynamically scale the airspeed variance for one aircraft to a geometrically similar aircraft of a different size
- Define safety margins using the variances of the airspeed and normal load factor
- Draw new flight envelopes that incorporate these safety margins

The problem is framed by driving airplane equations of motion with a stochastic wind disturbance and then computing the variances of the true airspeed and normal load factor. These two variances quantify the airplane's performance relative to a reference steady flight state. For the airplane equations of motion, this work uses linearized dynamics where the state variables are the airplane linear and angular velocity body frame components and the roll and pitch Euler angles. The inputs to these linearized dynamics are wind gust linear and angular velocity disturbances and the aileron, elevator, and rudder control inputs. In order to generate analytical solutions, some sections of this work use a phugoid approximation to these linearized

equations where the state variables are the airspeed and flight path angle and the input is the longitudinal wind velocity disturbance.

For the wind disturbances, this work incorporates stochastic gusts generated using the Dryden model. A coloring filter is appended to the linearized airplane dynamics. It takes white noise as an input and outputs the wind linear and angular velocity disturbance. The analysis does not use the airplane control inputs unless necessary to stabilize the dynamics of a particular airplane, with the notable exception of a section in Chap. V on gust alleviation using feedback control. When used, feedback control is achieved using state feedback and an observer, with the various gains chosen using a linear-quadratic regulator and a linear-quadratic estimator.

The resulting linear time invariant system incorporates the airplane dynamics, the wind gust dynamics, and, in some cases, state feedback and estimation. The covariance matrix of this system can be obtained using a Lyapunov equation. Through careful choice of the system output, the covariance matrix for the linear velocity components of the airplane and wind is computed and used to estimate the variances of the true airspeed and normal load factor. These variances are then used in scaling and flight envelope applications.

1.3 Original Contributions

Drawing on prior work in flight dynamics, turbulence modeling, and dynamic scaling, this dissertation provides the following original contributions:

- Scaling laws for the airplane phugoid mode natural frequency and damping ratio
- Analytical expressions for the airplane airspeed and flight path angle variances in the phugoid approximation parameterized by a new non-dimensional parameter, the phugoid-to-turbulence relative frequency

- Scaling laws for the airplane airspeed and flight path angle variances in the phugoid approximation
- A scaling law for the airplane airspeed coefficient of variation in the phugoid approximation showing decreasing coefficient of variation with increasing airplane size
- Validation of these scaling laws through numerical examples comparing the performance of eleven aircraft, focusing on the NASA Generic Transport Model (GTM) and its dynamically scaled counterpart, the NASA T2 [13]
- A method to determine the probability that a steady flight maneuver violates a steady flight constraint after taking into account stochastic gusts
- Stationary flight envelopes to visualize the probability that a particular combination of steady flight state and turbulence condition will exceed a steady flight constraint for a given airplane

Among these contributions, several provide innovative solutions to the problems addressed in this dissertation. In particular, use of the phugoid approximation in the dynamic scaling problem allows derivation of analytical solutions to the problem. Additionally, use of stationary flight envelopes allows visualization of the safety margins developed for flight through stochastic gusts.

These contributions provide new insights into airplane dynamic response to turbulence as well as quantitative tools to estimate and predict airplane performance in turbulence. These contributions are especially pertinent for small airplanes, which, according to the scaling laws and envelopes of this work, exhibit the largest changes in performance and which, according to the sources cited earlier, are becoming more prevalent in military applications and potentially in commercial applications as well.

1.4 Organization

The remainder of the dissertation is organized into five chapters. Chapter II gives an overview of the literature related to gust models, airplane dynamics and gust response, and dynamic scaling. Chapter III derives the state space, linearized airplane equations of motion used in the subsequent chapters and shows how to incorporate the Dryden model of turbulence and feedback control into these linearized equations.

Chapter IV introduces a phugoid approximation of the equations in Chap. III and dynamic scaling laws from the literature. Using that approximation, Chap. IV derives scaling laws for the phugoid mode, the airspeed variance, the flight path angle variance, and the airspeed coefficient of variation. In the process, Chap. IV shows that the airspeed and flight path angle variances can be parameterized by the ratio of the phugoid natural frequency to the turbulence corner frequency. Chapter IV ends by comparing the derived scaling laws to numerical solutions computed for a variety of aircraft, notably the NASA GTM [14] and the NASA T2 [13].

Following the discussion of scaling, Chap. V presents a technique to quantify airplane performance in turbulence. Chapter V introduces the notion of stationary flight, where an airplane's linear and angular velocities are stationary random processes. Chapter V also introduces the stationary flight envelope, an analog of the steady flight envelope depicting limitations of airplane performance in turbulence. Following the introduction of the stationary flight envelope, the chapter provides a detailed example of a Navion executing various steady flight maneuvers in turbulence with and without feedback control to alleviate the gusts.

The last chapter, Chap. VI, summarizes the work, highlights key contributions, and proposes directions for future study. Three appendices follow the conclusion to provide details on computing the true airspeed, angle of attack, and normal load factor variances, to derive probabilistic measures of staying in the flight envelope, and to describe the various airplane and turbulence models used in the examples.

CHAPTER II

Literature Review

2.1 Introduction

The contributions of this dissertation fall into a much larger body of science and engineering research. The results of the coming chapters rely heavily on this prior work. This chapter outlines some of the existing work that is most important and relevant to the rest of the dissertation. In particular, this chapter provides background in wind gust modeling, flight dynamics, and dimensional analysis in airplane dynamics. It also discusses several topics related to airplane dynamic response to gusts. Because this chapter summarizes work beyond the scope of the dissertation, notations in this chapter differ somewhat from notations in the rest of the dissertation. An effort is made in this chapter to define variables not used or used differently in the remaining chapters.

2.2 Stochastic Gust Models

Wind gust modeling is one of two fields that are critical to this dissertation. Virtually all of the contributions of this dissertation assume that the wind input to the airplane equations of motion is representative of realistic wind gusts. This section provides an overview of how stochastic wind gusts are modeled. Hoblit's text provides

a thorough description of gusts and gust loads [15], while Houbolt [16] and Etkin [17] provides concise summaries.

The wind can be described, classified, and modeled in a variety of ways. The type of wind relevant to this dissertation is wind gusts, brief changes in the wind velocity from a steady value. Gusts are classified into two types: discrete and continuous. Discrete gusts are isolated changes in wind velocity. They may also be added to continuous gusts to represent rare extremes. They are typically modeled as a pulse. When Hoblit computes gust responses, the response to a square pulse, also called a sharp-edge gust, serves as the baseline to compare other gust responses [15]. The FAA prefers discrete gust models with a "1 minus cosine" shape. For example, if there is a lateral gust of maximum speed $v_{wy_{\max}}$, then the gust builds as

$$\delta v_{wy} = \frac{v_{wy_{\max}}}{2}\left(1 - \cos\frac{\pi x}{x_{\max}}\right) \quad 0 \le x \le 2x_{\max}, \tag{2.1}$$

where x is the distance penetrated into the gust, $x_{\max}$ is the position at which the gust reaches a maximum, and δv_{wy} is the deviation of the lateral wind from its steady value [18]. The FAA regulation specifies values for $v_{wy_{\max}}$ and $x_{\max}$. The military has similar standards [19]. Note that the gust is a function of position but not time. In this model, any temporal variation comes from the motion of the aircraft passing through the gust. This is clearly not realistic; any reader has undoubtedly experienced gusts varying in time while the reader stood in one place. Nevertheless, such an assumption is sufficient to model airplane flight in gusts.

Continuous gusts vary randomly in patches lasting for several minutes of flight. The prevailing models of continuous gusts treat them as random processes and make a number of simplifying assumptions in order to describe them mathematically. Chapter 13 of Etkin's text gives a good description of the key assumptions [20], which include:

- Gaussian: The probability distribution of gust velocities is Gaussian
- Stationary: The statistics do not vary with time
- Homogeneous: The statistics do not depend on the path flown by the vehicle
- Ergodic: Ensemble averages equal single sample time averages
- Frozen: The spatially varying gust velocity field does not vary with time
- Isotropic: For high altitude gusts, the statistics do not depend on the orientation of the coordinate axes

Chapter 12 of Hoblit's text thoroughly assesses these assumptions and concludes that, while suspect, they yield an adequate model [15]. These models have analogs for road roughness [21] and rough seas [22, 23].

The two most widely used models of continuous gusts are the Dryden and von Kármán models. These two models have standardized forms specified by the Federal Aviation Administration and the Department of Defense for design and simulation [18, 19]. According to Hoblit [15], the Dryden model first appeared in a 1952 paper by Liepmann [24]. The von Kármán model dates back to a report by Diedrich and Drischler [25], who drew upon earlier work by von Kármán [26, 27, 28] to develop the model. Both models define gusts using power spectral densities. Clear air turbulence and turbulence in storms adhere well to this type of model.

The Dryden model has a rational power spectral density. For example, MIL-HDBK-1797, the Department of Defense's handbook on flying qualities, specifies the power spectral density of the longitudinal linear velocity component in the Dryden model as

$$\Phi_{\delta v_{wx}}(\Omega) = \frac{2L_u\sigma_u^2}{\pi v_t}\frac{1}{1+\left(\frac{L_u\Omega}{v_t}\right)^2}, \tag{2.2}$$

where $\Phi_{\delta v_{wx}}$ is the power spectral density for the longitudinal linear velocity component of the gust, Ω is a spatial frequency, L_u is the longitudinal gust scale length, σ_u is

the root mean square gust velocity or "gust intensity", and v_t is the true airspeed [19]. The power spectral density can be spectrally factorized, meaning a stable, minimum phase transfer function $G_{\delta v_{wx}}(s)$ can be found such that

$$\Phi_{\delta v_{wx}}(\omega) = |G_{\delta v_{wx}}(i\omega)|^2, \tag{2.3}$$

where $i = \sqrt{-1}$. When this transfer function is driven by a white noise input, its output has the power spectral density $\Phi_{\delta v_{wx}}$. Such a filter transforms the white noise process into a colored random process and is sometimes referred to as a "coloring filter". Because the Dryden power spectral density is rational, its spectral factorization is exact.

The von Kármán model has an irrational power spectral density, so its spectral factorization can only be approximated, with an exact factorization requiring a filter of infinite order. However, the von Kármán power spectral density matches experimental observations of gusts more closely than the Dryden model. MIL-HDBK-1797 specifies the power spectral density of the longitudinal linear velocity component in the von Kármán model as [19]

$$\Phi_{\delta v_{wx}}(\Omega) = \frac{2L_u\sigma_u^2}{\pi v_t} \frac{1}{\left(1 + \left(\frac{1.339 L_u \Omega}{v_t}\right)^2\right)^{5/6}}. \tag{2.4}$$

For both models, the choice of turbulence scale length and intensity depend on altitude according specifications given with the spectra. They have three different regimes representing low (below 1000 ft AGL), medium (1000–2000 ft AGL), and high (above 2000 ft AGL) altitude turbulence, where AGL stands for altitude "above ground level". The turbulence intensity varies with turbulence severity.

This dissertation almost exclusively uses the Dryden model to generate the wind gust inputs. This choice is primarily for convenience. The Dryden model yields filters

of lower dynamic order that are more tractable for analytical and numerical computations without sacrificing any illustrative value for the dissertation's contributions. The military specifications indicate that the von Kármán model is preferable in all cases, but that the Dryden model is acceptable for modeling and simulation that do not include structural loading [19].

2.3 Flight Dynamics

This dissertation uses the wind gusts described in the previous section as inputs to airplane dynamic equations. The dynamics of airplane flight are well-known; a number of standard textbooks provide excellent presentations [20, 29, 30, 31, 32]. Flight dynamics are founded on Newton's second law expressed in the body or wind frame, neither of which is inertial. In the body frame, we can say that

$$m(\dot{v}_c + \Omega_\times v_c) = F_a(v_c - v_w, \omega - \omega_w, c) + F_g + F_0, \tag{2.5}$$

$$\dot{h} + \Omega_\times h = M_a(v_c - v_w, \omega - \omega_w, c) + M_0. \tag{2.6}$$

On the left hand side, m is the mass, v_c is the center of mass velocity expressed in the body frame, h is the angular momentum, and $\Omega_\times$ is a skew symmetric matrix formed from the angular velocity ω such that $\Omega_\times v_c$ is the same as the cross product of ω and the center of mass velocity v_c. Therefore, the left hand sides of Eqs. (2.5) and (2.6) represent the time derivatives of the linear and angular momenta, respectively, assuming constant mass and moment of inertia. The terms with $\Omega_\times$ are entrainment terms due to frame rotation. On the right hand side, the net force is split into aerodynamic, gravitational, and other components, and the net torque, or moment, is split into aerodynamic and other components. The aerodynamic force and moment include dependence on the wind linear and angular velocities v_w and ω_w as well as the control input vector c. When combined with kinematic equations for the airplane's

position and attitude, these equations provide a complete nonlinear description of the airplane's six-degree-of-freedom motion.

In most applications, these nonlinear equations are linearized for small perturbations around an equilibrium condition. Chapter III of this dissertation shows how to linearize these equations in the notation used by the later chapters. The chapter also summarizes some of the key assumptions needed to model airplane flight with these equations.

2.4 Steady Flight

The equilibrium conditions of the airplane equations of motion occur when the airplane's linear and angular velocity are constant in the body frame and are called steady flight states. In the Earth frame, the only acceleration possible in a steady flight maneuver is a centripetal acceleration during a steady banked turn, unless we consider instantaneously steady maneuvers such as a steady roll or a steady pull-up. Therefore, after substituting aerodynamic models for the lift and drag and substituting propulsion models for the thrust, we can derive a set of algebraic relationships too numerous to list between the airplane parameters, the atmospheric parameters, the control inputs, and the variables determining the flight state. Steady flight is described in detail in several textbooks [32, 33].

A steady flight state can be parameterized by four variables:

- Altitude above mean sea level, which determines air density [34]
- True airspeed: the magnitude of the velocity of the airplane relative to the wind
- Bank angle: the angle between the vertical in the Earth frame and the z-axis in the wind frame
- Flight path angle: the angle between the velocity vector and horizontal in the

Earth frame

Note that the bank angle and flight path angle, along with the heading angle, are the three Euler angles describing the orientation of the wind frame with respect to the Earth frame. Also note that airplanes cannot achieve all combinations of the four variables. Steady flight is characterized by three constraints:

- Stall constraint: maximum and minimum values for the angle of attack, the angle between the velocity vector and the aircraft longitudinal axis
- Propulsion constraint: a maximum value for the engine thrust or engine power, depending on the type of engine
- Load constraint: maximum and minimum forces of lift, measured relative to weight, that can be withstood by the airframe

The angle of attack, along with the sideslip angle, is an Euler angle describing the orientation of the aircraft body frame with respect to the wind frame. In general, the the minimum angle of attack and normal load factor are negative and not relevant to the analysis in this dissertation.

In steady flight, the stall and propulsion constraints directly limit the range of airspeeds achievable by an airplane at a given altitude. Additionally, for most airplanes, these first two constraints indirectly limit the maximum altitude and most positive flight path angle. The range of achievable flight path angles is also limited by the fact that the steady flight equations assume it is small. For many airplanes, the load constraint can limit the maximum achievable airspeed as well, since the normal load factor might exceed its maximum acceptable value at high speeds. Additionally, a larger lift force is needed to maintain steady turns, so the load constraint limits the maximum bank angle of many aircraft.

The combinations of altitudes, airspeeds, bank angles, and flight path angles that satisfy the steady flight constraints comprise the steady flight envelope. In its full

form, the steady flight envelope is a four-dimensional surface. Points inside the surface are combinations of altitudes, airspeeds, bank angles, and flight path angles that can be achieved as steady flight states and points outside are not. The steady flight envelope is typically depicted in two-dimensional cross-sections. Two particular cross-sections are more popular than the others: altitude versus airspeed, and normal load factor versus airspeed. An example of the former was already shown in Fig. 1.2. The latter is often referred to as a v-n diagram, and an example for a Navion is given in Fig. 2.1. Variants of the v-n diagram also include limits for negative loads.

2.5 Scaling in Flight Dynamics

The airplane dynamic equations described earlier apply very widely to airplane flight. However, the key variables in these equations carry dimensions. This means that the equations do not readily provide a systematic comparison of airplane response and performance between airplanes with different geometries, mass characteristics, engine characteristics, or flying in different atmospheric conditions. Instead, response and performance must be determined separately for each case in absolute terms and then compared.

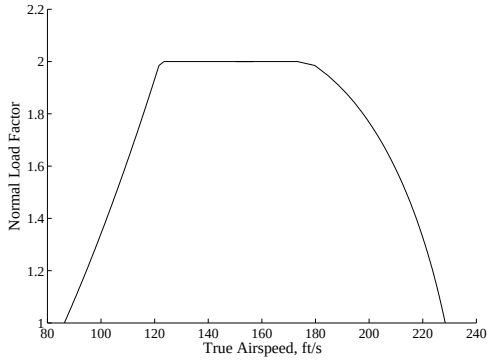

Figure 2.1: v-n diagram for a Navion.

In many applications, comparison of one airplane relative to another is desirable. For example, one might want to understand the performance of a large airplane that is costly, difficult, or dangerous to test by studying a small-scale analog that can be tested readily. If a relationship between the performance of the large airplane relative to the small one exists, then the tests on the small airplane can be used to predict the performance of the large airplane without testing it at all. A variety of scaling

laws exist for airplanes, including several new ones presented in this dissertation.

Scaling of airplane response and performance derives from the general field of dimensional analysis. Dimensional analysis is described well in several textbooks [35, 36]. A key objective in dimensional analysis is to re-express the variables in a model of some system that has dimensions in terms of non-dimensional variables. A key result of dimensional analysis is that the number of independent variables needed to describe the system is often reduced in the transition to dimensionless variables. For most systems,

$$N_p = N_v - N_d, \tag{2.7}$$

where N_v is the number of dimensional variables needed to describe the system, N_d is the number of dimensions needed for those variables, and N_p is the number of dimensionless variables needed to describe the system. Once the dimensionless variables have been defined, systems that may be very different in scale but have the same values for the dimensionless variables have equivalent models and are described as "similar". The most convenient system can be studied, and the conclusions applied to any similar system, as in the airplane flight test example just described. Equation (2.7) represents a special case of the more general Buckingham-π theorem [37].

In flight dynamics, Wolowicz et al. give a thorough overview of similarity requirements and scaling laws [38]. As a simplified example, suppose the lift force acting on an airplane is a function of the following quantities:

- ρ Air density
- μ_a Dynamic viscosity of air
- a Speed of sound in air
- l Airplane characteristic length
- m Airplane mass
- v_t True airspeed
- α Angle of attack
- c Control surface deflections
- g Standard acceleration of free fall

$$F_L = F_L(\rho, \mu_a, a, l, m, v_t, \alpha, c, g). \tag{2.8}$$

The dimensions of these variables can all be expressed in terms of three fundamental dimensions: length, time, and mass. Thus, by Eq. (2.7), our one dependent and nine independent dimensional variables can be reduced to one dependent and six independent dimensionless variables. The choice of dimensionless variables is not unique, but the following choice includes some familiar quantities:

$$C_L \triangleq \frac{2F_L}{\rho v_t^2 l^2} = C_L(\alpha, c, \frac{v_t}{a}, \frac{\rho v_t l}{\mu_a}, \frac{v_t}{\sqrt{gl}}, \frac{m}{\rho l^3}). \tag{2.9}$$

- $\frac{2F_a}{\rho v_t^2 l^2}$ Coefficient of lift (if $l^2 \leftarrow S$)
- $\frac{v_t}{\sqrt{gl}}$ Froude number
- $\frac{v_t}{a}$ Mach number
- $\frac{m}{\rho l^3}$ Relative density
- $\frac{\rho v_t l}{\mu_a}$ Reynolds number

These quantities are not unique to flight dynamics. In fact, these types of similarity and dimensional analysis arguments are very common in fluid mechanics [39] more generally, with analogous applications for ships [40] and supernovae [41].

The dimensionless variables in the example lead to a variety of potential similarities between ostensibly dissimilar aircraft. Related to this notion of similarity is the practice of producing geometrically similar models, where the length and mass characteristics of one aircraft are determined by applying to another aircraft a set of scaling laws described in detail later in Section 4.2. These scaling laws have been used in applications such as system identification of small scale helicopters [42] and development of dynamically scaled aircraft for flight testing [43, 44].

In addition to using scaling laws for model testing, scaling laws can be used to understand the science of flight and predict performance of flyers of different sizes.

One such study by Tennekes produced what he calls the Great Flight Diagram, reproduced in Fig. 2.2. The points in the diagram show the relationship between weight and cruise speed for flyers ranging from a fruit fly to an Airbus A380. The diagonal line represents the scaling law

$$\frac{mg}{S} \propto (mg)^{1/3}, \tag{2.10}$$

that wing loading is proportional to the cube root of the weight. The proportionality constant chosen is 47. The vertical line represents a cruise speed of 10 m/s.

Scaling laws such as that in the Great Flight Diagram are at the intersection of scaling laws for aircraft described above, and a rich literature of scaling laws for animals [46, 47, 48, 49]. In the same vein as Tennekes' work, Shyy et al. provide a review of scaling laws for fixed and flapping wing flight in their text on low Reynolds number flyers [50]. Liu provides a variety of geometric, power, and velocity scaling laws with comparative examples for fixed and flapping wing flight [51].

2.6 Turbulence in Flight Dynamics

Many authors have studied the loads and dynamic response that gusts cause in airplanes, in no small part because of the safety hazard gusts represent, as described in Chap. I. Houbolt [16] and Etkin [17] provide detailed reviews of the literature on gust modeling and applications up to the early 1980s. Hoblit's text provides the most thorough discussion on gust load concepts and applications [15]. Etkin also describes how to incorporate wind disturbances into flight dynamics in the last chapter of his textbook [20].

Chapter 7 of Hoblit's text outlines how to formulate dynamic equations to determine gust loads on aircraft. Chapter 8 of the same text describes loads computed using a short period approximation of the rigid body airplane equations of motion.

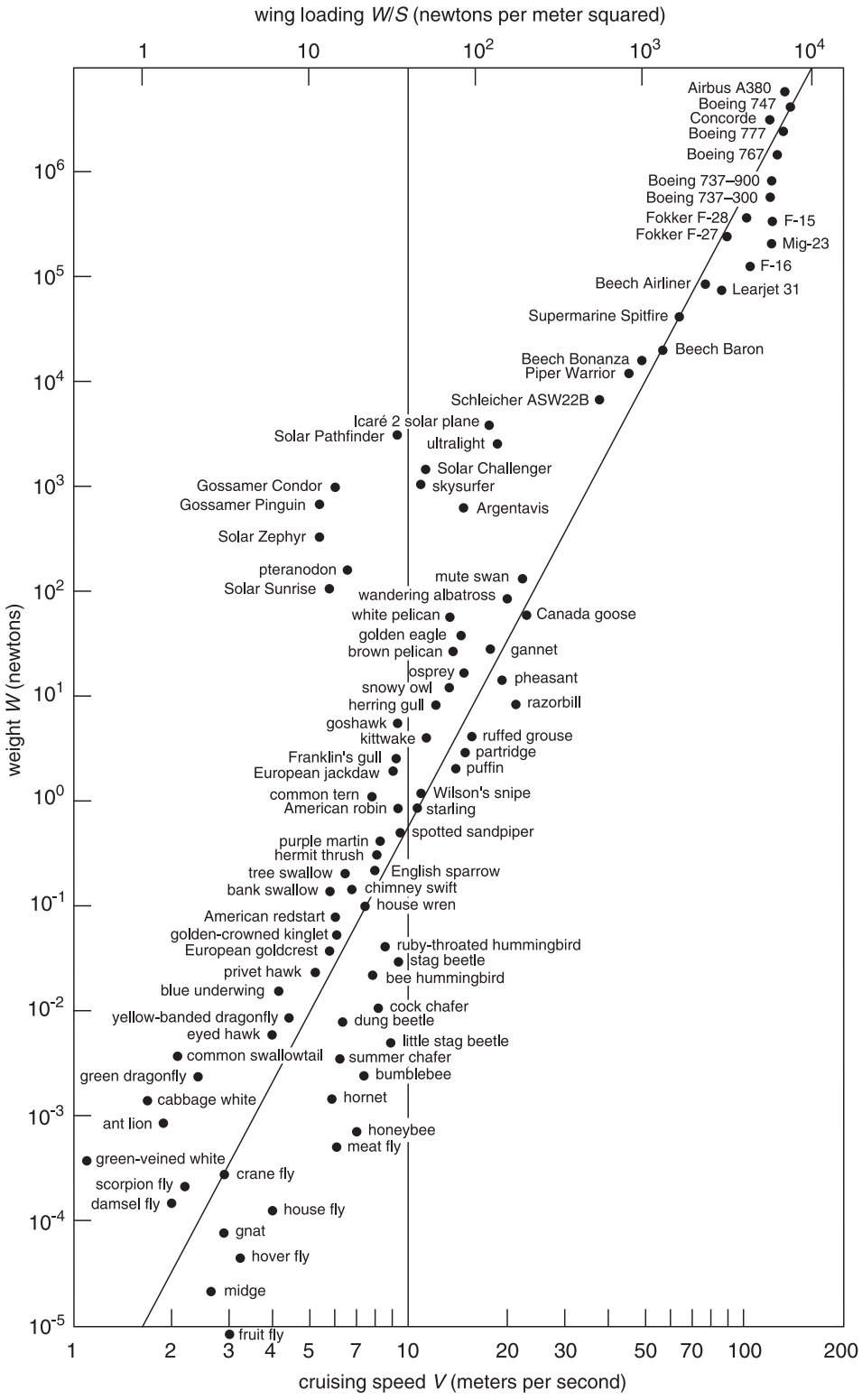

Figure 2.2: The Great Flight Diagram, adopted from [45].

Hoblit's work focuses on calculation of K_σ, where

$$K_\sigma = \frac{\Delta n}{\text{sharp-edge gust } \Delta n}. \tag{2.11}$$

The numerator is the root-mean square normal load factor when the airplane is subject to continuous gusts. The denominator is the root mean square normal load factor when the airplane is subject to gusts modeled with a particular rectangular pulse described in Hoblit's text. Thus, K_σ is a dimensionless coefficient that relates the root mean square normal load factor to a reference normal load factor for a different type of gust.

Hoblit shows that in the short period approximation of the airplane dynamic equations, K_σ can be parameterized by four dimensionless variables:

$$\frac{\delta_{sp}}{L_w}, \quad \frac{\bar{c}}{\delta_{sp}}, \quad \frac{f_{sp}\delta_{sp}}{v_t}, \quad \zeta_{sp},$$

where δ_{sp} is a characteristic airplane length, L_w is the characteristic length of vertical gusts, $\bar{c}$ is the airplane chord length, f_{sp} is the short period natural frequency, and ζ_{sp} is the short period damping ratio. The second dimensionless variable, $\bar{c}/\delta_{sp}$, is a measure of unsteady effects on the response, while the other three characterize the steady short period effects. Hoblit gives examples from a family of charts to look up K_σ for different combinations of the dimensionless variables above. He cites LR 18382, an internal Lockheed Report I could not obtain, that gives the comprehensive set of charts showing how loads depend on the four dimensionless variables.

Chapter IV of this dissertation presents analytical solutions to the gust response in the phugoid approximation. In the process, we show that the steady gust effects are characterized by two dimensionless variables: the phugoid damping ratio and the ratio of the phugoid natural frequency to the turbulence power spectral density's corner frequency. The latter is the phugoid approximation analog of dividing Hoblit's

$f_{sp}\delta_{sp}/v_t$ by δ_{sp}/L_w. This means that these two dimensionless parameters of Hoblit only appear as a ratio in the solution presented in Chap. IV.

Extending the studies of gust loads and airplane response to turbulence, a number of researchers have studied gust alleviation. Phillips [52] provides an early theoretical study of methods to improve smoothness of flight in gusts. McClean [53] shows an automatic elevator controller that alleviates gusts using the load factor, pitch rate, and elevator angle to determine elevator deflections. The study yielded modest alleviation and, according to its conclusions and to Etkin [17], is only effective at low frequencies. Burris [54] gives results from flight tests flown on modified B-52 aircraft where a flight control system was designed to use traditional control surfaces for gust alleviation. These flight tests mainly focused on aeroelastic effects and flutter modes and showed potential to reduce fatigue damage rates. Rynaski [55] gives theoretical but impractical criteria for total gust rejection using direct turbulence measurements, complemented by another work [56] that describes a linear optimal control law for alleviating gusts. More recently, Sato [57] shows an application of Model Predictive Control to the problem of gust alleviation. While recognizing that there is a substantial body of literature on gust alleviation, Chap. V of this dissertation uses simple state feedback with a Kalman filter and the standard control surfaces on a general aviation aircraft to illustrate the potential gains of feedback control in reducing the uncertainty caused by gusts.

In addition to gust alleviation, researchers have studied robustness of controllers with respect to various types of uncertainty. For example, some work has considered robustness with respect to uncertainty in the statistics of disturbances [58, 59]. Additional work studies robustness of systems with respect to model uncertainty and disturbances [60]. Researchers have applied these results to airplane design and control. Some examples include the use of quantitative feedback theory to design controllers robust with respect to variation of an airplane's design parameters through its flight

envelope [61, 62]. Similarly, the FAA and military specifications described earlier in the chapter [18, 19] are meant to standardize the gust models that researchers and manufacturers of airplanes use to test the robustness of their designs and controllers. Nevertheless, little theoretical work is available on the effects of gusts on control of aircraft. Chapter V adds to this field by providing safety margins for flight through turbulence based not only on gust loads but also on the probability of leaving the flight envelope.

2.7 Author's Publications

This dissertation is the culmination of several years of research I published elsewhere. The collective contributions of my work are summarized in Chap. I. Here I cite the relevant publications.

The original paper related to this work [63], presented at the American Institute for Aeronautics and Astronautics (AIAA) Atmospheric Flight Mechanics Conference in 2011, presents an early sketch of the stationary flight envelope concepts found here in Chap. V. A subsequent article accepted in 2012 for publication in the AIAA *Journal of Guidance, Control, and Dynamics* [64] presents the fully developed stationary flight envelope concepts found here in Chap. V, albeit with a different representation of the airplane rotational kinematics. The other article [65], submitted to the AIAA *Journal of Aircraft* shortly before publication of this dissertation, presents the scaled airplane response to turbulence found here in Chap. IV.

CHAPTER III

Developing the Airplane Equations of Motion

3.1 Introduction

Airplane equations of motion can be linearized and expressed in state space form. Such linearized equations are common, and variations can be found in several textbooks [29, 30, 31, 32]. This chapter derives the linearized equations, driven by stochastic gusts formed using the Dryden model, in the notation that is utilized throughout this dissertation. This chapter also incorporates a state feedback controller using the linear-quadratic regular and an observer to stabilize the linearized equations and alleviate gusts. Along the way, the chapter shows how to compute the covariance of the true airspeed, angle of attack, and normal load factor in both the open- and closed-loop cases for use in later applications.

3.2 Linearizing the Airplane Equations of Motion

The linearization starts with the nonlinear airplane dynamic equations from [30],

$$m(\dot{v}_c + \Omega_\times v_c) = F_a(v_c - v_w, \omega - \omega_w, c) + F_g(\epsilon) + F_0, \tag{3.1}$$

$$\dot{h} + \Omega_\times h = M_a(v_c - v_w, \omega - \omega_w, c) + M_0, \tag{3.2}$$

$$\dot{\epsilon} = \mathcal{E}(\omega, \epsilon), \tag{3.3}$$

where definitions for symbols can be found in the List of Symbols at the beginning of the dissertation. All the vectors are expressed in the body frame,

$$h = I\omega, \tag{3.4}$$

$$\mathcal{E}(\omega, \epsilon) = \Phi(\epsilon)\omega, \tag{3.5}$$

$$\Phi(\epsilon) = \begin{pmatrix} 1 & \sin\phi\tan\theta & \cos\phi\tan\theta \\ 0 & \cos\phi & -\sin\phi \end{pmatrix}, \tag{3.6}$$

and

$$I = \int\limits_{\text{Volume}} \rho_{\text{A/C}}(r)\left(||r||^2 \mathbb{1}_3 - rr^{\text{T}}\right) dV = \begin{pmatrix} I_{xx} & -I_{xy} & -I_{xz} \\ -I_{xy} & I_{yy} & -I_{yz} \\ -I_{xz} & -I_{yz} & I_{zz} \end{pmatrix}, \tag{3.7}$$

where r is a position vector with origin at the aircraft center of mass for the integral over the airplane's volume. The yaw Euler angle does not affect any of the other variables, so its dynamics are omitted. $\Omega_\times$ is a skew-symmetric matrix replacing the cross product of a pair of vectors expressed in an orthonormal coordinate system with the inner product of a matrix and a vector, as in the identity

$$\mathbf{a} \times \mathbf{b} = A_\times b = B_\times^{\text{T}} a, \tag{3.8}$$

$$A_\times(a) = \begin{pmatrix} 0 & -a_3 & a_2 \\ a_3 & 0 & -a_1 \\ -a_2 & a_1 & 0 \end{pmatrix}. \tag{3.9}$$

The subscript $\times$ indicates that these matrices replaced cross products.

Figure 3.1 depicts the orientation of the body frame with respect to the Earth frame. The Earth frame axes have subscript E and the body frame axes have subscript b. The x_b axis is the aircraft longitudinal axis and is positive in front of the aircraft. The z_b axis is perpendicular to the x_b axis, is in the plane of symmetry for all aircraft

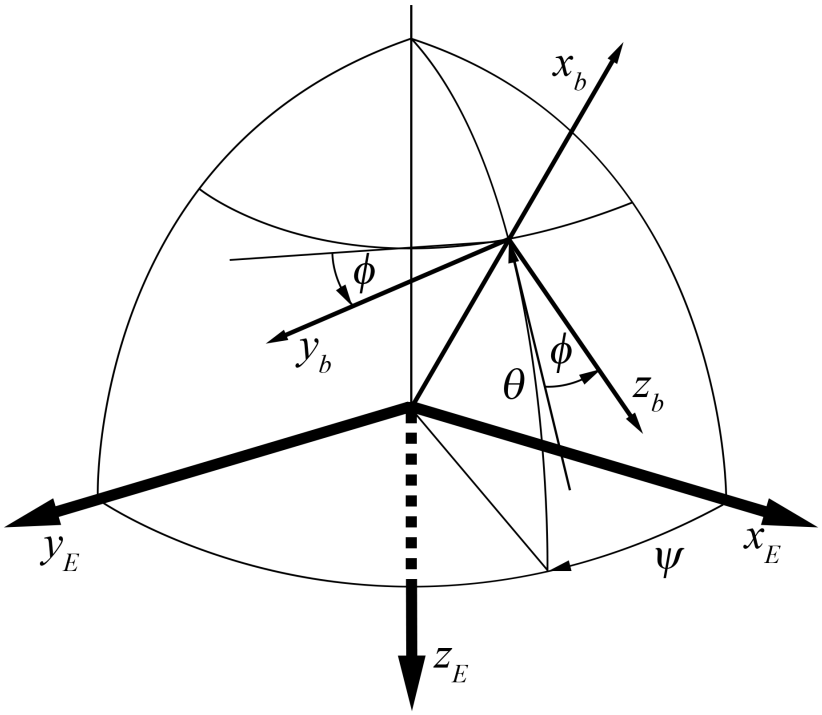

Figure 3.1: Orientation of the body frame with respect to the Earth frame, including the Euler angles. Adapted from Kuipers [66].

studied in this dissertation, and is positive below the aircraft.

Figure 3.1 also depicts the yaw, pitch, and roll Euler angles (ψ, θ, ϕ) and the sequence of rotations to transform between frames. An analogous illustration can be drawn using the heading, flight path, and bank Euler angles (σ, γ, μ) to depict the orientation of the wind frame with respect to the Earth frame. In the wind frame, the positive x_w axis is aligned with the aircraft velocity vector. Another analogous illustration can be drawn using the angles of sideslip, attack, and zero $(\beta, \alpha, 0)$ as Euler angles to depict the orientation of the body frame with respect to the wind frame.

The airplane dynamic equations require a number of assumptions. They assume that the Earth is flat and that a point on the Earth's surface can be the origin of an inertial reference frame. They assume that the airplane's weight and moment of

inertia do not change over time or with altitude. These are standard assumptions justifiable for airplane flight over tens of minutes. They also assume that the airplane is a rigid body, ignoring structural dynamics, also a standard assumption in many applications.

This dissertation focuses on the dynamic response of the airplane to wind velocity perturbations. To represent these perturbations, the following substitutions are made in Eqs. (3.1) and (3.2):

$$v_w \leftarrow v_w + \delta v_w, \qquad \omega_w \leftarrow \omega_w + \delta\omega_w. \tag{3.10}$$

As a consequence of Eqs. (3.1), (3.2), and (3.3), the perturbation of the wind velocity perturbs the airplane's linear and angular velocity and the Euler angles. The control input vector c can be perturbed by the pilot. These perturbations are denoted by the following substitutions:

$$v_c \leftarrow v_c + \delta v_c, \qquad \omega \leftarrow \omega + \delta\omega, \qquad \epsilon \leftarrow \epsilon + \delta\epsilon, \qquad c \leftarrow c + \delta c. \tag{3.11}$$

Henceforth, v_c, v_w, ω, ω_w, ϵ, and c are treated as constant reference values, with δv_c, δv_w, $\delta\omega$, $\delta\omega_w$, $\delta\epsilon$, and δc representing variations. Because of the substitutions,

$$\begin{aligned} m\left(\dot{v}_c + \delta\dot{v}_c + \tilde{\Omega}_\times(v_c + \delta v_c)\right) &= F_a(v_c + \delta v_c - v_w - \delta v_w, \omega + \delta\omega - \omega_w - \delta\omega_w, c + \delta c) \\ &\quad + F_g(\epsilon + \delta\epsilon) + F_0, \end{aligned} \tag{3.12}$$

$$\begin{aligned} \dot{h} + I\delta\dot{\omega} + \tilde{\Omega}_\times(h + I\delta\omega) &= M_a(v_c + \delta v_c - v_w - \delta v_w, \omega + \delta\omega - \omega_w - \delta\omega_w, c + \delta c) \\ &\quad + M_0, \end{aligned} \tag{3.13}$$

$$\dot{\epsilon} + \delta\dot{\epsilon} = \mathcal{E}(\omega, \epsilon) + \delta\mathcal{E}(\omega, \epsilon, \delta\omega, \delta\epsilon). \tag{3.14}$$

By linearity of the cross product,

$$\tilde{\Omega}_\times = \Omega_\times + \delta\Omega_\times, \tag{3.15}$$

where $\tilde{\Omega}_\times$ is formed from the vector $(\omega + \delta\omega)$ and $\delta\Omega_\times$ is formed from $\delta\omega$.

In Eqs. (3.1) and (3.2), the forces and moments have been split into components that depend on the relative wind velocity $v_c - v_w$ and the relative wind angular velocity $\omega - \omega_w$, and components that do not. The components that depend on the relative wind are typically the aerodynamic forces and moments. Both of these relative wind velocities have been perturbed by Eqs. (3.10) and (3.11). Additionally, the gravitational force in Eq. (3.12) depends on the perturbed Euler angles. Therefore,

$$\begin{aligned} &F_a(v_c + \delta v_c - v_w - \delta v_w, \omega + \delta\omega - \omega_w - \delta\omega_w, c + \delta c) = \\ &\qquad F_a(v_c - v_w, \omega - \omega_w, c) + \delta F_a(\delta v_c, \delta\omega, \delta v_w, \delta\omega_w, \delta c), \end{aligned} \tag{3.16}$$

$$\begin{aligned} &M_a(v_c + \delta v_c - v_w - \delta v_w, \omega + \delta\omega - \omega_w - \delta\omega_w, c + \delta c) = \\ &\qquad M_a(v_c - v_w, \omega - \omega_w, c) + \delta M_a(\delta v_c, \delta\omega, \delta v_w, \delta\omega_w, \delta c), \end{aligned} \tag{3.17}$$

$$F_g(\epsilon + \delta\epsilon) = F_g(\epsilon) + \delta F_g(\delta\epsilon). \tag{3.18}$$

Expressions for δF_a, δM_a, and δF_g are derived in the next section.

Replacing the forces, the moments, and $\tilde{\Omega}_\times$ in Eqs. (3.12)–(3.13) with the expressions in Eqs. (3.15)–(3.18), canceling the steady state terms, and ignoring second order terms,

$$m(\delta\dot{v}_c + \delta\Omega_\times v_c + \Omega_\times \delta v_c) = \delta F_a(\delta v_c, \delta\omega, \delta v_w, \delta\omega_w, \delta c) + \delta F_g(\delta\epsilon), \tag{3.19}$$

$$I\delta\dot{\omega} + \delta\Omega_\times h + \Omega_\times I\delta\omega = \delta M_a(\delta v_c, \delta\omega, \delta v_w, \delta\omega_w, \delta c). \tag{3.20}$$

By ignoring second order terms, we have assumed that the center of mass linear and

angular velocity perturbations are small.

Equation (3.14) can be linearized directly by taking partial derivatives of $\mathcal{E}$ with respect to the components of ω and ϵ and evaluating them at the reference condition, resulting in

$$\delta\dot{\epsilon} = \Phi(\epsilon)\delta\omega + \frac{\partial \mathcal{E}}{\partial \epsilon}\delta\epsilon, \tag{3.21}$$

where the partial derivative is shorthand for a Jacobian matrix evaluated at the steady flight reference condition.

In Eq. (3.8), when converting a cross product into an inner product, either vector from the cross product can be converted into a matrix. Therefore, $V_{c\times}$ and $H_\times$ can be defined as prescribed by Eq. (3.8) to express products such as $\delta\Omega_\times v_c$ in terms of $\delta\omega$. Recall that the matrices with subscript $\times$ are each equal to the negative of their transpose. Also, in realistic applications, the airplane's moment of inertia matrix is positive definite and invertible. After making these substitutions,

$$\begin{pmatrix} \delta\dot{v}_c \\ \delta\dot{\omega} \\ \delta\dot{\epsilon} \end{pmatrix} = \begin{pmatrix} -\Omega_\times & V_{c\times} & 0 \\ 0 & I^{-1}(H_\times - \Omega_\times I) & 0 \\ 0 & \Phi & \frac{\partial \mathcal{E}}{\partial \epsilon} \end{pmatrix} \begin{pmatrix} \delta v_c \\ \delta\omega \\ \delta\epsilon \end{pmatrix} + \begin{pmatrix} \frac{1}{m}\mathbb{1}_3 & 0 & \frac{1}{m}\mathbb{1}_3 \\ 0 & I^{-1} & 0 \\ 0 & 0 & 0 \end{pmatrix} \begin{pmatrix} \delta F_a \\ \delta M_a \\ \delta F_g \end{pmatrix}, \tag{3.22}$$

where perturbation of the forces and moment are inputs and perturbations of the airplane's linear velocity, angular velocity, and Euler angles are states.

3.3 Perturbing the Forces & Moments

Next, δF_a and δM_a must be related to the relative wind and δF_g to the Euler angles. Expanding the left hand side of Eqs. (3.16) and (3.17) to first order,

$$\begin{aligned} &F_a(v_c + \delta v_c - v_w - \delta v_w, \omega + \delta\omega - \omega_w - \delta\omega_w, c + \delta c) \approx \\ &\quad F_a(v_c - v_w, \omega - \omega_w, c) + \frac{\partial F_a}{\partial v}\Big(\delta v_c - \delta v_w\Big) + \frac{\partial F_a}{\partial \omega}\Big(\delta\omega - \delta\omega_w\Big) + \frac{\partial F_a}{\partial c}\delta c, \end{aligned} \tag{3.23}$$

$$\begin{aligned} &M_a(v_c + \delta v_c - v_w - \delta v_w, \omega + \delta\omega - \omega_w - \delta\omega_w, c + \delta c) \approx \\ &\quad M_a(v_c - v_w, \omega - \omega_w, c) + \frac{\partial M_a}{\partial v}\Big(\delta v_c - \delta v_w\Big) + \frac{\partial M_a}{\partial \omega}\Big(\delta\omega - \delta\omega_w\Big) + \frac{\partial M_a}{\partial c}\delta c. \end{aligned} \tag{3.24}$$

In the body frame,

$$F_g(\epsilon) = mg\begin{pmatrix} -\sin\theta & \cos\theta\sin\phi & \cos\theta\cos\phi \end{pmatrix}^{\mathrm{T}} \tag{3.25}$$

To first order in perturbation of ϵ,

$$F_g(\epsilon + \delta\epsilon) \approx F_g(\epsilon) + \frac{\partial F_g}{\partial \epsilon}\delta\epsilon. \tag{3.26}$$

The partial derivatives in Eqs. (3.23), (3.24), and (3.26) are shorthand for Jacobian matrices evaluated at the steady flight reference condition. For the derivatives of aerodynamic forces and moments, the matrices consist of airplane stability and control derivatives.

Comparing Eqs. (3.23), (3.24), and (3.26) with Eqs. (3.16)–(3.18) reveals that, to

first order,

$$\delta F_a(\delta v_c, \delta\omega, \delta v_w, \delta\omega_w, \delta c) \approx \frac{\partial F_a}{\partial v}\Big(\delta v_c - \delta v_w\Big) + \frac{\partial F_a}{\partial \omega}\Big(\delta\omega - \delta\omega_w\Big) + \frac{\partial F_a}{\partial c}\delta c, \quad (3.27)$$

$$\delta M_a(\delta v_c, \delta\omega, \delta v_w, \delta\omega_w, \delta c) \approx \frac{\partial M_a}{\partial v}\Big(\delta v_c - \delta v_w\Big) + \frac{\partial M_a}{\partial \omega}\Big(\delta\omega - \delta\omega_w\Big) + \frac{\partial M_a}{\partial c}\delta c, \quad (3.28)$$

$$\delta F_g(\delta\epsilon) \approx \frac{\partial F_g}{\partial \epsilon}\delta\epsilon. \quad (3.29)$$

Making these substitutions, Eq. (3.22) becomes

$$\begin{pmatrix} \delta\dot{v}_c \\ \delta\dot{\omega} \\ \delta\dot{\epsilon} \end{pmatrix} = \begin{pmatrix} -\Omega_\times + \frac{1}{m}\frac{\partial F_a}{\partial v} & V_{c\times} + \frac{1}{m}\frac{\partial F_a}{\partial \omega} & \frac{1}{m}\frac{\partial F_g}{\partial \epsilon} \\ I^{-1}\frac{\partial M_a}{\partial v} & I^{-1}\left(H_\times - \Omega_\times I + \frac{\partial M_a}{\partial \omega}\right) & 0 \\ 0 & \Phi & \frac{\partial \mathcal{E}}{\partial \epsilon} \end{pmatrix} \begin{pmatrix} \delta v_c \\ \delta\omega \\ \delta\epsilon \end{pmatrix} + \begin{pmatrix} \frac{1}{m}\frac{\partial F_a}{\partial c} \\ I^{-1}\frac{\partial M_a}{\partial c} \\ 0 \end{pmatrix} \delta c - \begin{pmatrix} \frac{1}{m}\frac{\partial F_a}{\partial v} & \frac{1}{m}\frac{\partial F_a}{\partial \omega} \\ I^{-1}\frac{\partial M_a}{\partial v} & I^{-1}\frac{\partial M_a}{\partial \omega} \\ 0 & 0 \end{pmatrix} \begin{pmatrix} \delta v_w \\ \delta\omega_w \end{pmatrix}, \quad (3.30)$$

a linear time invariant (LTI) system with wind velocity perturbations as the input.

Note the following about Eq. (3.30):

- The wind perturbations are not assumed to be random processes. These equations could also be used to study an airplane's impulse response, the response to pulses approximating discrete gusts, or the step response to wind shear.
- The forces and moments have not been perturbed with respect to linear or angular acceleration, hence we assume that those effects are negligible.
- To linearize the forces, we assume a small angle of attack and define the maximum angle of attack as the angle above which the lift coefficient cannot be modeled as proportional to angle of attack, illustrated in Fig. 3.2. These assumptions are consistent with those used in McClamroch's steady flight analysis [33]. This definition for the maximum angle of attack should not be confused

with the angle corresponding to the largest possible lift coefficient $C_{L_{\max}}$.

- Stability derivative values typically come from wind tunnel testing and may change with flight state. They are not readily available for many aircraft. Nelson [30] explains how to compute these stability derivatives and tabulates their values for several aircraft.

3.4 Modeling the Gusts

Until this point, the only assumption made about the wind velocity perturbations has been that they result in small perturbations of the forces, moments, and state variables. This is necessary to discard higher order terms in the linearization. Applying this model to flight through turbulence requires substitution of stationary random processes for δv_w and $\delta \omega_w$. Such a definition of gusts is consistent with turbulence found in clear air or storms but not with wind shear or discrete gusts. Engineers typically use the Dryden and von Kármán models of stochastic gusts [15, 19]. Both models define gusts in terms of their power spectral densities, and in both cases the random processes are colored.

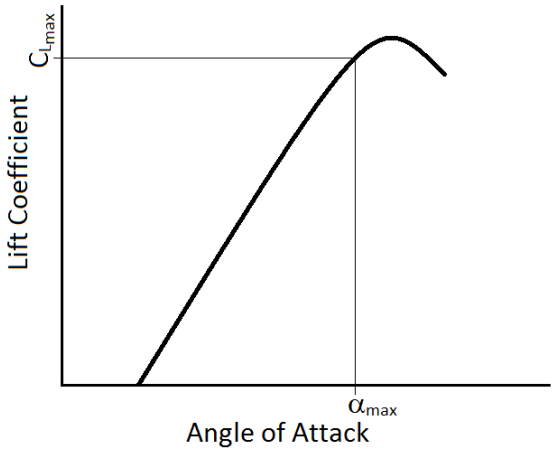

Figure 3.2: Illustration of the lift coefficient as a function of the angle of attack highlighting $C_{L_{\max}}$.

We define the spectral density of $(\delta v_w \quad \delta \omega_w)^{\mathrm{T}}$ and assume that it has a rational spectral factorization. This factorization exists for the Dryden model but can only be approximated for the von Kármán model [15]. Once the spectral density has been factorized, the wind velocity perturbations are modeled as the output of a coloring filter driven by Gaussian white noise $d(t)$ with zero mean and covariance matrix D.

Denote a realization of the filter in state space form as

$$\dot{\xi}_w = A_w \xi_w + E_w d(t), \tag{3.31a}$$

$$\begin{pmatrix} \delta v_w \\ \delta \omega_w \end{pmatrix} = C_w \xi_w = \begin{pmatrix} C_{wv} \\ C_{w\omega} \end{pmatrix} \xi_w, \tag{3.31b}$$

$$d(t) \sim \mathcal{N}(0, D). \tag{3.32}$$

Examples of such filters, such as the one used later from [67], have been derived from the power spectral densities of the Dryden or von Kármán models given in MIL-HDBK-1797 [19]. MIL-HDBK-1797 gives criteria based on airplane stability derivatives to judge when the angular velocity components of the gusts will be non-negligible.

3.5 Combining the Models

Appending the filter from the previous section to Eq. (3.30),

$$\begin{pmatrix} \delta \dot{v}_c \\ \delta \dot{\omega} \\ \delta \dot{\epsilon} \\ \dot{\xi}_w \end{pmatrix} = \begin{pmatrix} -\Omega_\times + \frac{1}{m}\frac{\partial F_a}{\partial v} & V_{c\times} + \frac{1}{m}\frac{\partial F_a}{\partial \omega} & \frac{1}{m}\frac{\partial F_g}{\partial \epsilon} & -\frac{1}{m}\left(\frac{\partial F_a}{\partial v} C_{wv} + \frac{\partial F_a}{\partial \omega} C_{w\omega}\right) \\ I^{-1}\frac{\partial M_a}{\partial v} & I^{-1}\left(H_\times - \Omega_\times I + \frac{\partial M_a}{\partial \omega}\right) & 0 & -I^{-1}\left(\frac{\partial M_a}{\partial v} C_{wv} + \frac{\partial M_a}{\partial \omega} C_{w\omega}\right) \\ 0 & \Phi & \frac{\partial \mathcal{E}}{\partial \epsilon} & 0 \\ 0 & 0 & 0 & A_w \end{pmatrix} \begin{pmatrix} \delta v_c \\ \delta \omega \\ \delta \epsilon \\ \xi_w \end{pmatrix}$$
$$+ \begin{pmatrix} \frac{1}{m}\frac{\partial F_a}{\partial c} \\ I^{-1}\frac{\partial M_a}{\partial c} \\ 0 \\ 0 \end{pmatrix} \delta c + \begin{pmatrix} 0 \\ 0 \\ 0 \\ B_w \end{pmatrix} d(t), \tag{3.33}$$

or more compactly,

$$\dot{x} = Ax + B\delta c + Ed(t). \tag{3.34}$$

The system of Eq. (3.33) is linear and driven by zero-mean, Gaussian white noise. In applications with asymptotically stable dynamics, the perturbations δv_c and $\delta\omega$ are also zero-mean, Gaussian, stationary random processes. For a white noise input to Eq. (3.33), the steady state covariance P_{OL} of this open-loop system's state is the solution of the Lyapunov equation [68]

$$AP_{\mathrm{OL}} + P_{\mathrm{OL}}A^{\mathrm{T}} + EDE^{\mathrm{T}} = 0. \tag{3.35}$$

For P_{OL} to be finite, unique, and positive definite, two conditions must hold. First, A must be asymptotically stable. Second, (A, E_c) must be controllable, where, since EDE^{T} is positive semidefinite, it can be factorized as $E_cE_c^{\mathrm{T}}$.

The applications considered later require the covariance of the true airspeed, the angle of attack, and the normal load factor. So, we choose $(\delta v_t \quad \delta\alpha \quad \delta n)^{\mathrm{T}}$ as the output of the LTI system, with corresponding output matrix C_{POL}. Equation (A.17) in Appendix A defines C_{POL}. The output's covariance matrix is

$$P = C_{\mathrm{POL}}P_{\mathrm{OL}}C_{\mathrm{POL}}^{\mathrm{T}}. \tag{3.36}$$

The diagonal of P contains the variances of the true airspeed, angle of attack, and normal load factor. The applications presented in later chapters use these variances to determine the probability that the airplane strays outside its flight envelope.

3.6 Incorporating Feedback Control

The larger the entries in P, the greater the uncertainty in the state, and the larger the margin of safety required for safe operation. The terms in P can be adjusted in several ways. First, airplanes can be designed to be more or less sensitive to gusts, i.e., by changing the parameters of aircraft performance reflected in state matrix

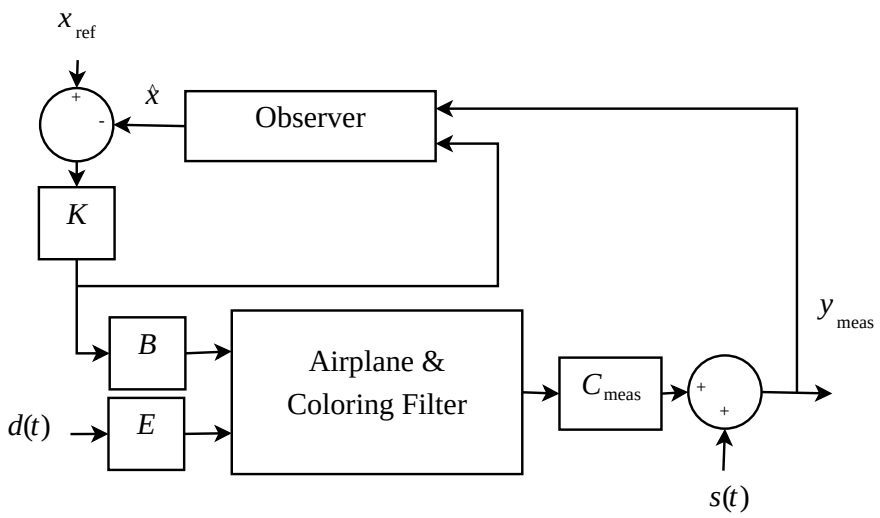

Figure 3.3: Observer-based state feedback control system architecture used for gust rejection.

A. Second, pilots can choose how and under what turbulence conditions to fly the airplane, i.e., the pilot determines the reference steady flight state and which forecast turbulence levels are acceptable. This section shows that control action to alleviate gust loads can also reduce the components of P. In many cases, control action will also be necessary to stabilize the dynamics of Eq. (3.30).

Consider the system in Eq. (3.34) with output

$$y_{\text{meas}} = \begin{pmatrix} \delta v_{\text{meas}} & \delta\omega_{\text{meas}} \end{pmatrix}^{\text{T}} = C_{\text{meas}} x + s(t), \tag{3.37}$$

$$s(t) \sim \mathcal{N}(0, S_{\text{meas}}). \tag{3.38}$$

A controller design must be selected. To illustrate how feedback control affects the covariance of the states, state feedback with a Kalman filter is utilized. The control architecture is illustrated in Fig. 3.3. As described in Chap. II, various feedback control designs exist for gust alleviation, many of which may perform better than this controller. This controller is chosen because its effect on the covariance of the state variables can readily be shown analytically.

Defining the state estimate from the Kalman filter as $\hat{x}$ and the estimate's error as $\Delta x = x - \hat{x}$,

$$\begin{pmatrix} \dot{x} \\ \Delta\dot{x} \end{pmatrix} = \begin{pmatrix} A - BK & BK \\ 0 & A - LC_{\text{meas}} \end{pmatrix} \begin{pmatrix} x \\ \Delta x \end{pmatrix} + \begin{pmatrix} BK \\ 0 \end{pmatrix} x_{\text{des}} + \begin{pmatrix} E & 0 \\ E & -L \end{pmatrix} \begin{pmatrix} d(t) \\ s(t) \end{pmatrix}, \tag{3.39a}$$

$$y_{\text{meas}} = \begin{pmatrix} C_{\text{meas}} & 0 \end{pmatrix} \begin{pmatrix} x \\ \Delta x \end{pmatrix} + s(t), \tag{3.39b}$$

where the state feedback gain K and the observer gain L are

$$K = R^{-1} B^{\mathrm{T}} \bar{P}, \tag{3.40}$$

$$L = \bar{\Sigma} C_{\text{meas}}^{\mathrm{T}} S_{\text{meas}}^{-1}. \tag{3.41}$$

$\bar{P}$ and $\bar{\Sigma}$ are the respective solutions of the algebraic Riccati equations

$$\bar{P}A + A^{\mathrm{T}}\bar{P} + Q - \bar{P}BR^{-1}B^{\mathrm{T}}\bar{P} = 0, \tag{3.42}$$

$$\bar{\Sigma}A^{\mathrm{T}} + A\bar{\Sigma} + D - \bar{\Sigma}C_{\text{meas}}^{\mathrm{T}} S_{\text{meas}}^{-1} C_{\text{meas}} \bar{\Sigma} = 0. \tag{3.43}$$

Q and R are weight matrices for a linear-quadratic regulator (LQR).

Equation (3.39) can be expressed more compactly as

$$\dot{x}_{\text{CL}} = A_{\text{CL}} x_{\text{CL}} + B_{\text{CL}} x_{\text{des}} + E_{\text{CL}} \begin{pmatrix} d(t) \\ s(t) \end{pmatrix}, \tag{3.44a}$$

$$y_{\text{meas}} = C_{\text{CL}} x_{\text{CL}} + s(t). \tag{3.44b}$$

As in Eq. (3.35), the covariance of the closed-loop system's state vector is the solution

of a Lyapunov equation,

$$A_{\mathrm{CL}}P_{\mathrm{CL}} + P_{\mathrm{CL}}A_{\mathrm{CL}}^{\mathrm{T}} + E_{\mathrm{CL}} \begin{pmatrix} D & 0 \\ 0 & S_{\mathrm{meas}} \end{pmatrix} E_{\mathrm{CL}}^{\mathrm{T}} = 0. \tag{3.45}$$

By once again restricting attention to the covariance of $(\delta v_t \quad \delta\alpha \quad \delta n)^{\mathrm{T}}$ using the output matrix $C_{\mathrm{PCL}} = (C_{\mathrm{POL}} \quad 0)$ applied to the closed-loop state variables $(x \quad \Delta x)^{\mathrm{T}}$, the covariance matrix P is

$$P = C_{\mathrm{PCL}}P_{\mathrm{CL}}C_{\mathrm{PCL}}^{\mathrm{T}}. \tag{3.46}$$

The entries of P, whether computed for an open- or closed-loop system, provide the statistics necessary for the applications that follow.

CHAPTER IV

Dynamic Scaling of Airplane Response to Stochastic Gusts

4.1 Introduction

This chapter presents scaling laws for the phugoid mode, the airspeed and flight path angle variances, and the airspeed coefficient of variation. In the process, an analytical solution for the airspeed and flight path angle variances is derived and shown to depend on a new non-dimensional parameter, the airplane-to-turbulence relative frequency. The analytical results are validated using models of a variety of airplanes, particularly stability derivative models of the NASA Generic Transport Model (GTM) and the NASA T2. The numerical examples are primarily given for the phugoid approximation, though some are from the full linearization presented in Chap. III.

Section 4.2 summarizes the scaling laws presented in the literature. Section 4.3 summarizes a phugoid approximation of the model in Chap. III and shows how this phugoid model's natural frequency and damping ratio depend on airplane size. Section 4.3 also derives an analytical solution for the airspeed and flight path angle variances in the phugoid model in terms of a new non-dimensional parameter. Section 4.4 provides numerical examples of the models from Chap. III and 4.3 that dynamically

scale a full-size transport airplane in comparison to a scale model. Section 4.4 also shows how these two transports compare to a variety of other airplanes.

4.2 Dynamic Scaling

To compare aircraft of different sizes, the aircraft should be dynamically scaled according to established similitude requirements and scaling laws. Wolowicz et al. present a comprehensive review of similitude requirements for scale models of aircraft [38]. Their review describes similarity of geometry, angle of attack, Reynolds number, Froude number, and Mach number and lists other similarities that may be important in applications. For geometric similarity, a set of scaling laws are presented in Mettler et al. [42] and Burk and Wilson [43]:

$$\text{Length:} \qquad l_m = N l_f, \tag{4.1a}$$

$$\text{Area:} \qquad S_m = N^2 S_f, \tag{4.1b}$$

$$\text{Mass:} \qquad m_m = N^3 m_f, \tag{4.1c}$$

$$\text{Inertia:} \qquad I_m = N^5 I_f, \tag{4.1d}$$

$$\text{Speed:} \qquad v_m = \sqrt{N} v_f, \tag{4.1e}$$

$$\text{Angular Rate:} \qquad \omega_m = \frac{1}{\sqrt{N}} \omega_f, \tag{4.1f}$$

where the subscripts "m" and "f" stand for "model" and "full-size", and N is the length scale factor, meaning a quantity such as the model aircraft's wingspan will be N times the wingspan of the full-size aircraft. Wolowicz et al. describe some of the assumptions needed to make these geometric similarity arguments, mainly as they relate to similarity in Reynolds and Froude numbers [38].

In the work of Burk and Wilson [43] and Jordan et al. [44, 69], scaling is used to design small-scale model airplanes upon which experiments are conducted that

give insight into the performance of the full-size airplane. In Shyy et al., on the other hand, scaling laws presented at the beginning of the book are meant to explain how parameters and performance variables can be expected to vary over aircraft of different sizes [50]. This chapter of the dissertation uses scaling in a manner similar to Shyy [50]. The contributions of this chapter center on deriving other scaling laws from those above and drawing conclusions about how aircraft performance is a function of aircraft size. As such, the scale factor N is often referred to in this chapter as a measure of aircraft size relative to some arbitrary baseline aircraft.

The scaling relationships above also depend on the relative density of the air, since, in many cases, a model and full-size aircraft do not operate at the same altitude. Rather than include the density explicitly in the scaling laws above, we assume that smaller aircraft operate at lower altitudes than their larger counterparts, or

$$\rho = \rho(a(N)), \qquad \frac{d\rho}{dN} \leq 0, \tag{4.2}$$

where here a is the altitude. Equation (4.2) shows that the air density decreases with increasing N over the range of length scales for fixed wing flight. In the figures in Section 4.4, however, the air density is held constant for the dynamic scaling, i.e., each curve compares scaled aircraft at a particular altitude. On a related note, the turbulence parameters in the Dryden model vary with altitude. For fixed probability of exceedance, the most severe turbulence generally occurs at roughly 5,000 ft above the ground [19].

Note that scaling the airplane equations of motion down to small flyers can be perilous. In his 1934 text on insect flight, Magnan relates:

> "Tout d'abord, poussé par ce qui se fait en aviation, j'ai appliqué aux insectes les lois de la résistance de l'air, et je suis arrivé avec M. Sainte-Laguë à cette conclusion que leur vol est impossible." [70]

To paraphrase, by applying the laws of aerodynamics to insects, Magnan and Sainte-Laguë conclude that insect flight is impossible. Among other subtleties, some of the models of aerodynamic forces and moments in airplane flight assume a large Reynolds number. As the length scale becomes sufficiently small, this assumption ceases to hold. This dissertation only considers length scales relevant for fixed wing flight at high Reynolds number. Detailed analysis of aerodynamics at Reynolds numbers of 10^5 and below is available in Shyy et al. [50].

4.3 Turbulence in the Phugoid Model

4.3.1 Phugoid Model

The phugoid model described in Stengel [32] is a model order reduction that captures the airspeed and flight path angle dynamics of the linearized dynamics presented in Chap. III. As described in detail in Chap. V, the airspeed statistics can be used to compute safety margins and envelopes for steady flight maneuvers performed in turbulence, hence the interest in the phugoid approximation. In particular, the airspeed statistics can be used to identify steady flight states close to the stall and propulsion boundaries of the steady flight envelope, including the flight ceiling, that are unlikely to be maintainable and prone to loss of control in turbulence. The phugoid equations of motion are

$$\begin{pmatrix} \delta\dot{V} \\ \delta\dot{\gamma} \end{pmatrix} = \begin{pmatrix} -\frac{1}{m}\frac{\partial F_D}{\partial V} & -g\cos\gamma \\ \frac{1}{mV}\frac{\partial F_L}{\partial V} & \frac{g\sin\gamma}{V} \end{pmatrix} \begin{pmatrix} \delta V \\ \delta\gamma \end{pmatrix} + \frac{1}{m}\begin{pmatrix} \frac{\partial F_D}{\partial V} \\ -\frac{1}{V}\frac{\partial F_L}{\partial V} \end{pmatrix} \delta v_{wx}, \tag{4.3}$$

or more compactly,

$$\delta\dot{x}_p = A_p\delta x_p + E_p\delta v_{wx}. \tag{4.4}$$

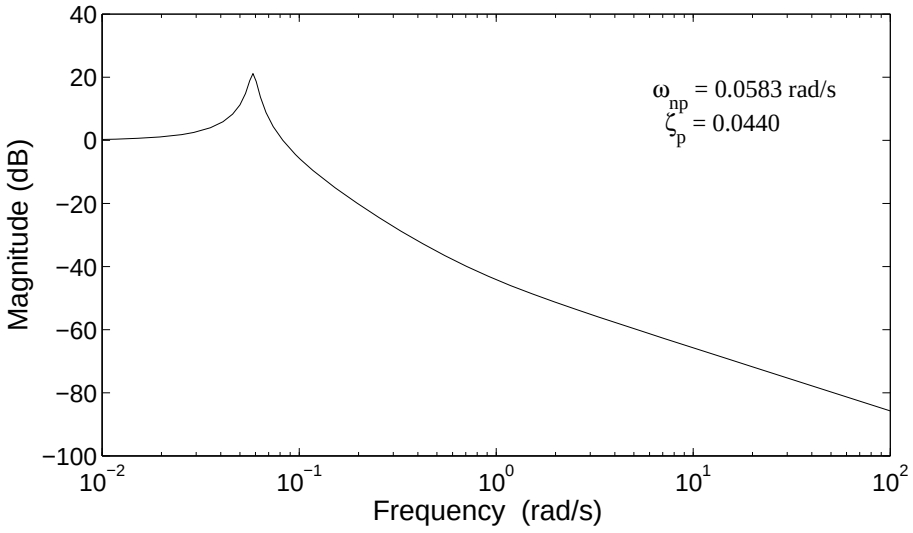

Figure 4.1: Bode magnitude plot for the GTM's phugoid approximation.

From here the discussion is limited to level reference conditions, i.e., $\gamma = 0$. The characteristic equation for this system is

$$s^2 + \frac{1}{m}\frac{\partial F_D}{\partial V}s + \frac{g}{mV}\frac{\partial F_L}{\partial V} = 0. \tag{4.5}$$

From the coefficients of the characteristic equation, the natural frequency and damping ratio are

$$\omega_{np} = \sqrt{\frac{g}{mV}\frac{\partial F_L}{\partial V}}, \tag{4.6}$$

$$\zeta_p = \frac{1}{2m\omega_{np}}\frac{\partial F_D}{\partial V}. \tag{4.7}$$

Qualitatively, the frequency response of both the airspeed and the flight path angle to a wind disturbance has a flat or upward sloping low-frequency response, a resonant peak at ω_{np} if $\zeta_p < 0$, and a high-frequency response that falls off with frequency. Fig. 4.1 shows the Bode magnitude plot for the GTM's phugoid approximation.

For the forces of lift and drag,

$$F_L = \frac{1}{2}\rho S C_L V^2, \tag{4.8}$$

$$F_D = \frac{1}{2}\rho S C_D V^2, \tag{4.9}$$

$$\frac{\partial F_L}{\partial V} = \rho S C_L V + \frac{1}{2}\rho S V^2 \frac{\partial C_L}{\partial V}, \tag{4.10}$$

$$\frac{\partial F_D}{\partial V} = \rho S C_D V + \frac{1}{2}\rho S V^2 \frac{\partial C_D}{\partial V}. \tag{4.11}$$

Set $\frac{\partial C_L}{\partial V} = \frac{\partial C_D}{\partial V} = 0$ for subsonic flight, as it is, for example, in all of the stability derivative models presented in the appendix of Nelson [30]. Substituting these expressions into the natural frequency and damping ratio,

$$\omega_{np} = \sqrt{\frac{g\rho S C_L}{m}}, \tag{4.12}$$

$$\zeta_p = \frac{C_D V}{2}\sqrt{\frac{\rho S}{m g C_L}}. \tag{4.13}$$

Substituting the scaling laws in Eqs. (4.1a)–(4.1f) gives a scaling law for the phugoid mode.

Scaling Law 1: Phugoid Mode

$$\omega_{np} \propto \sqrt{\frac{\rho(N)}{N}}, \tag{4.14}$$

$$\zeta_p \propto \sqrt{\rho(N)}. \tag{4.15}$$

□

The natural frequency decreases with increasing airplane size. Its $N^{-1/2}$ dependence is consistent with the angular rate scaling law of Eq. (4.1f). It has an additional dependence through the air density that also decreases with increasing size. The damping ratio decreases with increasing N, but only due to the higher flight altitude

of larger aircraft. Because of these relationships, small aircraft are more sensitive to high frequency gusts than large aircraft. Similarly, the resonant peak of small aircraft is at a higher frequency than that of large aircraft and is smaller due to increased air density at low altitude.

4.3.2 Covariance of the Phugoid Model

The phugoid model is driven by gusts along the same direction as the velocity vector. At altitudes above 2,000 ft, the Dryden turbulence model provides the power spectral density and coloring filter transfer function for turbulence along the aircraft longitudinal axis [67]. For small angles of attack and sideslip, these gust components along the wind and body frame x-axes are approximately equal. Appending a state variable of the coloring filter to Eq. (4.4),

$$\begin{pmatrix} \delta\dot{x}_p \\ \dot{\xi}_{v_{wx}} \end{pmatrix} = \begin{pmatrix} A_p & E_p C_{v_{wx}} \\ 0 & A_{v_{wx}} \end{pmatrix} \begin{pmatrix} \delta x_p \\ \xi_{v_{wx}} \end{pmatrix} + \begin{pmatrix} 0 \\ B_{xw} \end{pmatrix} n(t). \tag{4.16}$$

As with Eq. (3.35), a Lyapunov equation can provide this LTI system's state variables' covariance. Solving the Lyapunov equation analytically and substituting in Eqs. (4.10) and (4.11) as well as the coloring filter matrices yields analytical expressions for the airspeed and flight path angle variances. Relating them to the scaling laws already presented leads to a scaling law for these variances.

Scaling Law 2: Airspeed & Flight Path Angle Variances

$$\sigma_V^2 = \left(\frac{\sigma_u^2}{\pi}\right) \frac{2\zeta_p\kappa + \frac{\kappa}{2\zeta_p} + \kappa^2}{1 + 2\zeta_p\kappa + \kappa^2}, \tag{4.17}$$

$$\sigma_\gamma^2 = \left(\frac{\sigma_u^2}{V^2\pi}\right) \left(\frac{C_L}{C_D}\right)^2 \frac{2\zeta_p\kappa}{1 + 2\zeta_p\kappa + \kappa^2}, \tag{4.18}$$

$$\kappa \triangleq \frac{\omega_{np}}{\omega_{\text{turb}}}, \tag{4.19}$$

$$\omega_{\text{turb}} \triangleq \frac{V}{L_u}, \tag{4.20}$$

After substituting in the scaling laws for ω_{np} and V,

$$\kappa \propto \frac{1}{N}. \tag{4.21}$$

□

The frequency ω_{turb} is the corner frequency of the longitudinal turbulence power spectral density. So, κ is the relative frequency of the airplane phugoid mode to the turbulence corner frequency. To understand why the turbulence's corner frequency depends on the airplane's airspeed, recall that the Dryden and von Kármán models assume a spatially varying turbulence velocity field frozen in time. The temporal frequency content of the stochastic gusts depends on how fast the airplane travels through the spatially varying field.

Figures 4.2 and 4.3 show how σ_V^2 and σ_γ^2 depend on κ and ζ_p. The other parameters, $\frac{C_L}{C_D}$, σ_u^2, and $\frac{\sigma_u^2}{V^2}$, are kept fixed at the GTM's values for steady level longitudinal flight at Mach 0.8 and 35,000 ft in moderate turbulence. The airplane and turbulence model parameters are described in detail in Section 4.4 and Appendix C. The range of values for κ starts at the GTM's value at the small end and increases until the length scale factor $N = 0.01$ in Eq. (4.21). Both σ_V^2 and σ_γ^2 have peaks near the low end of this range of κ. The range of values for ζ_p starts at the order of magnitude of

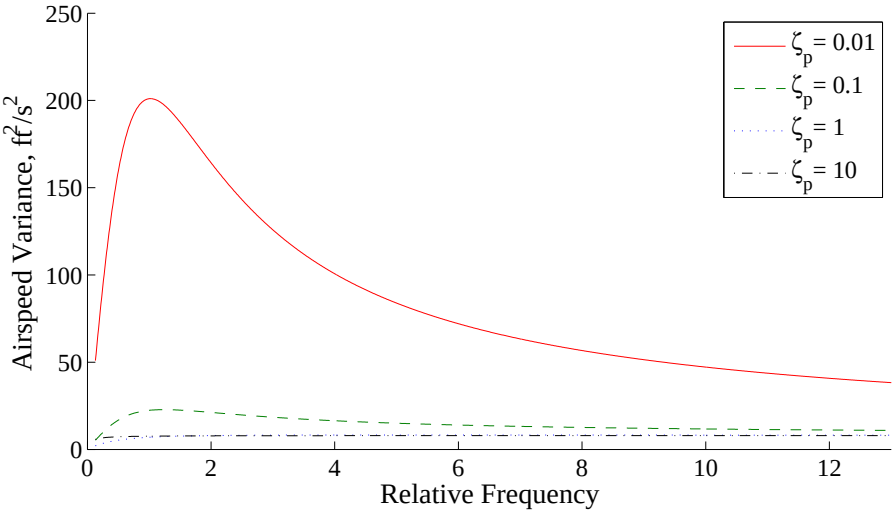

Figure 4.2: Plot of the airspeed variance versus the relative frequency of the phugoid mode to the turbulence parameterized by the phugoid damping ratio.

the GTM and T2 and goes up three orders of magnitude. This range of ζ_p allows us to speculate about the effects on the variances of feedback control to improve phugoid damping. Increasing ζ_p causes a decrease in σ_V^2 except for combinations of low values of κ and high values of ζ_p and causes an increase in σ_γ^2.

To investigate the peaks of both variances with respect to κ, we take the derivatives of σ_V^2 and σ_γ^2 with respect to κ and set them equal to zero. The peaks of σ_V^2 and σ_γ^2 occur, respectively, at

$$\kappa = 2\zeta_p + \sqrt{1 + 8\zeta_p^2}, \tag{4.22}$$

$$\kappa = 1. \tag{4.23}$$

The peaks indicate resonance between the turbulence and the aircraft taking place at these relative frequencies. For the airspeed variance, that resonance depends on the phugoid damping, but for the flight path angle variance, the phugoid damping does not matter.

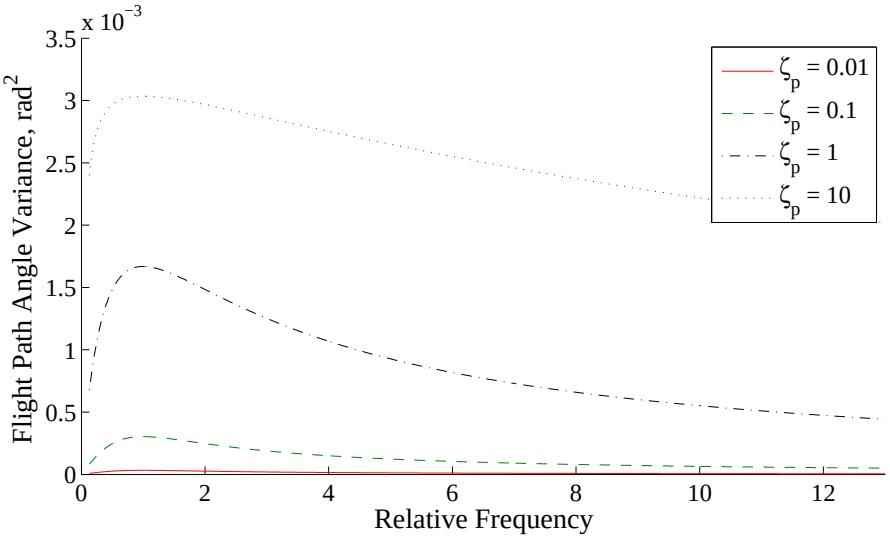

Figure 4.3: Plot of the flight path angle variance versus the relative frequency of the phugoid mode to the turbulence parameterized by the phugoid damping ratio.

4.3.3 Comparison with Hoblit Parameters

Recall from Section 2.6 that Hoblit describes the root mean square normal load factor in the short period approximation in terms of four dimensionless parameters,

$$\frac{\delta_{sp}}{L_w}, \quad \frac{\bar{c}}{\delta_{sp}}, \quad \frac{f_{sp}\delta_{sp}}{v_t}, \quad \zeta_{sp},$$

where L_w is the characteristic length of vertical gusts, $\bar{c}$ is the airplane chord length, f_{sp} is the short period natural frequency, ζ_{sp} is the short period damping ratio, and

$$\delta_{sp} \triangleq \frac{2m}{\rho S C_{L_\alpha}}, \tag{4.24}$$

a characteristic airplane length [15].

We do not consider here Hoblit's dimensionless parameter $\bar{c}/\delta_{sp}$ describing unsteady effects, though in Table C.2 in Appendix C quotes its value for the various airplanes used in the upcoming examples to show that unsteady effects should be small. In Eqs. (4.17)–(4.18) we see that, as in the short period approximation, the phugoid

damping ratio can be used as one of the dimensionless parameters to describe the response. As for Hoblit's other two dimensionless parameters, note that if we divide them, we get the dimensionless parameter $f_{sp}L_w/v_t$, a short period analog of κ defined in Eq. (4.19). Thus, in this dissertation's formulation of the gust response, these two dimensionless parameters of Hoblit only appear as a ratio, reducing the number of dimensionless parameters needed to characterize the response. As described in Szirtes and Rózsa, the number of curves and charts necessary to characterize a dependent variable in terms of a set of independent variables, not to mention the effort that goes into creating and using such charts, grows exponentially with the number of independent variables [36]. So, a reduction from four dimensionless parameters to three is a marked improvement.

4.4 Comparison of Airplane Responses to Turbulence

This section gives numerical examples of the results from the previous section. The numerical examples are based on the Dryden turbulence model and stability derivative models of two NASA airplanes. Some of the examples also include nine other airplanes. Appendix C gives detailed discussion of the parameters for the airplanes and the turbulence.

The first NASA airplane used is the GTM, a hypothetical airplane similar to a Boeing 757 used in computer simulations of transport aircraft [14]. The reference condition for the chosen parameters is steady level longitudinal flight at Mach 0.8 and an altitude of 35,000 ft. Figure 4.4 depicts the ARIES, a NASA-owned Boeing 757. The second NASA airplane used is the T2 subscale jet transport, a 5.5% dynamically scaled model of the GTM in operational use by NASA. Hence, $N = 0.05$ in Eq. (4.1a) when the GTM is the full scale aircraft and the T2 is the model. Jordan et al. [44] describe the design and construction of the T2. Most of the needed aircraft parameters for the T2 are tabulated in Morelli and Cunningham [13] and correspond to steady

level longitudinal flight at roughly 132 ft/s and an altitude of 1,400 ft. Figure 4.5 depicts the NASA T2.

4.4.1 Figure Format

Figures 4.6–4.8 show numerical examples of the dynamic scaling of different performance variables described in Section 4.3. In each of the figures, the values of the variables investigated are plotted by dynamically scaling the value for the GTM in steady level longitudinal flight in moderate turbulence at two altitudes using the scaling laws in Eqs. (4.1a)–(4.1f). The two altitudes chosen are 35,000 ft and 1,400 ft, typical cruise altitudes of the GTM and T2, respectively.

A choice of Mach 0.8 for the GTM at 1,400 ft is neither practical nor a good comparison to the cruising T2. For the curve corresponding to 1,400 ft, the GTM airspeed has been adjusted as follows. Assume that Mach 0.8 at 35,000 ft, or 782 ft/s, corresponds to the airspeed for minimum thrust v_{mt} for the GTM. According to McClamroch [33], the airspeed for minimum thrust in a jet aircraft is also the airspeed that minimizes the rate of fuel consumption and only depends on altitude via the air density. They are related as $v_{mt}(a) \propto \rho^{-1/2}(a)$, where a is again the altitude. Thus, the airspeed for minimum thrust at 1,400 ft is related to the air densities at 1,400 ft and 35,000 ft and the airspeed for minimum thrust at 35,000 ft as

$$v_{mt}(1400 \text{ ft}) = \sqrt{\frac{\rho(35000 \text{ ft})}{\rho(1400 \text{ ft})}} v_{mt}(35000 \text{ ft}). \tag{4.25}$$

Carrying out the computation, the GTM's airspeed for minimum thrust at 1,400 ft is 446 ft/s. This airspeed is used as the reference airspeed for the GTM in the curve showing dynamic scaling at 1,400 ft.

Along with the dynamic scaling curves, points are marked for the values of the GTM at 35,000 ft and the T2 at 1,400 ft. The dynamic scaling curves are plotted

Figure 4.4: The ARIES, a NASA-owned Boeing 757. The Boeing 757 is similar to the GTM. Image courtesy of NASA Langley Research Center.

Figure 4.5: The NASA T2. Image courtesy of NASA Langley Research Center.

using the analytical solutions from Section 4.3, while the points for the GTM and T2 are computed by forming the respective state space models and using a numerical Lyapunov solver. Two points are marked for each aircraft, one computed using the phugoid approximation of Eq. (4.16) and one computed using the full linearized model of Eq. (3.33).

4.4.2 Scaling of the Phugoid Mode

Equations (4.14) and (4.15) give scaling laws for the phugoid natural frequency and damping ratio, respectively. Figure 4.6 plots the phugoid natural frequency ω_{np} versus the scale factor N. The curves show how the GTM phugoid natural frequency scales dynamically based on Eq. (4.14) at 35,000 ft and 1,400 ft. The points marked show good agreement between the phugoid approximation and the full linearization phugoid natural frequency. The T2's phugoid approximation and full linearization also have similar phugoid natural frequencies. The T2's phugoid natural frequency is below that predicted by dynamically scaling the GTM with the T2 phugoid natural frequency about 15% below the predicted value, but it is well above the GTM's phugoid natural frequency at 35,000 ft. Any error must come from the difference in airspeed or coefficients of lift and drag, since the other airplane parameters match well and the altitude and turbulence parameters are the same for both.

Equation (4.15) shows that the phugoid damping ratio only depends on the length scale factor through the air density. Without a model of how the air density varies with length scale factor, the phugoid damping ratio cannot be plotted versus length scale factor. Instead, Table 4.1 shows the phugoid damping ratio for the GTM and T2 computed using the phugoid approximation and the full linearization. The GTM and T2 phugoid damping ratios are all of the same order of magnitude, with the phugoid approximations matching best. The natural frequency values in Table 4.1 correspond to the four points marked in Fig. 4.6.

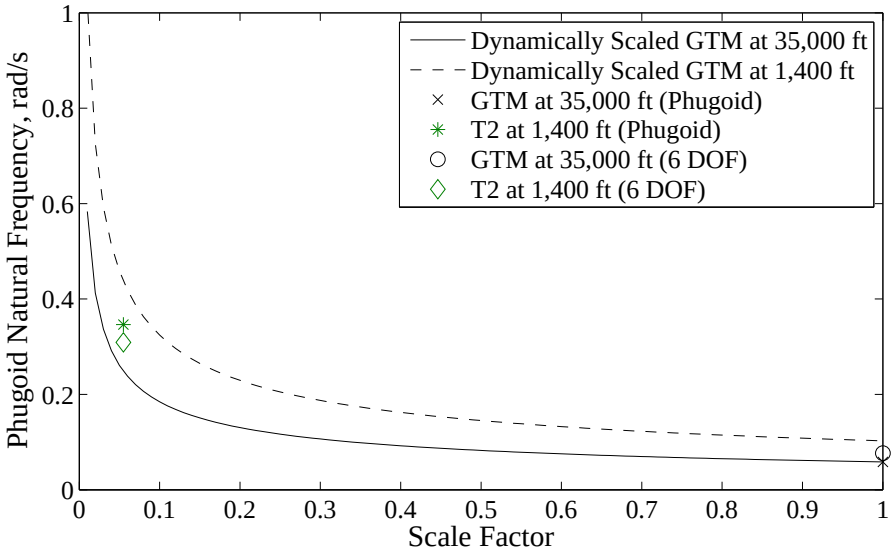

Figure 4.6: Phugoid natural frequency ω_{np} versus the scale factor N. Also plotted are values for the GTM and T2 using the phugoid approximation and the full 6 degree of freedom linearization.

4.4.3 Scaling of the Airspeed Variance

In Eq. (4.17), the variance of the airspeed depends on the airplane length scale factor through κ. Figure 4.7 shows how σ_V^2 varies with airplane length scale factor. At both altitudes, σ_V^2 is small for small and large airplanes and has a peak in between. For the T2, the phugoid approximation, the full linearization, and the scaled GTM are all close in variance. However, the difference between the airspeed variance in the phugoid approximation and the full linearization is substantial for the GTM. Validating these dynamic scaling curves from the phugoid model against the full linearization is left as future work.

To get a better sense of the magnitude of these variances, they should be normalized. A common way to measure uncertainty in a random variable is to compute its coefficient of variation: the standard deviation divided by the mean. Because Eq. (4.16) is a linear time invariant system driven by zero-mean white noise, the airspeed perturbations will also have zero mean. The mean airspeed will therefore equal

Table 4.1: Phugoid eigenvalue, damping ratio, and natural frequency for the GTM and T2 computed using the phugoid approximation and the full six-degree-of-freedom linearization.

Airplane	Model	Eigenvalue	ζ_p	ω_{np} rad/s
GTM	Phugoid	$-0.00257 \pm 0.0583i$	0.0440	0.0583
GTM	6 DOF	$-0.00185 \pm 0.0766i$	0.0241	0.0766
T2	Phugoid	$-0.0193 \pm 0.346i$	0.0558	0.346
T2	6 DOF	$-0.0283 \pm 0.307i$	0.0918	0.309

the reference airspeed of the linearization.

Scaling Law 3: Airspeed Coefficient of Variation *The coefficient of variation for the airspeed is σ_V/V. Figure 4.8 plots the airspeed coefficient of variation versus the scale factor.* □

Figure 4.8 shows that, after normalizing by the airspeed, the uncertainty in the airspeed decreases monotonically with increasing airplane size. The figure also shows that the disagreement in airspeed variance between the phugoid approximation and the full linearization lessens after normalization. The T2's coefficient of variation from the phugoid approximation is about 16% below the value for the scaled GTM but is well above the GTM's coefficient of variation at 35,000 ft. A later example shows better agreement when the airspeed of the scaled GTM is used for the T2 instead of the airspeed from the parameter source. Recall from Eq. (4.1e) that $V \propto N^{1/2}$. The coefficient of variation exhibits the airspeed's strong dependence on length scale factor but is adjusted because of the dependence of σ_V on the length scale factor.

To consider how the dynamically scaled GTM compares to the other types of airplanes, consider again Fig. 1.1 from the introduction, variations of which are presented in Fig. 4.9. Figure 4.9 shows values for the airspeed variance and coefficient of variation for a variety of aircraft, all computed at 1,400 ft using the phugoid approximation. The solid curve represents the dynamically scaled, analytically determined GTM value. The dashed curve represents the dynamically scaled, analytically deter-

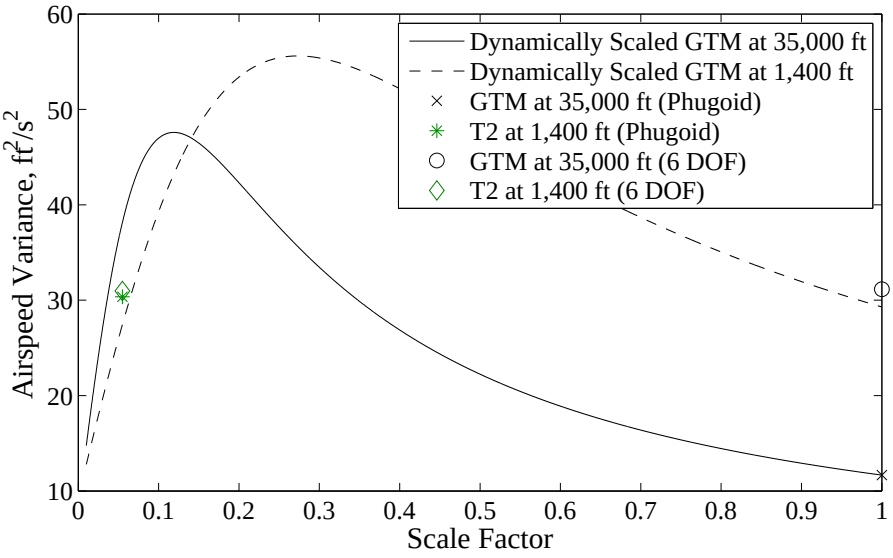

Figure 4.7: Airspeed variance σ_V^2 versus the scale factor N. Also plotted are values for the GTM and T2 using the phugoid approximation and the full 6 degree of freedom linearization.

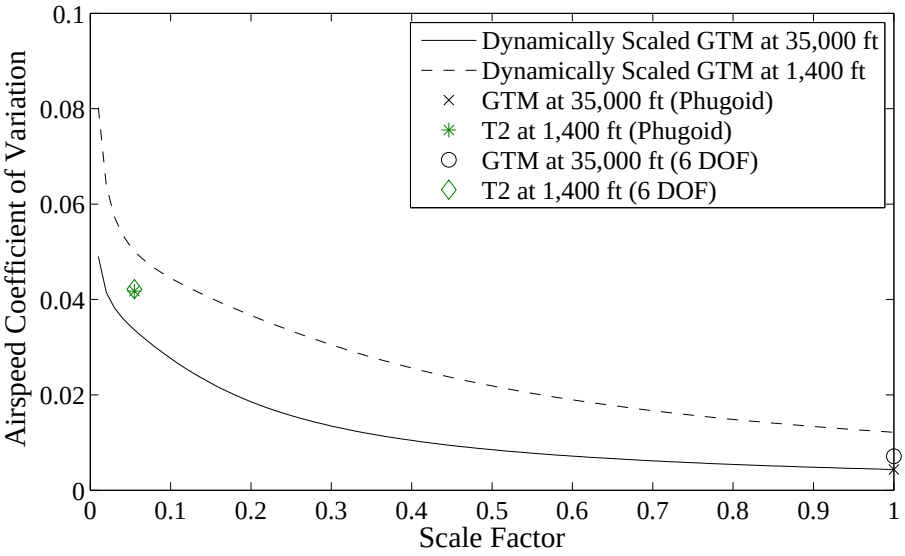

Figure 4.8: Coefficient of variation of the airspeed σ_V/V versus the scale factor N. Also plotted are values for the GTM and T2 using the phugoid approximation and the full 6 degree of freedom linearization.

mined C-5A value. The numerically determined GTM and C-5 values are marked with $\times$ on the curves. All of the other plotted points correspond to numerically determined values for the indicated airplanes.

Both the airspeed variance and coefficient of variation depend on the reference airspeed. The speed scaling law in Eq. (4.1e) suggests a simple relationship between airspeeds at different airplane sizes. In reality, aircraft can operate at a wide range of airspeeds, and design considerations other than length scale, such as weight and engine performance, play an important role in determining airspeed.

Compare, for example, the Navion general aviation aircraft and the A-4D fighter. The Navion's wingspan is 33.4 ft and the A-4D's is 27.5 ft. We estimate that, at an altitude of 1,400 ft, the Navion's airspeed for minimum fuel consumption is 100 ft/s and the A-4D's is 402 ft/s. Scaling the GTM down to the size of the A-4D, we expect an airspeed for minimum fuel consumption of 209 ft/s. To eliminate this variability, the scaled GTM's airspeed is used for all of the airplanes in Figs. 4.9. This includes adjusting the T2's airspeed, and improves agreement between the T2 and the scaled GTM compared to the previous examples. Airplane weight exhibits similar variability, but the figures do not account for deviations of airplane weight from the scaling laws.

In Fig. 4.9, the length scale factor again corresponds to the relative wingspan. While studying the figures, note the following:

- The T2 matches the scaled GTM's curves well, better than the previous examples where the airspeed from the T2 parameters' source was used
- Neither fighter matches the scaled transports well
- Both the GTM and T2 appear to be unusually sensitive to gusts for aircraft at their wingspans
- The Navion's airspeed variance is lower than the scaled GTM's or the scaled

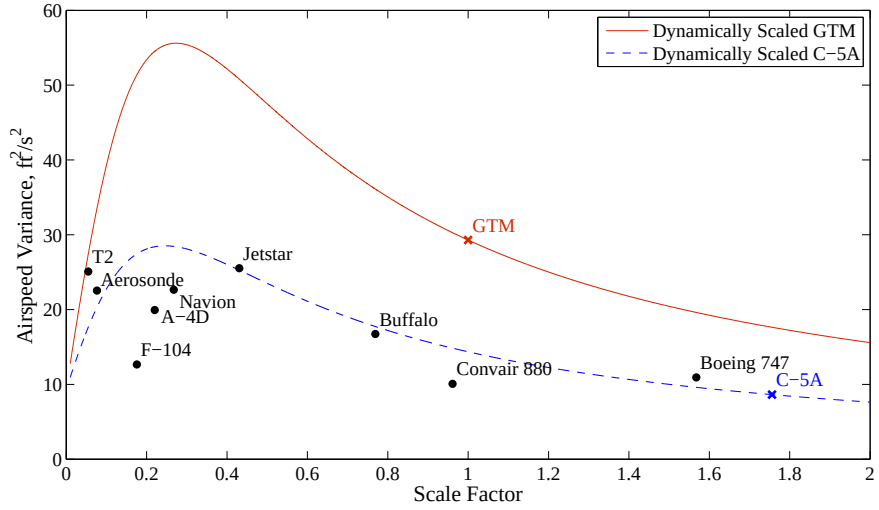

(a)

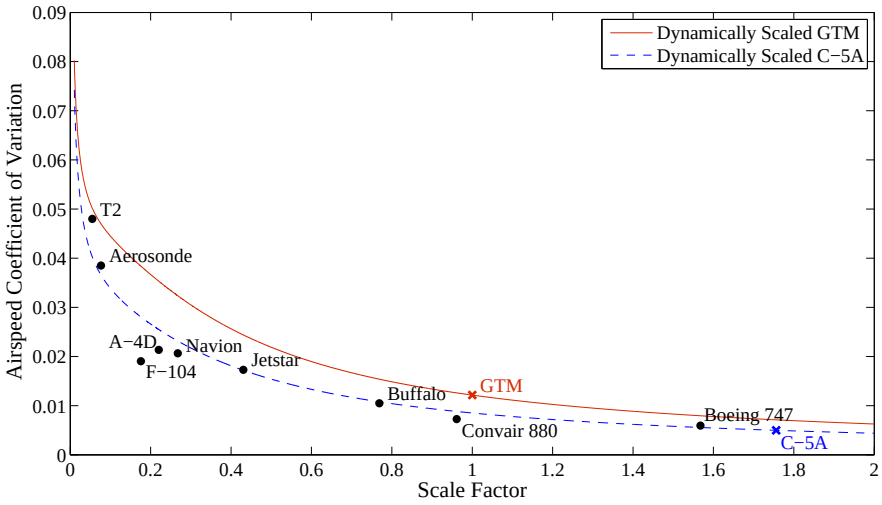

(b)

Figure 4.9: Airspeed variance σ_V and coefficient of variation σ_V/V for eleven airplanes versus the wingspan scale factor N computed using the phugoid approximation at 1,400 ft.

C-5A's

- The rest of the aircraft follow the trend of the dynamically scaled C-5A

The poor agreement between the scaling law and the fighters is expected for the reasons described earlier related to performance of the fighters compared to performance of transport aircraft their size. The fighters, the Navion, and the Convair 880 have less airspeed variation than the scaled C-5A while the GTM and T2 have more; all of these deviations from the scaled C-5A can be explained by comparing the airplanes' phugoid damping ratios.

Table C.2 in Appendix C lists for each airplane in Fig. 4.9 the values of κ, the GTM's scaled value of κ, and ζ_p. While the scaled GTM's κ does not predict the values of κ for the other airplanes well, the trends match. As for the phugoid damping ratio, according to Eq. (4.15) it should be the same for all airplanes at fixed altitude, but it clearly varies between the different aircraft types. Moreover, these are open-loop phugoid damping ratios, so they can be expected to vary further with a controller. For every airplane in Fig. 4.9, the damping ratio relative to the C-5A's determines whether the airspeed variance and coefficient of variation are above or below the C-5A's dynamically scaled value. Furthermore, the GTM and the F-104, which have the lowest and highest damping ratios, respectively, are the most significant outliers. Thus, the dependence of the airspeed variance on ζ_p and the difference between the various airplanes' values for ζ_p limit the accuracy of the scaling laws.

4.4.4 Other Length Scale Factors

Relative wingspan is one of many potential length scale factors to use for these scaling laws. This section compares scaling based on relative wingspan with scaling based on relative wing loading and relative weight.

In some applications, the wing loading $^{mg}/_{S}$ is the preferred length scale factor, as in Tennekes' Great Flight Diagram [45]. In fact, the wing loading is very relevant to

this problem since Eqs. (4.14)–(4.15) show that the phugoid natural frequency and damping ratio can be written in terms of wing loading. While wing loading is not a length, the scaling laws in Eqs. (4.1b)–(4.1c) show that it should scale proportional to length.

Figure 4.10 shows the same scaling laws as Fig. 4.9 except with the length scale factor and the chosen airspeeds corresponding to relative wing loading. Note that even though the T2 is designed as a 5.5% dynamically scaled model of the GTM, its relative wing loading actually corresponds to a relative wing loading length scale factor of 8.7%. Also note that the T2's reference airspeed from the source of the parameters [13] and the scaled GTM's airspeed based on relative wing loading differ by less than 3%. Therefore, the T2's airspeed variance and coefficient of variation do not change significantly from the examples earlier that use the airspeed given in the T2 parameters' source.

From the plots, the trends shown in the previous examples are apparent, with the F-104 and the GTM still being outliers and the smallest airplanes having the largest airspeed coefficients of variation. With the exception of the F-104, all of the aircraft's variances and coefficients of variation are bounded by those of the dynamically scaled GTM and C-5A. However, neither the dynamically scaled GTM nor the dynamically scaled C-5A capture the precise values of the other aircraft, especially for the variance, when compared with using the relative wingspan for the length scale factor.

Another preferred length scale factor is the cube root of the airplane mass, $\sqrt[3]{m}$, as in Liu [51]. Like wing loading, the cube root of the mass is not a length but scales proportional to length, as seen in Eq. (4.1c). Also like wing loading, the mass features prominently in the phugoid approximation, suggesting it should also be a more relevant length scale than wingspan.

Figure 4.11 shows the same scaling laws as Figs. 4.9 and 4.10, except with the length scale factor and the chosen airspeeds corresponding to the cube root of the

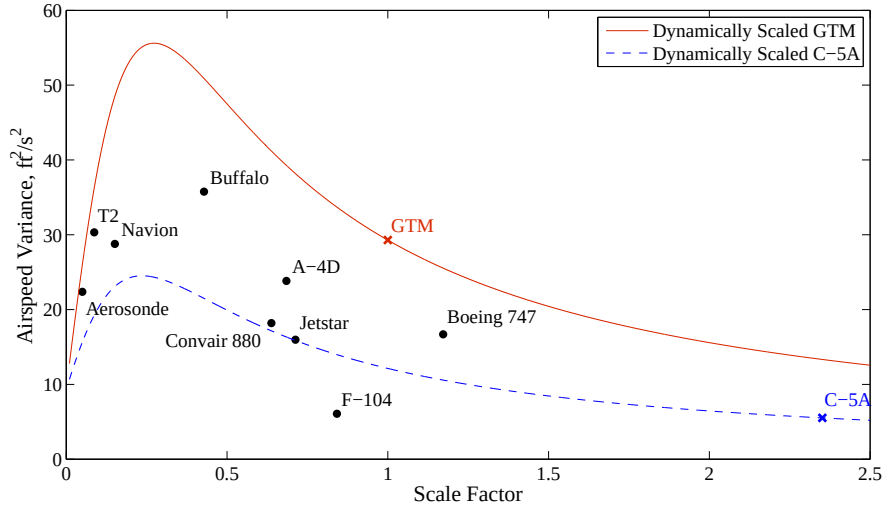

(a)

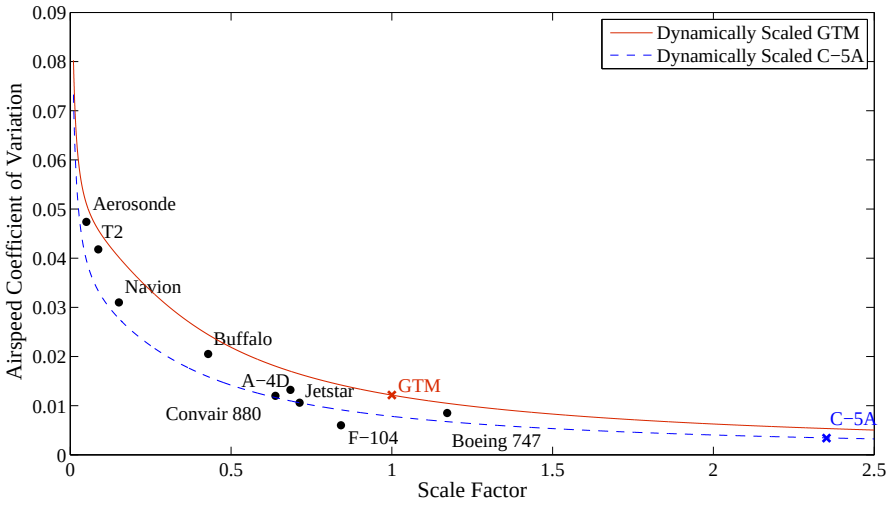

(b)

Figure 4.10: Airspeed variance σ_V and coefficient of variation σ_V/V for eleven airplanes versus the wing loading scale factor N computed using the phugoid approximation at 1,400 ft.

relative mass. Using this length scale factor, the trends and major outliers remain the same. For the airspeed variance, the scaled C-5A and the other aircraft show better agreement than when scaled by wing loading, but relative wingspan still provides the best fit and agreement related to the damping ratio. Scaling based on relative weight results in better agreement between the airspeed coefficient of variation scaling law and numerical solution compared to scaling based on relative wing loading, but it is not clear if it is an improvement over scaling based on relative wingspan. Overall, the scaling laws in this dissertation are good predictors of the statistics of airspeed variations due to turbulence in the phugoid approximation, particularly the airspeed coefficient of variation. Furthermore, the examples suggest that relative wingspan is a better measure of length scale than wing loading for this set of scaling laws.

4.5 Summary

Using a phugoid approximation of the linearized airplane dynamic equations, this chapter derives scaling laws for the phugoid mode natural frequency and damping ratio as well as expressions for the airspeed and flight path angle variances. It also gives numerical examples of the results of the phugoid analysis and compares them to stability derivative models of the NASA GTM and T2. The numerical results include plots showing how the airspeed coefficient of variation scales with airplane size and compare the T2 and dynamically scaled GTM to a variety of other airplanes.

Using two metrics, the results show that small airplanes are more susceptible to turbulence than large airplanes. First, the scaling of the phugoid natural frequency shows that the dynamics of large airplane filter out more high frequency gusts than the dynamics of smaller airplanes. Second, the coefficient of variation for airspeed decreases as airplanes get larger, showing that variations in airspeed due to turbulence, when expressed as a fraction of the nominal airspeed, are smaller for large airplanes. This scaling law, which from a qualitative standpoint is intuitive, reemphasizes the

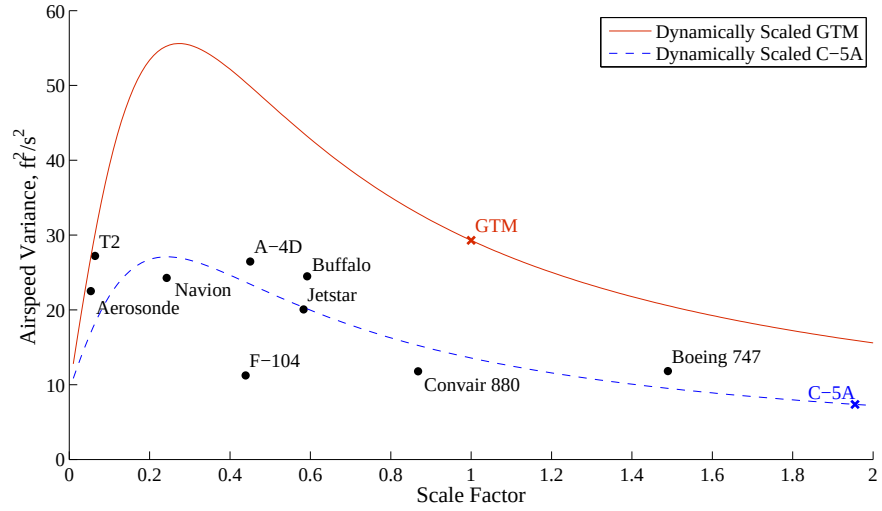

(a)

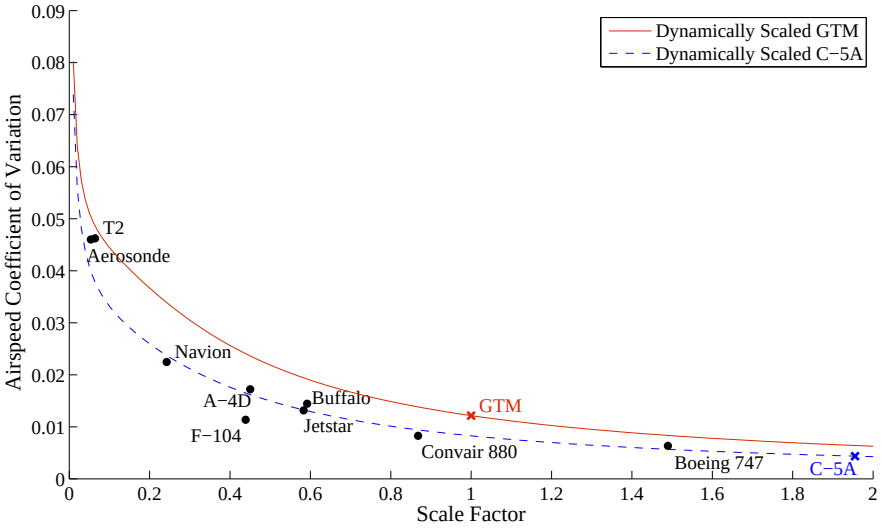

(b)

Figure 4.11: Airspeed variance σ_V and coefficient of variation $^{\sigma_V}/_V$ for eleven airplanes versus the cube root of the weight scale factor N computed using the phugoid approximation at 1,400 ft.

need to make autopilots on small airplanes robust with respect to turbulence and raises the complementary question of whether small scale airplanes are more or less capable of alleviating gust response with control action.

These scaling laws provide a quantitative basis to compare gust responses of airplanes of different sizes. Such a comparison can improve understanding of gust response at different length scales. It can also help pilots using the same airspace in airplanes of different sizes trade information about gust conditions and expected response. As small aircraft become more prevalent in military and commercial applications, these scaling laws can serve as useful tools to predict and improve airplane performance in gusts.

CHAPTER V

Envelopes for Flight Through Stochastic Gusts

5.1 Introduction

This chapter uses the model derived in Chap. III to introduce the notion of *stationary flight* and the *stationary flight envelope*. This chapter describes how to use the linear velocity covariance matrix generated at the end of Chap. III to quantify airplane performance in stochastic gusts. In particular, this chapter describes how to compute the probability that steady flight constraints are violated given the covariance matrix and the airplane model. This leads to the stationary flight envelope, an adjustment of the steady flight envelope for use when the airplane's state is a stationary random process. The stationary flight envelope allows visualization of the probability of an airplane violating a steady flight constraint because of turbulence.

Section 5.2 describes applications of the model derived in Chap. III to compute safety margins for steady flight in turbulence. Section 5.2 also introduces the notion of stationary flight and the stationary flight envelope. Section 5.3 gives numerical examples for a Navion general aviation aircraft performing various steady flight maneuvers in moderate turbulence, including examples of gust alleviation using feedback control. Through analysis of the example, the section shows what guarantees can be made about steady flight in uncertain wind conditions, both in terms of true airspeed and normal load factor perturbations. The chapter ends by providing brief, illus-

trative examples of a small, unmanned airplane's stationary flight envelope and the Navion stationary flight envelope when the gusts are generated using the von Kármán model.

5.2 Safety Margins for Stationary Flight

Chapter III presents linearized airplane dynamic equations that include a gust coloring filter and, in some cases, state feedback and an observer. In either the open- or closed-loop case, a covariance matrix P is computed using a Lyapunov equation. This matrix P is the covariance of the vector $(\delta v_t \quad \delta\alpha \quad \delta n)^{\mathrm{T}}$, the true airspeed, the angle of attack, and the normal load factor. Appendix A defines these three quantities and derives their perturbations from the perturbations of the airplane and wind linear velocities. After determining the covariance matrix P, the effect of wind gusts on steady flight can be quantified.

The Cessna 172 Pilot Information Manual [71] provides an example where quantifying performance to meet a desired stall safety margin might be beneficial. For a normal landing, the manual states:

> "Normal landing approaches can be made with power on or power off with any flap setting within the flap airspeed limits. Surface winds and air turbulence are usually the primary factors in determining the most comfortable approach speeds." [71]

Later, the manual states:

> "For a short field landing in smooth air conditions, approach at 61 KIAS with FULL flaps using enough power to control the glide path. Slightly higher approach speeds should be used in turbulent air conditions." [71]

Pilots might benefit if the manual included information describing how much to adjust the approach speed for a particular severity of turbulence. Similarly, the manual

could show the stall curves or adjusted steady flight envelopes for an approach in turbulence. In this manner, the manual could quantify how to adjust the approach speed in turbulence. Of course, these and similar adjustments to airspeed to account for turbulence must be traded off against other constraints, such as landing and takeoff distances. When weighing the airspeed adjustment for turbulence against other constraints, quantifying the reduction in the flight envelope due to turbulence would help identify flight plans that are not flyable in turbulence with the desired margin of safety.

5.2.1 Stationary Flight and the Stationary Flight Envelope

To help predict safe flight conditions when facing turbulence, we propose use of the terms *stationary flight* and *stationary flight envelope*. Stationary flight is a flight state where the airplane's linear and angular velocities are stationary random processes. Equation (3.33) is an example of a system whose flight state is stationary. A stationary flight state is defined by its covariance matrix for the state variables and a reference steady flight state that is the mean. A stationary flight envelope is an adjusted version of the steady flight envelope for use in the case of stationary flight. It is defined as the set of stationary flight states where the instantaneous probability of exceeding a steady flight constraint is less than some specified value. It can equivalently be defined as the set of stationary flight states where the logarithmic residence time in the steady flight envelope is less than some specified value. It is formed by shifting the boundaries of the steady flight envelope inward as a function of the variances of the airplane's true airspeed and normal load factor to achieve the desired safety margin. For the case of steady level longitudinal flight, a stationary flight envelope can be formed by shifting the steady flight envelope inward by three standard deviations of the fluctuations of the airspeed.

Section 1.1 gives an illustration of a stationary flight envelope in Fig. 1.2, repro-

duced for convenience here as Fig. 5.1. In this open-loop, low-speed example, the reference flight state is steady flight with both zero flight path angle and zero bank angle. In their most general form, the linear and angular velocities in steady flight depend on the flight path angle γ and the bank angle around the velocity vector μ as

$$v_c = V \begin{pmatrix} \cos\alpha \\ 0 \\ \sin\alpha \end{pmatrix}, \qquad \omega = \frac{g}{V} \tan\mu \begin{pmatrix} -\sin\gamma\cos\alpha - \cos\gamma\cos\mu\sin\alpha \\ \cos\gamma\sin\mu \\ \cos\gamma\cos\mu\cos\alpha - \sin\gamma\sin\alpha \end{pmatrix}, \tag{5.1}$$

where the angle of attack α is related to μ by

$$\alpha = \frac{1}{C_{L_\alpha}} \left(\frac{2mg}{\rho V^2 S \cos\mu} - C_{L_0} \right). \tag{5.2}$$

For steady level longitudinal flight, Eq. (5.1) simplifies to the reference condition

$$v_c = \begin{pmatrix} u \\ 0 \\ w \end{pmatrix}, \qquad \omega = \begin{pmatrix} 0 \\ 0 \\ 0 \end{pmatrix}. \tag{5.3}$$

Figure 5.2, illustrations adapted from McClamroch [33], shows steady climbing turn of an airplane from several perspectives, with the relevant angles and coordinate frames included. Figure 3.1 in Chap. III depicts the orientation of the body frame with respect to the Earth frame along with the yaw, pitch, and roll Euler angles (ψ, θ, ϕ). By analogy, Fig. 3.1 also shows the heading, flight path, and bank Euler angles (σ, γ, μ) that transform the Earth frame to the wind frame as well as the angles of sideslip, attack, and zero $(\beta, \alpha, 0)$ that transform the wind frame to the body frame.

As discussed in Section 2.4, steady flight is constrained by maximum engine output, angle of attack, and normal load factor. In steady flight, the maximum angle of attack corresponds to a minimum true airspeed and the maximum engine output

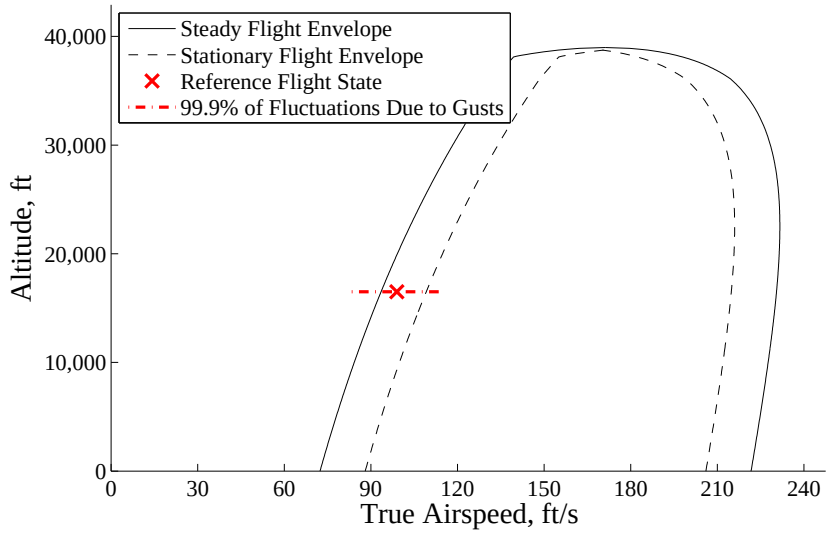

Figure 5.1: Illustration of the steady and stationary flight envelopes for an airplane flying through turbulence.

corresponds to maximum and minimum true airspeeds. The diagonal entries of the covariance matrix P are $\begin{pmatrix}\sigma_{v_t}^2 & \sigma_\alpha^2 & \sigma_n^2\end{pmatrix}$, the variances of the true airspeed, the angle of attack, and the normal load factor, respectively. Therefore, the diagonal entries of P describe the statistics of variables that are bounded in steady flight.

5.2.2 Quantifying the Probability of Flight Envelope Departures

In this section, we consider three methods to quantify the probability that the system in Eq. (3.33) exceeds a steady flight constraint. Each method applies to the true airspeed, the angle of attack, and the normal load factor. For convenience, each method is only explained in terms of the true airspeed.

5.2.2.1 Instantaneous Probability of Exceedance

Consider an airplane in turbulence with a steady flight reference true airspeed v_t and true airspeed fluctuations with zero mean and variance $\sigma_{v_t}^2$. The probability p that at a particular instant the true airspeed's value is less than k standard deviations

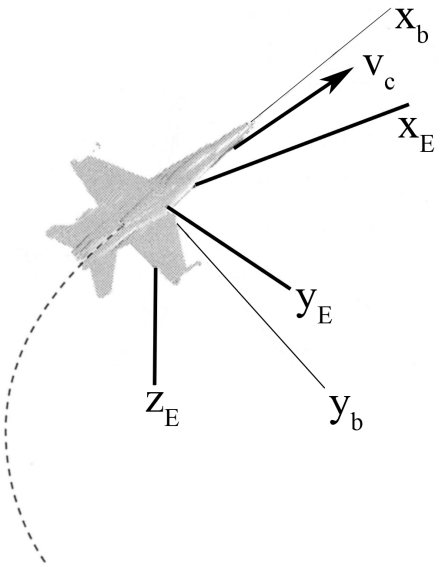

(a) Three dimensional view of an airplane in a climbing turn.

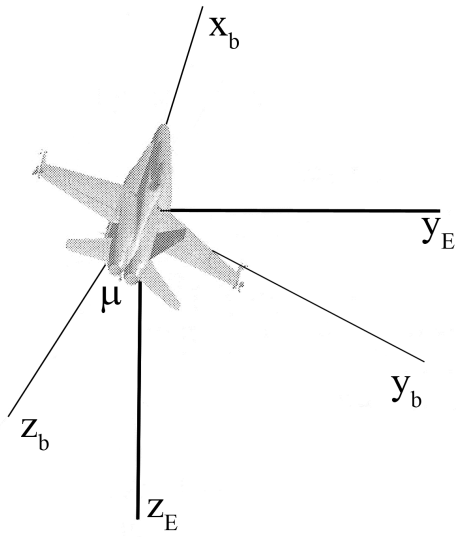

(b) View in the direction of the velocity vector of an airplane in a climbing turn.

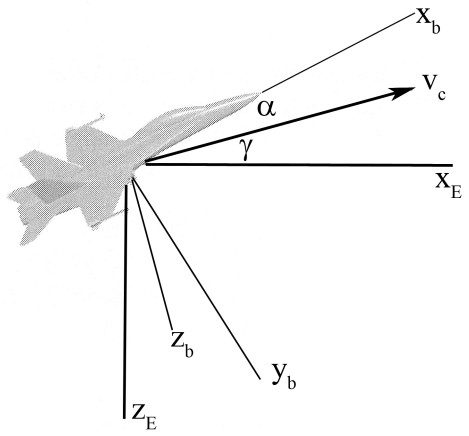

(c) View in the $-y_E$-axis direction of an airplane in a climbing turn.

Figure 5.2: Illustration of the Earth and body frame axes in a climbing turn adapted from McClamroch [33]. Also shown are the flight path angle γ, the bank angle around the velocity vector μ, and the angle of attack α.

below or greater than k standard deviations above the mean can be computed from the Gaussian distribution's cumulative distribution function. Because of the symmetry of the Gaussian distribution, both probabilities are given by

$$p\left(v_t + \delta v_t \leq v_t - k\sigma_{v_t}\right) = \mathrm{p}\left(v_t + \delta v_t \geq v_t + k\sigma_{v_t}\right) = \frac{1}{2}\left(1 - \mathrm{erf}\left({}^{k}/_{\sqrt{2}}\right)\right), \tag{5.4}$$

where $\mathrm{erf}({}^{k}/_{\sqrt{2}})$ is the error function. For ergodic random processes, which we presume, p is also the fraction of time that the process spends k standard deviations above or below the mean. So, for example, if the stall speed were exactly two standard deviations less than v_t, i.e., $k = 2$, then, as the airspeed randomly fluctuated, the airplane would slow to below the stall speed at most 2.3% of the time. If it were three standard deviations less than v_t, the plane would slow below the stall speed 0.13% of the time. Figure 5.4 gives an illustration.

This instantaneous probability of exceeding the flight envelope, or equivalently the fraction of time spent outside of the flight envelope, is referred to as a safety margin in the rest of this chapter. This safety margin can be set by the number of standard deviations of flight state fluctuations lying between the reference state and the steady flight envelope boundaries.

5.2.2.2 Flight Envelope Logarithmic Residence Time

Consider again stationary flight with a true airspeed that is a stationary random process with distribution $\mathcal{N}(v_t, \sigma_{v_t}^2)$. Another safety margin to consider is the expected value for the time of the first flight envelope departure, called the residence time. The first section of Appendix B derives an approximation for the residence time within the flight envelope. It also derives an exact value for the logarithmic residence time, a constant of a random process related to the natural log of the residence time and useful in residence time control applications [72, 73].

Denote the logarithmic residence time of the true airspeed $\hat{\mu}_{v_t}$. Suppose that the minimum steady flight true airspeed is $v_t - k_{\min}\sigma_{v_t}$ and the maximum steady flight true airspeed is $v_t + k_{\max}\sigma_{v_t}$. Then,

$$\hat{\mu}_{v_t} = \frac{1}{2}\min(k_{\min}, k_{\max})^2. \tag{5.5}$$

This dimensionless logarithmic residence time grows monotonically with the residence time and does not require computation of the proportionality constant needed to find the actual residence time. Like the safety margin in the previous section, the logarithmic residence time is directly related to the number of standard deviations between the steady flight reference value and value at the steady flight envelope boundary. For flight states no less than 3 standard deviations away from the flight envelope boundary, the logarithmic residence time is guaranteed to be at least 4.5.

5.2.2.3 Probability of Exceedance Per Unit Time

In many applications it is desirable to know the probability that the flight envelope will be exceeded during a given time interval. The second section of Appendix B derives this probability and gives it in Eq. (B.14). Consider again stationary flight with a true airspeed that is a stationary random process with distribution $\mathcal{N}(v_t, \sigma_{v_t}^2)$. Suppose that the minimum steady flight true airspeed is $v_t - k_{\min}\sigma_{v_t}$ and the maximum steady flight true airspeed is $v_t + k_{\max}\sigma_{v_t}$. Then,

$$p_{\text{ex}}(t) = 1 - e^{-N_{v_t}(k_{\min}, k_{\max})t}, \tag{5.6}$$

$$N_{v_t}(k_{\min}, k_{\max}) = N_{0,v_t} e^{-\hat{\mu}_{v_t}}, \tag{5.7}$$

where $N_{v_t}(k_{\min}, k_{\max})$ is the frequency of $|\delta v_t|$ exceeding $k_{\min}$ or $k_{\max}$–whichever is smaller–per unit time, $\hat{\mu}$ is given in Eq. (5.5), and N_{0,v_t} is the frequency with which δv_t crosses 0 with positive slope. N_{0,v_t} is related to the proportionality constant

described earlier for the residence time and can only be estimated in many flight dynamics applications. Equation (B.12) shows how to compute N_{0,v_t} from the power spectral density of δv_t.

For small $N_{v_t}(k_{\min}, k_{\max})t$, as in the case where v_t is many standard deviations away from the flight envelope boundaries,

$$p_{\text{ex}}(t) \approx N_{v_t}(k_{\min}, k_{\max})t, \tag{5.8}$$

and $N_{v_t}(k_{\min}, k_{\max})$ is approximately equal to the probability of exceedance per unit time, $p_{\text{ex}}(t)/t$.

All three of the preceding measures of the probability of exceeding the flight envelope can be developed for the angle of attack and the normal load factor. The normal load factor's safety margin is discussed later. The angle of attack safety margin applies to stall, as does the true airspeed safety margin. In the examples of the next section, for reference states near the stall boundary, stall safety margins based on the true airspeed and the angle of attack give the same stall speed to within 3%. Furthermore, we prefer to use the steady flight envelope, which plots true airspeed on one axis. Therefore, this dissertation uses the true airspeed variance to compute stall safety margins. Detailed comparison of the merits of each approach is left for future study.

5.2.3 Flight Envelope Departures Other Than Stall

Until this point, we have mainly discussed true airspeed fluctuations, especially for avoiding stall, but we propose shifting all boundaries of the steady flight envelope inward. This inward shift creates a stationary flight envelope that provides a quantitative safety margin that corresponds to the turbulence level. A set of constraints determines the boundaries of the steady flight envelope, namely maximum values of

power, angle of attack, and normal load factor. Exceeding any of these constraints puts the airplane in a flight state where steady flight cannot be guaranteed, and therefore the control and structural integrity of the airplane are at risk. In Fig. 5.1, the angle of attack constraint determines most of the minimum airspeed boundary, while the propulsion constraint determines the rest. For this airplane, the normal load factor constraint only limits the maximum bank angle in steady turns. In general, the normal load factor limits the high-speed performance of many aircraft. Returning to the Cessna 172 manual, a table under "Airspeeds for Normal Operation" shows the "Maximum Recommended Turbulent Air Penetration Speed" parameterized by airplane weight [71]. These airspeeds can also be computed and depicted using the methods herein. The next section goes through detailed examples of for a Navion.

Limits on the normal load factor are typically displayed on v-n diagrams, plots of normal load factor versus airspeed demarcating steady flight states. v-n diagrams at fixed altitude and flight path angle are two dimensional cross-sections of the full steady flight envelope. σ_n^2 can be used to shift inward the wing loading boundaries and form the stationary flight envelope.

The propulsion constraint limits airplane thrust or power, depending on the engine type. For the reciprocating engine of the Navion, we can model the propulsion constraint as a maximum engine power [33]. Exceeding the propulsion constraint implies that the airplane cannot provide sufficient power to maintain its flight state. While this excursion is not as dangerous as stalling or overloading, it puts the airplane in a state that cannot be maintained steadily. Suppose that turbulence changed the airplane's airspeed, resulting in the airplane flying out of equilibrium. If the airplane were out of equilibrium but the new combination of airspeed, altitude, flight path angle, and bank angle were within the steady flight envelope, then the pilot could adjust the control inputs to equilibrate the aircraft in the new state and then adjust the inputs again to transition back to the desired state. If the airplane were out of

equilibrium and had crossed the propulsion boundary, the pilot would have less control over equilibration of the flight state and might struggle to maintain the desired reference state. Staying within the stationary flight envelope reduces the probability of this occurring. Regardless of the utility, the adjustment of the propulsion boundary is an available safety margin for flight through turbulence. In practice, a less stringent safety margin, or no margin at all, may be acceptable to the operator for this steady flight constraint compared to the others.

As a consequence of shifting the low and high speed boundaries of the flight envelope inward, the flight ceiling is also reduced. This downward shift of the flight ceiling is not a reduction based on the fluctuations of the altitude, nor is it a reflection of the risks of exceeding the flight ceiling. Flight states near the flight ceiling are necessarily close to the low and high speed boundaries of the flight envelope. The inward shift of those boundaries therefore excludes states near the flight ceiling. Even if, in applications, it is decided not to shift the propulsion boundary inward, the inward shift of the stall boundary may still cause this reduction in flight ceiling.

In summary, when planning a flight through known turbulent conditions, or upon encountering turbulence and flight state perturbations whose statistics can be estimated, a pilot can adjust the airplane's steady flight state to ensure that the state lies within the stationary flight envelope. For an inward shift of three standard deviations, flying within the stationary flight envelope guarantees that the airplane stays within the steady flight envelope at least 99.87% of the time and also guarantees a logarithmic residence time above 4.5. The three standard deviation adjustment is arbitrary and can be changed on each boundary to generate the desired safety margin for each type of envelope excursion.

Figure 5.3: Ryan Navion on display at the Air Force Museum.

5.3 Envelopes for a General Aviation Aircraft

This section details a specific example of the model just derived. The application centers on a Ryan Navion general aviation aircraft model from [30]. Figure 5.3 shows a picture of a Navion on display at the Air Force Museum. Table C.1 in Appendix C summarizes the necessary parameters. This airplane model only offers one steady flight state's stability and control derivatives, but we use them for all steady flight states. This likely detracts from the validity of the numerical results. However, the examples below still provide valuable illustrations of how to apply the method. Applications of this method could be improved by using airplane models that offer multiple states' derivatives spanning the relevant portions of the flight envelope.

A variant of the algorithm published in [33] enables calculation of the flight envelope boundaries. The steady flight envelopes are plotted by computing what combinations of airspeed, altitude, bank angle, and flight path angle mark the boundaries of the steady flight constraints: maximum angle of attack, maximum power, and maximum normal load factor. The stationary flight envelopes are plotted by shifting the boundaries of the steady flight envelope based on the statistics of the flight state.

The example uses high altitude turbulence, which MIL-HDBK-1797 defines as valid starting 2,000 ft above terrain [19]. For high altitude turbulence, the turbulence axes are defined to coincide with the airplane axes. For the noise, the example uses a filter for continuous Dryden gusts given in [67]. Table C.3, also in Appendix C, gives the parameters describing the turbulence and coloring filter. The example assumes that the average wind velocity is zero, i.e., $v_w = \omega_w = 0$.

In certain parts of the flight envelope, including all longitudinal flight states, this Navion model has one unstable mode in the system of Eq. (3.30). Therefore, open-loop covariances cannot be computed for these states and the model must be stabilized. The stabilization is achieved using the controller design of Section 3.6. For the LQR weight matrix Q, define a weight matrix Q_a for the system in Eq. (3.30) as

$$Q_a = q \begin{pmatrix} \mathbb{1}_6 & 0 \\ 0 & 0 \end{pmatrix}, \tag{5.9}$$

where q is some scalar. We form Q from Q_a by appending zeros for the coloring filter states,

$$Q = \begin{pmatrix} Q_a & 0 \\ 0 & 0 \end{pmatrix}. \tag{5.10}$$

The LQR weight matrix R and the Kalman filter measurement noise covariance S_{meas} are chosen as

$$R = \mathbb{1}_3, \tag{5.11}$$

$$S_{\text{meas}} = \mathbb{1}_6, \tag{5.12}$$

where S_{meas} is chosen such that the measurement noise in the simulations is about an order of magnitude smaller than the fluctuations caused by the gusts. These choices and $q = 10$ allow stabilization of the dynamics. For consistency, all of the

Navion examples use this controller regardless of whether they are stable without the controller.

5.3.1 Steady Level Longitudinal Flight

Consider steady level longitudinal flight in moderate turbulence with a reference airspeed of 102 ft/s at an altitude of 16,500 ft. This is an unusual state in which to operate a Navion, but it is in the flight envelope and provides a good illustration. Given this airplane model, turbulence model, and reference flight state, the variance of the true airspeed $\sigma_{v_t}^2$ can be computed to be 15 ft^2/s^2. With this information, the stationary flight envelope can be plotted by shifting the steady flight envelope inwards by three standard deviations, $3\sigma_{v_t}$, as shown in Fig. 5.4. For the reference state depicted inside the stationary flight envelope, the airspeed is guaranteed to stray outside the steady flight envelope at most 0.13% of the time as it fluctuates due to the turbulence. That state is also guaranteed to have a logarithmic residence time of at least 4.5. For the state depicted outside the stationary flight envelope, the airspeed leaves the flight envelope between 0.13% and 50% of the time and the logarithmic residence time is less than 4.5.

For other choices of safety margin, the stationary flight envelope is a different size. Equation (5.4) shows the relationship between probability of departing the steady flight envelope and the number of true airspeed standard deviations between v_t and the stall speed. Figure 5.5 shows several stationary flight envelopes corresponding to different probabilities of instantaneously dropping below the stall speed, the safety margin in question in this example. Only the safety margin is varied to generate each of the figure's stationary flight envelopes. Note that as the probability of departing the envelope decreases, the number of standard deviations required to meet that safety margin increases but more slowly. For example, decreasing the probability from 10^{-3} to 10^{-6} results in less than three standard deviations worth of additional inward shift

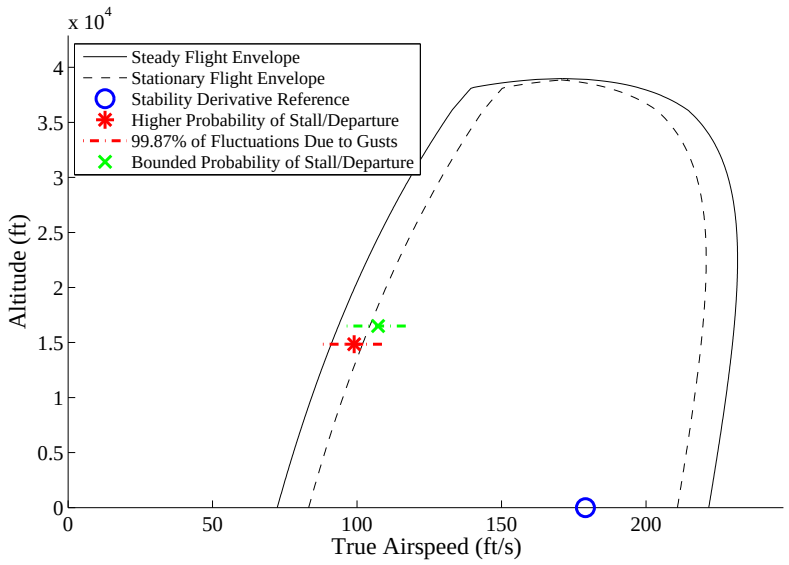

Figure 5.4: Steady and stationary flight envelopes for a Navion in moderate turbulence, along with two reference flight states, where the stationary flight envelope is shifted inward by $3\sigma_{v_t}$.

to draw the corresponding stationary flight envelope. Nevertheless, the stationary flight envelope boundaries do not approach an asymptote as the probability shrinks arbitrarily. Choosing a probability that is sufficiently small does eventually reduce the flight envelope dramatically. Also, note that the steady flight envelope is itself a stationary flight envelope with a 50% probability of instantaneously departing the steady flight envelope as the airspeed fluctuates and a logarithmic residence time of 0.

5.3.2 Steady Longitudinal Flight

The previous case of steady level longitudinal flight is a special case of the more general steady longitudinal flight, where the airplane flies along a straight line trajectory in a vertical plane and its linear and angular velocities remain constant in the body frame. The two-dimensional steady level longitudinal flight envelope is a cross-section of the three-dimensional steady longitudinal flight envelope where the

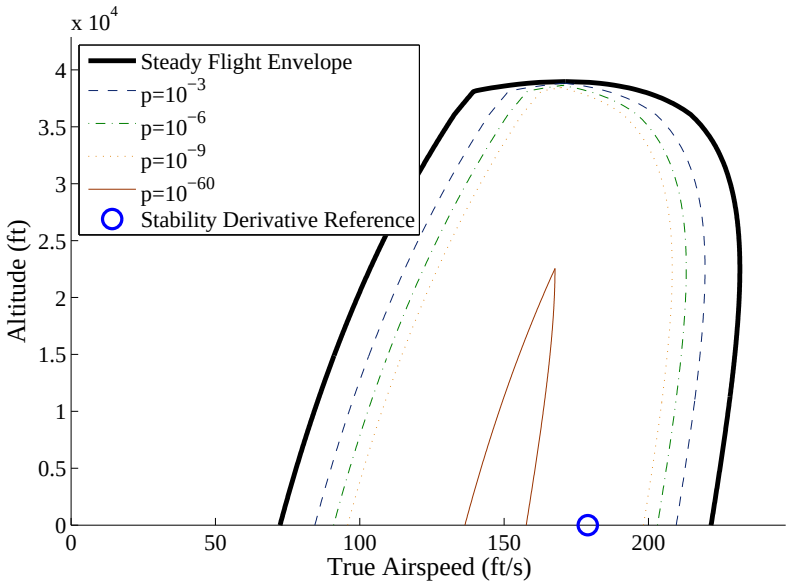

Figure 5.5: Steady flight envelope for a Navion and several stationary flight envelopes corresponding to different safety margins.

flight path angle $\gamma = 0$. Figure 5.6 shows the three-dimensional steady longitudinal flight envelope and its corresponding three-dimensional stationary longitudinal flight envelope for a Navion in moderate turbulence. The climb rate axis represents $V \sin(\gamma)$. $\sigma_{v_t}^2$ ranges from 13–16 ft^2/s^2 for the airplane and turbulence considered above. An inward shift of $15\sigma_{v_t}$ is used in Fig. 5.6 to make it easier to distinguish the two surfaces in the plot. The reader will quickly recognize that, in this example, the reduction of the flight envelope to form the stationary flight envelope is small, so for this airplane, our analysis is only important for flight states near the boundaries of the envelope. Later, Section 5.3.5 gives an example for a small, unmanned airplane where the adjustment is more significant.

5.3.3 Steady Turning Flight

To maintain steady longitudinal flight, the flight state must satisfy the stall constraint, which defines much of the low-speed portion of the flight envelope, and the propulsion constraint, which defines the rest. During steady turning flight, both

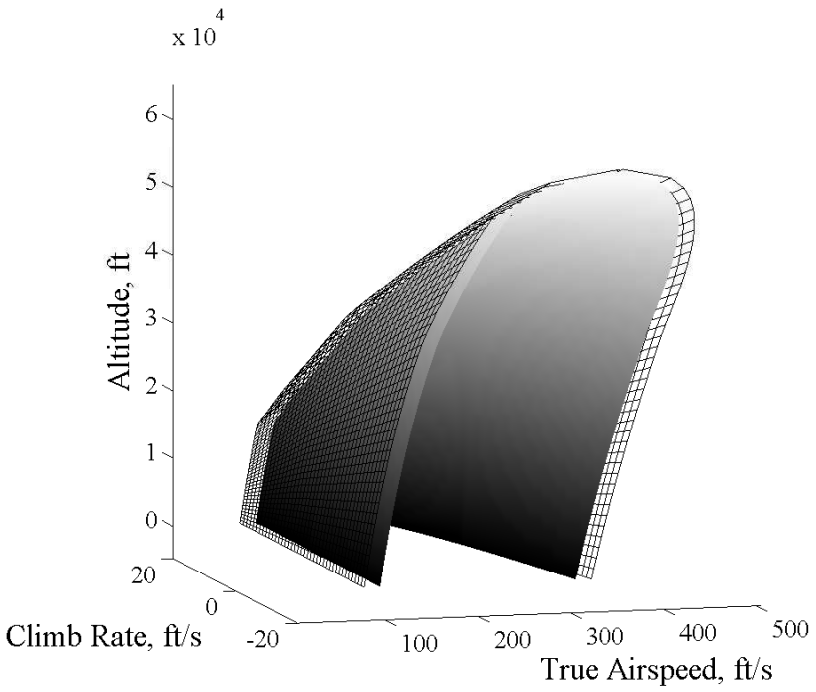

Figure 5.6: Three-dimensional steady longitudinal and stationary longitudinal flight envelopes for a Navion in moderate turbulence. The mesh surface is the steady longitudinal flight envelope and the solid surface underneath is the stationary flight envelope.

the stall constraint and the propulsion constraint still apply, but another constraint must be analyzed: wing loading. For steady flight analysis, the normal load factor $n \triangleq {}^{F_L}/_{mg}$ is usually constrained to be less than or equal to some maximum acceptable value $n_{\max}$. Exceeding the maximum load factor endangers the structural integrity of the airplane, thereby increasing the risk of costly damage to the airframe, loss of control, and a subsequent accident. When adjusting the steady turning flight envelope to take into account stochastic gusts, two different perturbations must be considered. The first perturbation is the one already discussed, the perturbation of v_t characterized by σ_{v_t}. The second perturbation is the perturbation of the normal load factor n.

5.3.3.1 Perturbation of Airspeed in Steady Turning Flight

As with the case of steady longitudinal flight, the linearized system developed in Chap. III, combined with the dependence of the reference flight state on the flight path angle and bank angle given in Eq. (5.1), provide sufficient tools to analyze the covariance of the velocity due to turbulence. The reference state depends on the flight path angle and bank angle, so the covariance matrix P varies with these angles. Figure 5.7a shows how $\sigma_{v_t}^2$ depends on the flight path angle for a reference condition with a 30° bank angle, a Mach number of 0.158, and an altitude of 11,550 ft. Figure 5.7b shows how $\sigma_{v_t}^2$ depends on the bank angle with a steady level turning reference state at a Mach number of 0.158 and an altitude of 11,550 ft.

5.3.3.2 Perturbation of Normal Load Factor in Steady Turning Flight

In addition to perturbations of the velocity, perturbations of the normal load factor also occur. For simplicity, static wing loading is assumed to dominate and structural dynamics are ignored. To assess the static wing loading, this section first considers the variance of the normal load factor perturbations, as was done with v_t.

In steady flight the relationship between F_L and mg allows the normal load factor to be expressed in terms of the bank angle around the velocity vector as $n = \sec \mu$. Turbulence will perturb the lift force as the true airspeed fluctuates, but the weight remains constant. This results in normal load factor perturbations. In a manner similar to Eq. (3.16), a first order perturbation to n called δn can be defined and related to the lift force perturbation as

$$\delta n = \frac{\delta F_L}{mg}. \tag{5.13}$$

The bottom right entry of the covariance matrix P is σ_n^2. Figure 5.8, a plot of the standard deviation of the normal load factor versus the reference normal load factor,

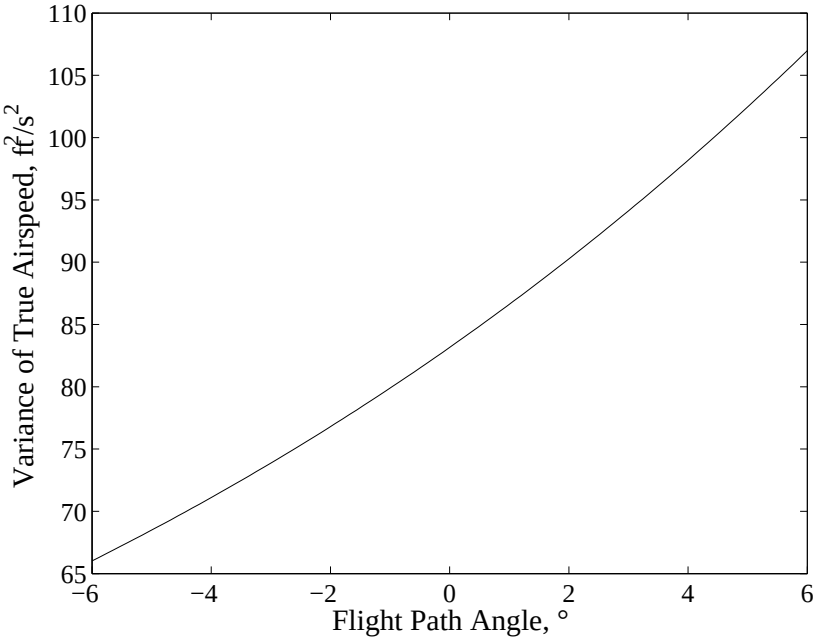

(a)

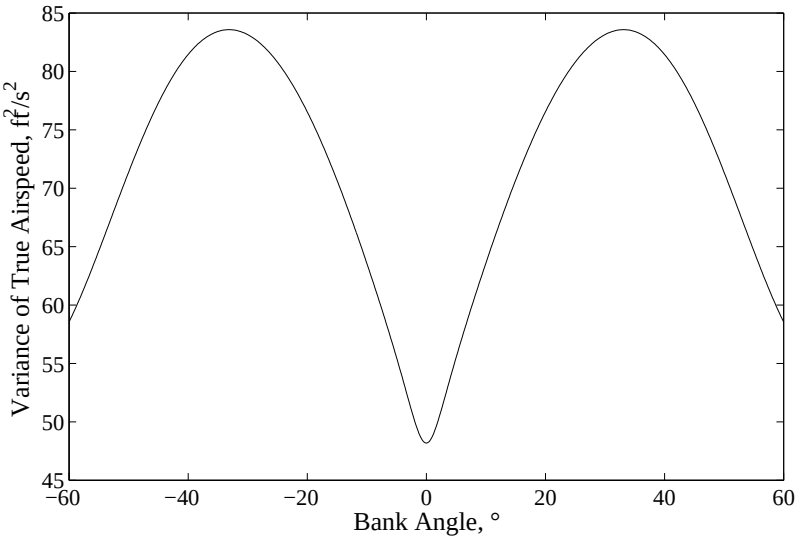

(b)

Figure 5.7: Relationship between the variance of the true airspeed and the flight path and bank angles for a Navion.

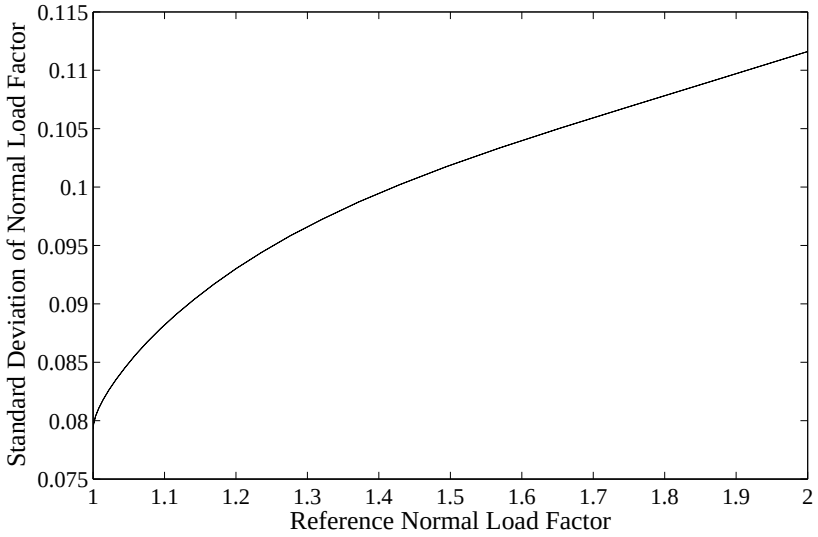

Figure 5.8: Plot of the standard deviation of the normal load factor versus the reference normal load factor for a Navion.

shows that as the reference normal load factor grows, the standard deviation of the normal load factor tends to an asymptote.

The variance of the normal load factor gives a measure of the typical size of the normal load factor perturbations as well as a way to predict how often large perturbations occur. For violations of the stall constraint, large but short duration fluctuations of the airspeed were assumed not to cause a stall even if they briefly violated the stall constraint. For wing loading, a large increase above the nominal normal load factor could damage the airplane in much less time than it takes to stall the airplane. Hence, practical applications would likely need more conservative safety margins on the wing loading compared to the safety margins on stall. Equation (5.4), the cumulative distribution of the Gaussian distribution, shows that this can be accomplished by requiring the airplane to stay more standard deviations away from the wing loading edge of the envelope than was chosen for the stall edge. Etkin notes that the Gaussian distribution can significantly underestimate the probability of gusts whose magnitude exceeds three standard deviations above the mean [17].

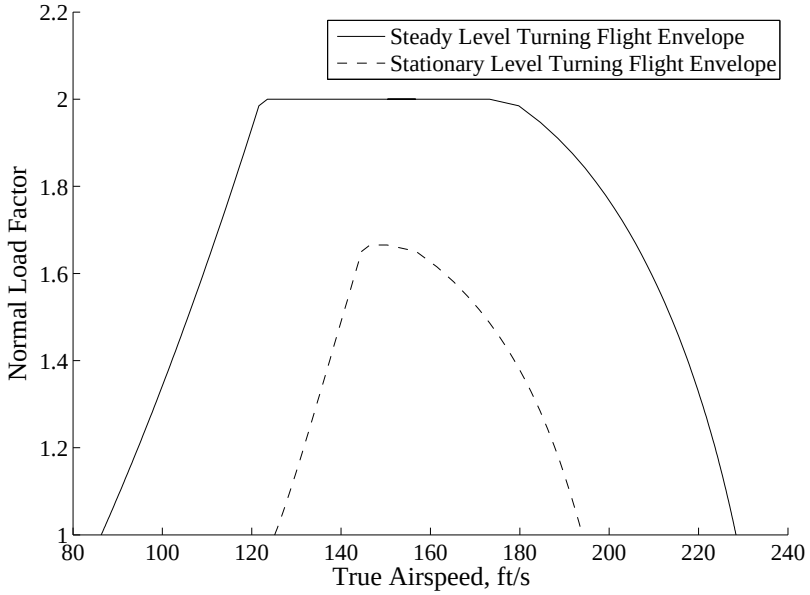

Figure 5.9: Steady and stationary v-n diagrams for a Navion.

This provides extra motivation for a large safety margin on the normal load factor when assuming a Gaussian distribution for the gusts.

For steady turning, the flight envelope is often assessed via a v-n diagram [33]. The steady longitudinal flight analysis above simply entailed shifting the edges of the flight envelope inward by an amount proportional to σ_{v_t}. Steady turning flight analysis requires shifting the envelope inward along both axes. Along the airspeed axis the shift is again proportional to σ_{v_t}. Along the normal load factor axis the shift is proportional to σ_n. In both cases, the size of the shift varies with the bank angle. Figure 5.9 shows an example of a v-n diagram for steady level turning at an altitude of 11,550 ft and the corresponding stationary flight envelope shifted inward by three standard deviations. $n_{\max}$ is chosen to be two [33].

The effect of the turbulence on loading is more significant than the effect on airspeed in this example. Compare the coefficients of variation for the normal load factor and the true airspeed, which, in the level turning example just given at a 40° bank angle, are 0.079 and 0.054, respectively. The coefficient of variation is the

ratio of the standard deviation to the mean, where in this case the mean is the reference value. The present analysis is likely less conservative than one that takes into account the airplane's structural dynamics or the distribution of the loading on the structure. These effects could make the wing loading during turbulence even larger. However, increasing the safety margin in this framework can protect against some of these unknown effects.

On a different note, the coefficient of variation serves as a heuristic to judge the viability of the linearization. A small coefficient of variation indicates that the first order effects of the perturbation are small, which suggests that including higher order effects will not change the results much.

5.3.4 Enlarging the Stationary Flight Envelope By Gust Alleviation

As illustrated in the examples above, the stationary flight envelope can be enlarged if the components of P are reduced. Section 3.6 showed that the components of P can be changed using feedback control, resulting in the closed-loop system given by Eq. (3.39). Feedback control has already been utilized to stabilize the airplane dynamics. In this section, the controller's ability to alleviate gusts is investigated.

A representative plot of how σ_{v_t} depends on the LQR gain Q is shown in Fig. 5.10. In the plot, Q is parameterized by its norm q from Eq. (5.9). The reference flight state was a steady level turn with a bank angle of 30° and Mach number of 0.158 at 11,550 ft.

Figure 5.11 shows a comparison of the steady flight envelope and two stationary flight envelopes for a steady level turn. One stationary flight envelope uses this controller implemented at $q = 10^3$ and the other at $q = 10$. $q = 10^3$ is not practical for the Navion, which is discussed later, but such a high value illustrates the potential enlargement of the stationary flight envelope by gust alleviation. The reference flight state used here is a steady level turn with a 30° bank angle at 11,550 ft.

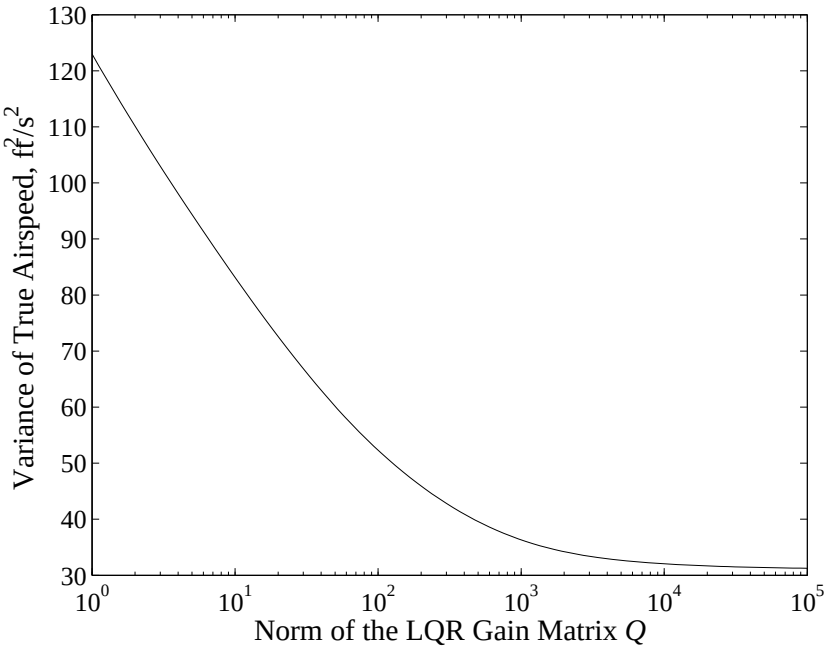

Figure 5.10: Plot of $\sigma^2_{v_t}$ versus the norm of the LQR gain Q for a Navion.

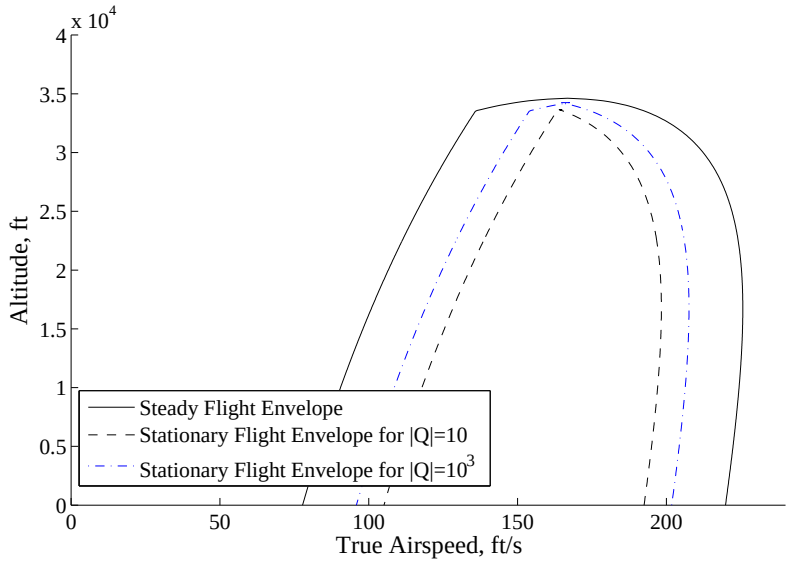

Figure 5.11: Comparison of the stationary level turning flight envelopes for two different norms of Q.

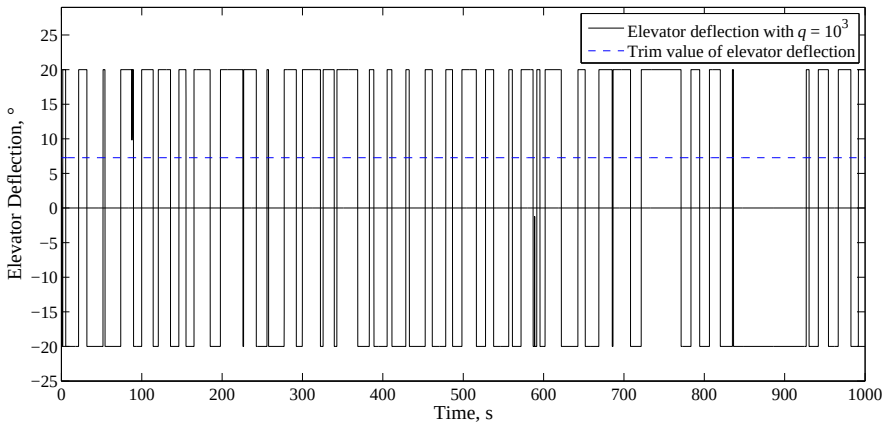

Figure 5.12: Elevator deflection versus time for a Navion with a high gain controller in turbulence.

The conclusion based on the two figures is that the stationary flight envelope can, in principle, be enlarged using feedback control. However, in order to achieve reductions in σ_{v_t} that are more than a few percent, the controller utilizes unreasonably high control gains. The resulting deflections of the control surfaces make unrealistic assumptions such as infinite bandwidth of the actuators, linear aerodynamics at large control deflections, and deflections well beyond typical saturation values.

As an example, a sample time history of the elevator deflection with $q = 10^3$ is plotted in Fig. 5.12. The figure also shows the trim value of the elevator deflection for the steady reference condition. In the example, the elevator deflection is subject to a $\pm 20^\circ$ saturation that is not accounted for by the controller. From the figure, it is clear that with q set at 10^3, the controller almost always generates control inputs in excess of the elevator's capabilities. The aileron and rudder deflections suffer from the same problem. Even at $q = 10$, saturation at $\pm 20^\circ$ limits performance, but to less of an extent. We did not investigate loading on or near the control surfaces for this high-gain controller, but presume they were correspondingly large. Controller designs and control surfaces other than those used, such as those incorporating quasilinear control [74] or those described in Chap. II, might offer more realistic alleviation.

The modest alleviation achieved in this example conveys the importance of the stationary flight envelope. Should closed-loop control offer dramatic reduction in the effects of the gusts, then the stationary flight envelope would be enlarged to the point that it offers little advantage over the steady flight envelope. However, this study suggests that simple state feedback with a Kalman filter is not sufficient to reduce the effects of gusts for this aircraft. Therefore, short of a controller design with much better performance, the stationary flight envelope remains a useful tool to determine how far from the steady flight envelope boundaries a pilot should fly to maintain a desired safety margin.

5.3.5 Comparison With Other Examples

This section provides two other numerical examples for comparison with the detailed Navion results just presented. First, the stationary flight envelope is shown for a smaller airplane, an Aerosonde. Second, the Navion's stationary flight envelope is computed using a von Kármán wind model instead of the Dryden wind model.

5.3.5.1 Aerosonde Stationary Flight Envelope

Some of the Navion stationary flight envelope examples presented show only minor reductions in the flight envelope after accounting for turbulence, indicating that only states very close to the edges of the envelope are problematic during turbulence encounters. In Chap. IV, the coefficient of variation for the airspeed, the ratio of the airspeed's standard deviation to its mean, decreases monotonically with increasing airplane size. Thus, for airplanes smaller than the Navion, the flight envelope reductions will be larger.

As an example of a smaller airplane, consider the Aerosonde model in Beard and McLain [12]. An Aerosonde is a single-engine, propeller-driven, unmanned aircraft with a wingspan of 9.56 ft and a typical weight of 29.7 lbs. Figure 5.13 depicts the

steady and stationary flight envelopes for the Aerosonde subject to the same moderate turbulence as the Navion in Fig. 5.4 and using a reference condition of steady level longitudinal flight at 4,950 ft and 83 ft/s. Comparing the Aerosonde's steady flight envelope to the Navion's, the Aerosonde is seen to be slower than the Navion, to have a lower flight ceiling, and to have a smaller range of airspeeds. Moreover, the reduction from the Aerosonde's steady flight envelope to the Aerosonde's stationary flight envelope is more substantial. This gives a true airspeed coefficient of variation of 5.8%, compared to a coefficient of variation of 3.8% in the Navion steady level longitudinal example. Using the same safety margin of a three standard deviation inward shift of the flight envelope, at 4,950 ft the Aerosonde's range of airspeeds within the envelope is decreased by about 35% to form the stationary flight envelope, compared to about a 15% reduction in the Navion example. This means that turbulence constrains the Aerosonde to fly closer to the center of its steady flight envelope than it does for the Navion in order to stay within the safety margin.

While this result and the scaling laws suggest that the reduction of small scale airplanes' flight envelopes are more substantial in turbulence, many small scale airplanes have high thrust to weight ratios. This allows them to fly post-stall, offsetting the reduction in lift with a component of thrust. For application to small scale airplanes, the results of this dissertation would be complemented by research on the expansion of the flight envelope post-stall for high performance airplanes.

5.3.5.2 Response to von Kármán Gusts

Thus far, all of the examples given in this dissertation use turbulence generated using the Dryden model of stochastic gusts. In this section, the level longitudinal flight example from Section 5.3.1 and Fig. 5.14 is repeated using the von Kármán model of stochastic gusts. The von Kármán coloring filters, adapted from the MATLAB documentation [75], approximate the von Kármán gust model since the model's power

spectral density is irrational. The reference state is again steady level longitudinal flight in moderate turbulence with an airspeed of 102 ft/s at an altitude of 16,500 ft. The variance of the true airspeed $\sigma_{v_t}^2$ is 13 ft^2/s^2. Figure 5.14 shows the steady and stationary flight envelopes for this von Kármán example. This example demonstrates the viability of using the approximated von Kármán gust model's coloring filters in all of the scaling and envelope examples of this dissertation. In applications, the most appropriate gust model can be applied.

5.4 Summary

This chapter uses linearized airplane dynamic equations to determine the impact of stochastic gusts on steady flight maneuvers. In the process, it extended the concept of steady flight to stationary flight, where the airplane's linear and angular velocities are stationary random processes whose mean corresponds to a reference steady flight state. Stationary flight, while developed in the context of response to turbulence, is relevant in any situation where the airplane's state variables are stationary random processes. The stationary flight envelope, an adjusted steady flight envelope that takes into account the stochastic nature of the state variables, is computed based on the statistics of the state variables. Whether those statistics are computed from a model of how an underlying cause affects the state variables or those statistics are estimated from direct measurements, the stationary flight envelope can be employed to ensure that a desired safety margin is maintained.

This analysis' model of airplane dynamic response to stochastic gusts allows estimation of the statistics of the state variables and, therefore, estimation of the probability of violating the steady flight constraints. The analysis also shows that this probability can be reduced with feedback control to alleviate gust loads. This information can ultimately be used, given wind gust statistics, to choose flight states that guarantee, with specified probability and logarithmic residence time, that the aircraft

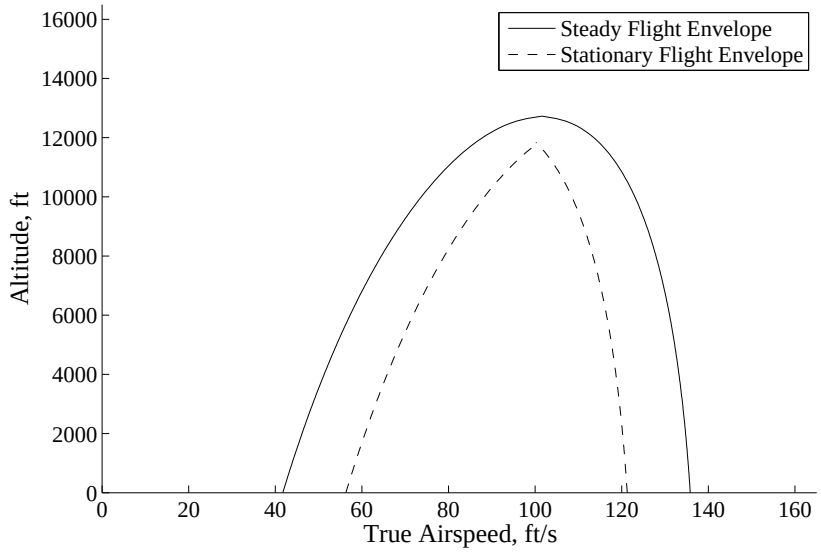

Figure 5.13: Steady and stationary flight envelopes for an Aerosonde in steady level longitudinal flight.

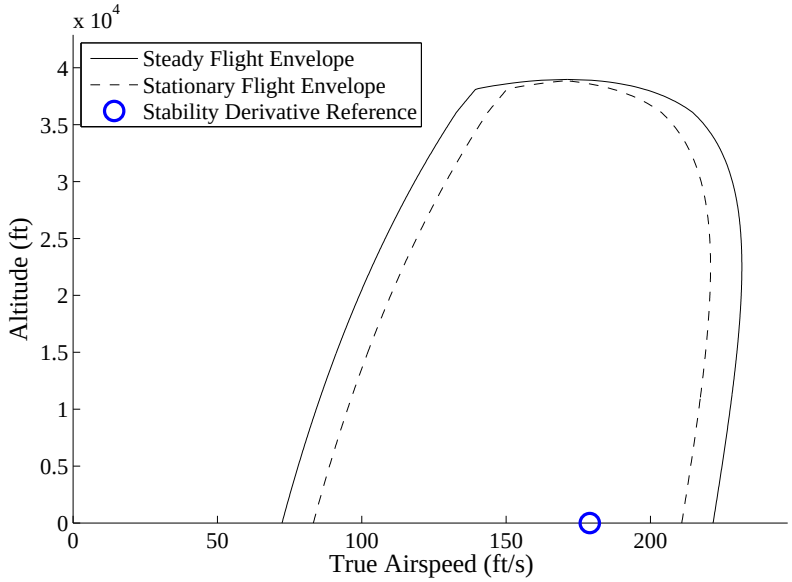

Figure 5.14: Steady and stationary flight envelopes for a Navion in moderate turbulence using the von Kármán gust model.

remains within the steady flight envelope despite uncertain conditions. In particular, the method presented shifts the boundary of the steady flight envelope based on the statistics of the wind gusts to provide a probabilistic safety margin when flying through turbulence. The stationary flight envelope can help pilots plan safe flights through known turbulent conditions. The stationary flight envelope, stored as a look-up table or computed online, can help autopilots, as well. Similarly, if airplanes encounter turbulent conditions in-flight and can estimate the statistics of either the turbulence or the flight state, the stationary flight envelope can give pilots a basis to determine quantitatively which maneuvers are safe.

CHAPTER VI

Conclusion

6.1 Summary of Contributions

The preceding chapters addressed the problem of quantifying airplane performance in stochastic gusts. Following a review of the literature in Chap. II, Chap. III reviewed the linearized, open- and closed-loop airplane equations of motion with stochastic gusts as a disturbance. Chapter III also reviewed how to compute the covariance matrix for the aircraft and wind linear velocity components.

Chapter IV derived the dependence of the airspeed variance on airplane size using a phugoid approximation of the linearized dynamics. It also gave a series of numerical examples showing how airplane performance in turbulence scales with size. In particular, Chap. IV compared the NASA GTM with its dynamically scaled counterpart the NASA T2, showing that the scaling laws derived can be used to accurately predict the T2's performance based on the performance of the GTM. Key contributions on scaling in Chap. IV included:

- Scaling laws for the airplane phugoid mode natural frequency and damping ratio
- Analytical expressions for the airplane airspeed and flight path angle variances in the phugoid approximation parameterized by a new non-dimensional parameter, the phugoid-to-turbulence relative frequency

- Scaling laws for the airplane airspeed and flight path angle variances in the phugoid approximation

- A scaling law for the airplane airspeed coefficient of variation in the phugoid approximation showing decreasing coefficient of variation with increasing airplane size

- Validation of these scaling laws through numerical examples comparing the performance of eleven aircraft, focusing on the NASA GTM and its dynamically scaled counterpart, the NASA T2

Chapter V continued by showing how the true airspeed and normal load factor variances can be used to compute safety margins for flight through stochastic gusts. In developing these safety margins, the chapter introduced the notions of stationary flight and the stationary flight envelope. To illustrate the concepts, the chapter provided numerical examples of a Navion performing a variety of steady flight maneuvers with accompanying stationary flight envelopes. Complementing the general aviation aircraft examples, the chapter ended with an example of a stationary flight envelope for the much smaller Aerosonde, showing even more substantial reductions in the flight envelope because of turbulence. Key contributions in Chap. V on safety margins for flight through turbulence included:

- A method to determine the probability that a steady flight maneuver violates a steady flight constraint after taking into account stochastic gusts

- The stationary flight envelope, an innovative visualization tool to depict which steady flight states have high probability of exceeding a steady flight constraint in the presence of stochastic gusts

These contributions further our understanding of the effects of stochastic gusts on airplane performance. In particular, they help us understand the capabilities

and limitations of small scale airplanes, which this dissertation showed are more susceptible to turbulence. As use of small, unmanned airplanes continues to grow for military and commercial applications, these contributions can lead to improved airplane design and control for flight through gusts.

6.2 Future Directions

Future research can readily build upon the contributions of this dissertation. Some of these future projects are direct extensions of these contributions, including some extensions already mentioned in the preceding chapters. Direct extensions of the scaling work in Chap. IV include:

- Validating the scaling laws from the phugoid approximation against the rigid body, six-degree-of-freedom model
- Developing scaling laws for the true airspeed rather than the magnitude of the center of mass velocity
- Defining a lower bound on airplane size where the scaling laws no longer apply
- Incorporating unsteady effects into the gust response solutions
- Developing scaling laws for gust alleviation to complement the scaling laws for gust response

Similarly, direct extensions of the work in Chap. V on stationary flight and stationary flight envelopes include:

- Identifying maneuvers where angle of attack variations due to turbulence are more important than airspeed variations when computing the stall boundary of the stationary flight envelope

- Detailed comparison of the residence time derived from large deviations theory and the residence time derived from the frequency of exceedance
- Incorporating the effects of structural modes into the wing loading safety margins
- Assessing the potential gains of quasilinear control to alleviate gusts despite actuator saturation

In addition to the direct extensions just listed, farther-reaching extensions of this work include:

- Using the same analytical technique to develop safety margins for other types of wind disturbances, such as discrete gusts, wind shear, and wake turbulence
- Extending the scaling laws of this dissertation to low Reynolds number flyers
- Developing margins analogous to those used in the steady flight envelope that quantify deviation from a desired trajectory in turbulence
- Using the safety margins developed in this dissertation to quantify turbulence limits for takeoff and landing of particular airplane models
- Informing pilots and operators of the probability of exceeding the steady flight envelope in turbulence via charts in pilot operating handbooks or via in-cockpit displays
- Incorporating post-stall dynamics into small scale airplane controller design so unmanned aircraft can use less stringent safety margins on the stall boundary of the stationary flight envelope
- Developing a model linking uncertainty in airplane dynamics with degradation of information collection from onboard sensors in order to quantify the effects

of turbulence on information gathered during intelligence, surveillance, and reconnaissance flights

6.3 Closing Remarks

At the beginning of this dissertation, we considered the hazard posed by turbulence to flight operations, recognized that small aircraft seem to be more susceptible to that hazard, and noted the growing use of small scale, unmanned aircraft in military and potential commercial applications. The subsequent chapters quantified the hazard posed by turbulence and the extent to which small scale aircraft are more susceptible. They also presented safety margins that, when adhered to, guarantee with specified probability and logarithmic residence time that an airplane flight state will remain in the steady flight envelope despite the airplane operating in turbulence.

Aircraft will continue to encounter turbulence. Using the contributions of this dissertation, those who design aircraft, design autopilots for aircraft, and operate aircraft, especially small scale aircraft, can better understand the capabilities and limitations of their aircraft in turbulence. They can also use these contributions to plan safer flights through known turbulent conditions and to pilot their aircraft in a manner more robust with respect to the effects of turbulence in flight.

APPENDICES

APPENDIX A

Perturbations of v_t, α, & n

This appendix shows how to derive the output matrix C_{POL} used in Eq. (3.36). Multiplying the state vector of Eq. (3.33) by C_{POL} gives as output the perturbations of the true airspeed, the angle of attack, and the normal load factor, $(\delta v_t \quad \delta\alpha \quad \delta n)^{\text{T}}$. Therefore, this appendix defines these quantities and shows how to write them as linear combinations of the airplane and wind linear velocities.

True Airspeed Perturbations

We define the true airspeed as the magnitude of the airplane velocity with respect to the air, namely

$$v_t \triangleq |v_c - v_w| = \sqrt{(u - v_{wx})^2 + (v - v_{wy})^2 + (w - v_{wz})^2}. \tag{A.1}$$

We perturb the airplane and wind velocities as in Chap. III by substituting $v_c \leftarrow v_c + \delta v_c$ and $v_w \leftarrow v_w + \delta v_w$, where v_c and v_w are constant reference values. Solving

for the first order perturbation of v_t,

$$\delta v_t = \frac{\delta v_t^2}{2v_t}, \tag{A.2}$$

$$\delta v_t^2 = 2\left((u - v_{wx})(\delta u - \delta v_{wx}) + (v - v_{wy})(\delta v - \delta v_{wy}) + (w - v_{wz})(\delta w - \delta v_{wz})\right), \tag{A.3}$$

where δv_t^2 is the perturbation of v_t^2, not the square of δv_t, and v_t now refers to a constant true airspeed reference value. This first order perturbation is a linear combination of the airplane and wind linear velocity components and can be factored as

$$\delta v_t^2 = 2\begin{pmatrix} u - v_{wx} & v - v_{wy} & w - v_{wz} \end{pmatrix}\begin{pmatrix} \delta u - \delta v_{wx} & \delta v - \delta v_{wy} & \delta w - \delta v_{wz} \end{pmatrix}^{\mathrm{T}}. \tag{A.4}$$

The column vector on the right is itself a linear combination of airplane and wind linear velocity components' perturbations and, therefore, of the state vector of Eq. (3.33) as well. Thus,

$$\delta v_t^2 = 2\begin{pmatrix} u - v_{wx} & v - v_{wy} & w - v_{wz} \end{pmatrix} C_t x, \tag{A.5}$$

$$C_t \triangleq \begin{pmatrix} \mathbb{1}_3 & 0 & 0 & -C_{wv} \end{pmatrix}, \tag{A.6}$$

$$x = \begin{pmatrix} \delta v_c & \delta\omega & \delta\epsilon & \xi_w \end{pmatrix}^{\mathrm{T}}, \tag{A.7}$$

where C_{wv} is defined in Eq. (3.31b) and x is the state vector of Eq. (3.33). Substituting Eq. (A.5) into Eq. (A.2) gives the first row of C_{POL}.

Angle of Attack & Normal Load Factor Perturbations

This section shows how to derive the perturbations of the angle of attack and normal load factor as a linear combination of the state vector of Eq. (3.33). To begin,

define the normal load factor and perturb it with substitutions analogous to those in Chap. III:

$$n = \frac{F_L}{mg} \leftarrow n + \delta n = \frac{F_L + \delta F_L}{mg}. \tag{A.8}$$

Canceling the steady state terms,

$$\delta n = \frac{\delta F_L}{mg}, \tag{A.9}$$

relating the perturbation of the normal load factor to the perturbation of the lift force.

Recall the magnitude of the lift force,

$$F_L = \frac{1}{2}\rho S C_L v_t^2, \tag{A.10}$$

$$C_L = C_{L_0} + C_{L_\alpha}\alpha. \tag{A.11}$$

Perturbing this expression for the lift to first order,

$$\delta F_L = \frac{1}{2}\rho S C_L \delta v_t^2 + \frac{1}{2}\rho S C_{L_\alpha} v_t^2 \delta\alpha, \tag{A.12}$$

where δv_t^2 is defined in Eq. (A.3) as the perturbation of v_t^2. All of the quantities except δv_t^2 and $\delta\alpha$ now represent constant reference values. Air density variations due to turbulence are assumed negligible.

Equation (A.12) relates the lift force perturbation to the true airspeed and angle of attack perturbations. Equation (A.5) gives δv_t^2. The angle of attack is defined in terms of the relative wind as

$$\alpha = \arctan\frac{w - v_{wz}}{u - v_{wx}}. \tag{A.13}$$

Perturbing this to first order,

$$\delta\alpha = \frac{u - v_{wx}}{(u - v_{wx})^2 + (w - v_{wz})^2}(\delta w - \delta v_{wz}) - \frac{w - v_{wz}}{(u - v_{wx})^2 + (w - v_{wz})^2}(\delta u - \delta v_{wx}). \tag{A.14}$$

The remainder of this derivation can be completed using this expression for $\delta\alpha$. However, most flight dynamics applications assume a small angle of attack, i.e. $(u - v_{wx})^2 \gg (w - v_{wz})^2$. Under this assumption, Eq. (A.14) simplifies to

$$\delta\alpha \approx \frac{1}{u - v_{wx}}(\delta w - \delta v_{wz}) - \frac{w - v_{wz}}{(u - v_{wx})^2}(\delta u - \delta v_{wx}). \tag{A.15}$$

As with Eq. (A.3), this simplified expression for $\delta\alpha$ can be factored into a row vector multiplying the state vector of Eq. (3.33),

$$\delta\alpha \approx \begin{pmatrix} -\frac{w - v_{wz}}{(u - v_{wx})^2} & 0 & \frac{1}{u - v_{wx}} \end{pmatrix} C_t x, \tag{A.16}$$

which is the second row of C_{POL}. Making the necessary substitutions into Eq. (A.9) gives the last row of C_{POL}. Factoring the expressions for the rows,

$$C_{\text{POL}} \triangleq \begin{pmatrix} \frac{1}{v_t} & 0 & 0 \\ 0 & 1 & 0 \\ 0 & 0 & \frac{\rho S C_L}{mg} \end{pmatrix} \begin{pmatrix} u - v_{wx} & v - v_{wy} & w - v_{wz} \\ -\frac{w - v_{wz}}{(u - v_{wx})^2} & 0 & \frac{1}{u - v_{wx}} \\ u - v_{wx} - \frac{C_{L_\alpha} v_t^2}{2C_L}\frac{w - v_{wz}}{(u - v_{wx})^2} & v - v_{wy} & w - v_{wz} + \frac{C_{L_\alpha} v_t^2}{2C_L(u - v_{wx})} \end{pmatrix} C_t. \tag{A.17}$$

APPENDIX B

Flight Envelope Residence Times

This appendix derives the flight envelope residence time and the probability of exceeding the flight envelope per unit time.

Asymptotic Output Residence Time

In this section, work done by Meerkov and Runolfsson on aiming control [72, 73] is leveraged to compute the expected time for an airplane's flight state to first exceed the steady flight envelope. First, we review definitions and a theorem taken directly from Meerkov and Runolfsson [73], then we derive a special case applicable to the safety margins of Chap. V.

Consider a LTI system such as Eq. (3.33) that can be modeled in state space form,

$$\dot{x} = Ax + \varepsilon Ed, \tag{B.1a}$$

$$y = Cx, \tag{B.1b}$$

where $x \in \mathbb{R}^n$, $y \in \mathbb{R}^p$, d is a zero-mean, stationary, Gaussian white noise process with covariance matrix D, ε is a small parameter, and C has rank p. Define a domain

$\Psi \subset \mathbb{R}^p$ that contains the origin and has a smooth boundary $\partial\Psi$. Assume that $x_0 = x(0) \in \Omega_0 \triangleq \{x \in \mathbb{R}^n | y = Cx \in \Psi\}$. Denote the output $y(t)$ in Eq. (B.1) with initial condition x_0 as $y(t, x_0)$. Define the first passage time of the output $y(t, x_0)$ from Ψ as

$$\tau^\varepsilon(x_0) = \inf\{t \geq 0 : y(t, x_0) \in \partial\Psi | y(t_0, x_0) \in \Psi\}, \tag{B.2}$$

and call its mean,

$$\bar{\tau}^\varepsilon(x_0) = \mathrm{E}[\tau^\varepsilon(x_0)|x_0], \tag{B.3}$$

the *residence time*. Large deviations theory offers asymptotic approximations of these times for small ε.

Theorem 1. *Assume*

1. *A is Hurwitz*

2. *The pair (A, E) is completely controllable*

Then uniformly for all x_0 belonging to compact subsets of $\Omega = \{x_0 \in \mathbb{R}^n | Ce^{At}x_0 \in \Psi, t \geq 0\}$ we have

$$\lim_{\varepsilon \to 0} \varepsilon^2 \ln \bar{\tau}^\varepsilon(x_0) = \hat{\mu}(\Psi), \tag{B.4}$$

where

$$\hat{\mu}(\Psi) = \min_{y \in \partial\Psi} \frac{1}{2} y^{\mathrm{T}} P^{-1} y, \tag{B.5}$$

$$P = C\bar{P}C^{\mathrm{T}}, \tag{B.6}$$

and $\bar{P}$ is the positive definite solution of the Lyapunov equation

$$A\bar{P} + \bar{P}A^{\mathrm{T}} + EDE^{\mathrm{T}} = 0. \tag{B.7}$$

This theorem is proven by Meerkov and Runolfsson [73]. The constant $\hat{\mu}$ is referred

to as the *logarithmic residence time* in Ψ.

Consider the special case where y is some scalar quantity denoted $\delta\tilde{y}$. The covariance matrix P simplifies to the variance of $\delta\tilde{y}$, denoted $\sigma_{\tilde{y}}^2$, the domain Ψ simplifies to the real interval $[-\delta\tilde{y}_{\min}, \delta\tilde{y}_{\max}]$, where $\delta\tilde{y}_{\min}, \delta\tilde{y}_{\max} > 0$, the boundary $\partial\Psi$ simplifies to the two real numbers $\{-\delta\tilde{y}_{\min}, \delta\tilde{y}_{\max}\}$, and the logarithmic residence time simplifies to

$$\hat{\mu}(\Psi) = \frac{\min(\delta\tilde{y}_{\min}, \delta\tilde{y}_{\max})^2}{2\sigma_{\tilde{y}}^2}. \tag{B.8}$$

We can express the boundary $\partial\Psi$ in terms of standard deviations of $\delta\tilde{y}$: $\delta\tilde{y}_{\min} = k_{\min}\sigma_{\tilde{y}}$ and $\delta\tilde{y}_{\max} = k_{\max}\sigma_{\tilde{y}}$. Substituting into Eq. (B.8),

$$\hat{\mu}(\Psi) = \frac{1}{2}\min(k_{\min}, k_{\max})^2. \tag{B.9}$$

Because $y(t)$ has zero mean in Eq. (B.1), the logarithmic residence time for scalar output is proportional to the square of the number of standard deviations between the mean and the boundary closest to the mean. The residence time can be approximated as

$$\bar{\tau}^{\varepsilon} \approx e^{\hat{\mu}/\varepsilon^2}. \tag{B.10}$$

For a more accurate but still approximate value of $\bar{\tau}^{\varepsilon}$, the exponential can be multiplied by a proportionality constant described in detail by Meerkov and Runolfsson [72]. A related formulation for the residence time that gives the same logarithmic residence time is derived in the next section.

Suppose that $\delta\tilde{y}$ represents zero mean, stationary, Gaussian fluctuations of some flight dynamics quantity around its steady flight reference value $\tilde{y}$. Furthermore, suppose that in steady flight there is a constraint $\tilde{y}_{\min} \leq \tilde{y} \leq \tilde{y}_{\max}$. We can then define $\delta\tilde{y}_{\min} = \tilde{y} - \tilde{y}_{\min}$ and $\delta\tilde{y}_{\max} = \tilde{y}_{\max} - \tilde{y}$. With this choice of boundary, the residence time $\bar{\tau}^{\varepsilon}$ and the logarithmic residence time $\hat{\mu}$ quantify the expected time for the perturbed airplane flight state to exit the steady flight envelope.

Probability of Exceedance Per Unit Time

In many applications, it is desirable to evaluate the probability of a random event occurring during a specified time interval. Chapter 4 of Hoblit describes how to do this for perturbed variables in the case of airplane dynamics driven by stationary, Gaussian models of turbulence [15]. His method, summarized here, amounts to determining the frequency with which a Gaussian random process exceeds some threshold, using that frequency as the rate for a Poisson process that counts the number of threshold crossings of the Gaussian random process, and computing the probability that the first jump of the Poisson process occurs at time t.

Rice [76] shows that for a zero-mean, scalar, Gaussian random process $\delta\tilde{y}$ with variance $\sigma^2_{\tilde{y}}$, power spectral density $\Phi_{\tilde{y}}(f)$, and some threshold $\delta\tilde{y}_{\max} > 0$, the frequency of exceedence, i.e., the number per unit time of threshold upcrossings, crossings with positive slope, is

$$N(\delta\tilde{y}_{\max}) = N_0 e^{-\frac{\delta\tilde{y}^2_{\max}}{2\sigma^2_{\tilde{y}}}}, \tag{B.11}$$

where N_0 is the number of zero upcrossings per unit time and can be computed from the power spectral density of the random process,

$$N_0 = \sqrt{\frac{\int_0^\infty f^2 \Phi_{\tilde{y}}(f) df}{\int_0^\infty \Phi(f)_{\tilde{y}} df}}. \tag{B.12}$$

The integral in the numerator of N_0 is problematic because it does not converge for either the Dryden or von Kármán models or, consequently, for many flight performance metrics. This makes it difficult or impossible to compute accurate values for N_0 in many cases. Both Hoblit [15] and Rice [76] address cases where the integral in the numerator of N_0 does not converge. Because of the symmetry of the Gaussian distribution, the frequency of crossing $-\delta\tilde{y}_{\min} < 0$ with negative slope is the same after substituting $\delta\tilde{y}_{\min}$ for $\delta\tilde{y}_{\max}$. Expressing the threshold in terms of standard

deviations, $\delta\tilde{y}_{\max} = k_{\max}\sigma_{\tilde{y}}$,

$$N(k_{\max}) = N_0 e^{-\frac{k_{\max}^2}{2}}. \tag{B.13}$$

According to Hoblit, for $k_{\max} > 2$, this frequency of exceedance is a good approximation for the average number of peaks that exceed $\delta\tilde{y}_{\max}$ per unit time on sample paths of $\delta\tilde{y}$.

For many types of stochastic processes, including Gaussian processes, as the threshold whose upcrossings are being counted grows arbitrarily, the number of the upcrossings converges to a Poisson process. The Poisson process' inter-arrival times are exponentially distributed random variables with rate equal to $N(\delta\tilde{y}_{\max})$ [77]. The probability that at time t no upcrossing has occurred is $e^{-N(\delta\tilde{y}_{\max})t}$ [78]. Its complement is the *probability of exceedance* at time t, the probability that at least one upcrossing has occurred by time t,

$$p_{\text{ex}}(t) = 1 - e^{-N(\delta\tilde{y}_{\max})t}. \tag{B.14}$$

For small $N(\delta\tilde{y}_{\max})t$, as in the case of large deviations of $\delta\tilde{y}$ from the mean,

$$p_{\text{ex}}(t) \approx N(\delta\tilde{y}_{\max})t, \tag{B.15}$$

and $N(\delta\tilde{y}_{\max})$ is approximately equal to the *probability of exceedance per unit time*, ${}^{p_{\text{ex}}(t)}/_{t}$.

The expected time for the first jump of a Poisson process is the mean of the inter-arrival times' exponential distribution, $N^{-1}(\delta\tilde{y}_{\max})$. This quantity is another way to formulate the residence time of $\delta\tilde{y}$ within the threshold $\delta\tilde{y}_{\max}$. Detailed comparison with the residence time of the previous section is left as future work, but we note here that both formulations give the same logarithmic residence time for scalar outputs of

Eq. (B.1), $\hat{\mu} = \ln(N_0/N(\delta\tilde{y}_{\max}))$.

Once again, we can consider $\delta\tilde{y}$ to be fluctuations around some steady flight reference value $\tilde{y}$ and set $\delta\tilde{y}_{\min}$ or $\delta\tilde{y}_{\max}$ according to the difference between $\tilde{y}$ and the steady flight constraints on $\tilde{y}$. The upcrossings then represent departures from the flight envelope. As in the residence time discussion of the previous section, $\min(\delta\tilde{y}_{\min}, \delta\tilde{y}_{\max})$ will determine the margin of safety since the smaller threshold has a larger frequency of exceedance, a larger probability of exceedance per unit time, and a shorter residence time.

APPENDIX C

Numerical Example Parameters

The numerical examples in Chaps. IV–V use models of eleven different aircraft. They also incorporate a Dryden model of wind gusts and an atmospheric model. This appendix provides references for and descriptions of the different airplane and wind models used. First the NASA GTM and T2 are described, followed by the Navion, then the remaining aicraft, and finally the wind and atmospheric models.

NASA GTM & T2

Chapter IV's examples focus on the NASA GTM and T2 transport aircraft. The GTM parameters came primarily from a GTM simulator developed at NASA Ames. The model is described in an internal NASA report [14] and applied in Nguyen et al. [79]. The simulator contains tables of stability derivatives parameterized by Mach number and angle of attack. Nguyen et al. [79, 80] use the GTM to study damaged, asymmetric transport aircraft, but Chap. IV uses the parameters for the intact GTM. The parameters selected correspond to Mach 0.8 with an angle of attack of 2°. The simulator does not specify an altitude for the parameters, so they are assumed to be valid at 35,000 ft. The GTM is similar to the Boeing 757, so this Mach number

and altitude are chosen based on Boeing 757 specifications posted on the American Airlines website[1], and the angle of attack is chosen based on a Boeing article about commercial jet angles of attack [81].

Stability derivatives for the NASA T2 subscale transport are given in the appendix of Morelli and Cunningham [13]. According to the flight test results, the stability derivatives correspond to a nominal flight condition of level longitudinal flight with a airspeed of roughly 132 ft/s at 1,400 ft with an angle of attack of 4.5°. Morelli and Cunningham [13] do not give values for the reference coefficients of lift or drag, C_{L_0} and C_{D_0}. These coefficients are estimated using standard equations for steady level longitudinal flight performance given in McClamroch [33]. Specifically, the following two expressions for the coefficient of lift are equated and solved for C_{L_0}:

$$C_L = \frac{2mg}{\rho S V^2}, \tag{C.1}$$

$$C_L = C_{L_0} + C_{L_\alpha}\alpha. \tag{C.2}$$

For the reference drag coefficient, the GTM's airspeed for minimum thrust at 1,400 ft computed in Eq. (4.25) is scaled using Eq. (4.1e) to the corresponding T2 airspeed for minimum thrust v_{mt}. Carrying out the computation, $v_{mt} = 104$ ft/s for the T2 at 1,400 ft altitude. This airspeed is related to the reference drag coefficient as

$$v_{mt} = \sqrt{\frac{2mg}{\rho\sqrt{C_{D_0}\pi e S b^2}}}. \tag{C.3}$$

These relationships lead to the values

$$C_{L_0} = 0.129, \qquad C_{D_0} = 0.0252. \tag{C.4}$$

[1]American Airlines, "Boeing 757," `http://www.aa.com/il8n/aboutUs/ourPlanes/boeing757.jps`, accessed February 28, 2013.

Table C.1: Navion parameters and stability derivatives used in this dissertation. Values are given in the source's units.

Symbol	Value	Name	Ref.	Symbol	Value	Ref.
mg	2,750 lbs	Weight	[82]	C_{m_q}	-9.96	[82]
I_{xx}	1,048 slug ft^2	Rolling Moment of Inertia	[82]	C_{y_β}	-0.564	[82]
I_{yy}	3,000 slug ft^2	Pitching Moment of Inertia	[82]	C_{l_β}	-0.074	[82]
I_{zz}	3,530 slug ft^2	Yawing Moment of Inertia	[82]	C_{n_β}	0.0701	[82]
I_{xz}	0 slug ft^2	xz Product of Inertia	[82]	C_{l_p}	-0.410	[82]
I_{xy}, I_{yz}	0 slug ft^2	Other Products of Inertia	[30]	C_{n_p}	0.0575	[82]
S	184 ft^2	Wing Planform Area	[82]	C_{l_r}	0.107	[82]
b	33.4 ft	Wing Span	[82]	C_{n_r}	-0.125	[82]
$\bar{c}$	5.7 ft	Mean Chord	[82]	$C_{z_{\delta_e}}$	-0.355	[82]*
e	0.8	Oswald Efficiency Factor	[33]	$C_{m_{\delta_e}}$	-0.889	[82]*
a	0.6	Air Density Exponent	[33]	$C_{l_{\delta_a}}$	0.1342	[82]
$P^s_{\max}$	290 hp	Maximum Engine Power	[33]	$C_{n_{\delta_a}}$	-0.00346	[82]
$C_{L_{\max}}$	2.4	Maximum Coefficient of Lift	[33]	$C_{y_{\delta_r}}$	0.157	[82]
$n_{\max}$	2	Maximum Load Factor	[33]	$C_{l_{\delta_r}}$	0.0118	[82]
η	0.8	Propeller Efficiency	[33]	$C_{n_{\delta_r}}$	-0.0717	[82]
C_{L_0}	0.36		[82]*	C_{y_p}	0	
C_{D_0}	0.039		[82]*	C_{y_r}	0	
C_{L_α}	4.44		[82]	C_{z_q}	0	
C_{D_α}	0.33		[82]	$\frac{dC_D}{dM}$†	0	[31]
C_{m_α}	-0.683		[82]	$\frac{dC_m}{dM}$†	0	[31]

* Computed from other parameters given in [33] and [82].
† M denotes the Mach number.

Navion

Section 5.3's numerical example uses a Navion general aviation aircraft model from Teper [82]. Table C.1 summarizes the necessary airplane parameters. This source's parameters correspond to steady level longitudinal flight at mean sea level with Mach number 0.158. For parameters not specified in Teper [82], the example uses the value given in McClamroch's [33] general aviation aircraft model. The last five parameters in the table are not given in either source. The last two are based on a plot for a different airplane in Roskam [31]. The remaining three parameters did not appear to affect the results and were set to zero. The stall boundaries of the resulting flight envelopes are generally consistent with the stall speeds listed in the Navion manual [83].

Other Aircraft

Figures 1.1 and 4.9–4.11 include results for several other aircraft. Beard and McClain [12] provide the Aerosonde model. Teper [82] provides the F-104, and A-4D models. Heffley and Jewell [84] provide the Lockheed Jetstar, Convair 880, Boeing 747, and C-5A models. MacDonald et al. [85] provide the de Havilland Canada DHC-5 Buffalo model. The Aerosonde model does not give a reference flight state. A reference airspeed of 60 kts is chosen as its cruise airspeed based on manufacturer's specifications [86]. The C-5A model used is for sea level at Mach 0.45. The Buffalo model used is for sea level at 215 ft/s. The remaining aircraft models, including the Navion, are reproduced in Appendix B of Nelson [30], and Chap. IV uses the sea level flight states listed in that text. For all of these models except the Aerosonde and the Buffalo, C_L, C_D, C_{L_α}, and α are given for the reference flight state of the model, but Chap. IV requires C_{D_0}. C_{D_0} is computed for each aircraft from the drag polar in McClamroch [33],

$$C_D = C_{D_0} + \frac{SC_L^2}{\pi e b^2}. \tag{C.5}$$

For all of the aircraft, the analysis required a value for the Oswald efficiency factor e in order to compute the coefficient for induced drag in the drag polar. This parameter is rarely provided, though the Buffalo model gives it as 0.75. This dissertation uses the value 0.8 for all of the other aircraft, including the GTM and T2.

Relevance of Unsteady Effects

Hoblit shows that, in the short period approximation, the dimensionless parameter $\bar{c}/\delta_{sp}$ is a measure of the importance of unsteady effects in turbulence response [15]. δ_{sp} is defined in Eq. (4.24) for the short period approximation. Here we posit a phugoid analog of δ_{sp},

$$\delta_p \triangleq \frac{2m}{\rho S C_L}, \tag{C.6}$$

Table C.2: Dimensionless parameters for the airplanes in Fig. 4.9.

Airplane	κ	Scaled GTM's κ	ζ_p	$\bar{c}/\delta_p$
T2	5.5	1.7	0.050	0.0027
Aerosonde	3.9	1.2	0.078	0.0013
F-104	1.7	0.52	0.30	0.0088
A-4D	1.4	0.41	0.14	0.0080
Navion	1.1	0.34	0.12	0.0035
Jetstar	0.70	0.21	0.091	0.0041
Buffalo	0.39	0.12	0.10	0.0021
Convair 880	0.31	0.094	0.14	0.0032
GTM	0.30	0.30	0.044	0.0027
Boeing 747	0.19	0.058	0.080	0.0028
C-5A	0.17	0.052	0.092	0.0028

based on the way the lift coefficient enters the two approximations.

Table C.2 shows the values of the relevant non-dimensional parameters for the eleven airplane models used in Fig. 4.9. The last column of Table C.2 lists the values for $\bar{c}/\delta_p$. Hoblit shows that for values of $\bar{c}/\delta_{sp} \leq 0.010$, the gust response does not change significantly due to unsteady effects. Since each of the airplanes listed in Table C.2 has a value for $\bar{c}/\delta_p$ that is less than 0.010, unsteady effects are not expected for any combination of airplane and flight state considered in this dissertation.

Atmosphere & Wind

For the air density and speed of sound in air, this dissertation follows the U.S. Standard Atmosphere model [34] by using a calculator provided in McClamroch [33]. For the Dryden and von Kármán gusts, this dissertation adheres to the MIL-HDBK-1797 specifications [19] and the filters given in the MATLAB documentation [67, 75]. The turbulence intensity and scale length vary with altitude. Since the high altitude turbulence intensity must be read off of a chart, some discretion had to be used in choosing values. For moderate turbulence, we choose $\sigma_u = 5$ ft/s at 35,000 ft and

Table C.3: Turbulence parameters used in Section 5.3. Values are given in the source's units.

Symbol	Value	Name	Ref.
D	$\mathbb{1}_6$	Noise Covariance Matrix	[67]
σ_u	10 ft/s	Longitudinal Turbulence Intensity	[19]
σ_v, σ_w	σ_u	Other Turbulence Intensities	[19]
L_u	1,750 ft	Longitudinal Turbulence Scale Length	[19]
L_v, L_w	$\frac{L_u}{2}$	Other Turbulence Scale Lengths	[19]

$\sigma_u = 9$ ft/s at 2,000 ft. The U.S. Standard Atmosphere model uses altitude above mean sea level while the turbulence models use altitude above ground level. For convenience, this dissertation assumes that the ground is at sea level.

In Chap. V, the same turbulence parameters are used in all of the examples that use the Dryden model for gusts. The parameters are listed in Table C.3

BIBLIOGRAPHY

BIBLIOGRAPHY

[1] "Review of Aviation Accidents Involving Weather Turbulence in the United States," National Aviation Safety Data Analysis Center, Federal Aviation Administration, Washington, DC, 2004.

[2] Belcastro, C. M. and Foster, J. V., "Aircraft Loss-of-Control Accident Analysis," *AIAA Guidance, Navigation, and Control Conference,* Toronto, Canada, 2010.

[3] "Statistical Summary of Commercial Jet Airplane Accidents," Boeing Commercial Airplanes, Seattle, WA, 2010.

[4] "Brief of Accident," ERA10LA506, National Transportation Safety Board, Washington, DC, 2012.

[5] "Brief of Accident," DFW07FA004, National Transportation Safety Board, Washington, DC, 2007.

[6] "Air Operators Utilization Reports," Aviation Data Systems Branch, Federal Aviation Administration, Washington, DC, 2001.

[7] "General Aviation and Air Taxi Activity (GAATA) Survey CY2001," Statistics and Forecasts Branch, Federal Aviation Administration, Washington, DC, 2001.

[8] *Unmanned Aircraft Systems: Comprehensive Planning and a Results-Oriented Training Strategy Are Needed to Support Growing Inventories*, GAO-10-331, Government Accountability Office, Washington, DC, 2010.

[9] *Umnanned Aircraft Systems Roadmap 2005-2030*, Office of the Secretary of Defense, Dept. of Defense, Washington, DC, 2005.

[10] *Pilot/Controller Glossary*, Federal Aviation Administration, Washington, DC, 2011.

[11] Cox, T. H., Nagy, C. J., Skoog, M. A., Somers, I. A., and Warner, R., "A Report Overview of the Civil UAV Capability Assessment," Draft Report, Civil UAV Team, NASA, Edwards, CA, 2005.

[12] Beard, R. W. and McLain, T. W., *Small Unmanned Aircraft: Theory and Practice*, Princeton University Press, Princeton, 2012, pp. xi, 275–276.

[13] Morelli, E. A. and Cunningham, K., "Aircraft Dynamic Modeling in Turbulence," *AIAA Atmospheric Flight Mechanics Conference,* Minneapolis, MN, 2012.

[14] Nguyen, N., Nelson, A., and Pulliam, T., "Damage Adaptive Control System Research Report," Internal Report, NASA, Moffett Field, CA, 2006.

[15] Hoblit, F. M., *Gust Loads on Aircraft: Concepts and Applications*, American Institute of Aeronautics and Astronautics, Inc., Washington, DC, 1988.

[16] Houbolt, J. C., "Atmospheric Turbulence," *AIAA Journal*, Vol. 11, No. 4, 1973, pp. 421–437.

[17] Etkin, B., "Turbulent Wind and Its Effect on Flight," *Journal of Aicraft*, Vol. 18, No. 5, 1981, pp. 327–345.

[18] "Airworthiness Standards: Transport Category Airplanes," *U.S. Code of Federal Regulations*, 14 CFR Part 25, Appendix G, Government Printing Office, Washington, DC, 2011.

[19] *Flying Qualities of Piloted Aircraft*, MIL-HDBK-1797, Dept. of Defense, Washington, DC, 1997, pp. 673–695.

[20] Etkin, B., *Dynamics of Atmospheric Flight*, Dover Publications, Mineola, NY, 2005, pp. 529–556.

[21] Dodds, C. J. and Robson, J. D., "The Description of Road Surface Roughness," *Journal of Sound and Vibration*, Vol. 31, No. 2, 1973, pp. 175–183.

[22] Bishop, R. E. and Price, W. G., *Hydroelasticity of Ships*, Cambridge University Press, London, 1979, pp. 326–387.

[23] Lloyd, A. J., *Seakeeping: Ship Behavior in Rough Weather*, Chichester, West Sussex, England, 1989, pp. 93–120.

[24] Liepmann, H. W., "On the Application of Statistical Concepts to the Buffeting Problem," *Journal of the Aeronautical Sciences*, Vol. 19, No. 12, 1952, pp. 793–800.

[25] Diedrich, F. W. and Drischler, J. A., "Effect of Spanwise Variations in Gust Intensity on the Lift Due to Atmospheric Turbulence," NACA TN 3920, 1957.

[26] de Kármán , T. and Howarth, L., "On the Statistical Theory of Isotropic Turbulence," *Proceedings of the Royal Society of London. Series A, Mathematical and Physical Sciences*, Vol. 164, No. 917, 1938, pp. 192–215.

[27] von Kármán , T., "Progress in the Statistical Theory of Turbulence," *Proceedings of the National Academy of Sciences*, Vol. 34, No. 11, 1948, pp. 530–539.

[28] von Kármán , T. and Lin, C. C., "*On the Statistical Theory of Isotropic Turbulence*," von Mises, R. and von Kármán , T., eds., Advances in Applied Mechanics, Academic Press, Inc., New York, Vol. 2, pp. 1–19, 1951.

[29] Etkin, B. and Reid, L. D., *Dynamics of Flight: Stability and Control*, John Wiley & Sons, Inc., New York, 3rd ed., 1996, pp. 259–302.

[30] Nelson, R. C., *Flight Stability and Automatic Control*, WCB/McGraw–Hill, Boston, 2nd ed., 1998, pp. 101–127, 398–419.

[31] Roskam, J., *Airplane Flight Dynamics and Automatic Flight Controls*, Vol. 1, Design, Analysis, and Research Corporation, Lawrence, KS, 2003, pp. 53–236.

[32] Stengel, R. F., *Flight Dynamics*, Princeton University Press, Princeton, 2004, pp. 29–272, 457–473.

[33] McClamroch, N. H., *Steady Aircraft Flight and Performance*, Princeton University Press, Princeton, 2011.

[34] *U.S. Standard Atmosphere, 1976*, NOAA-S/T 76-1562, National Oceanic and Atmospheric Administration, Washington, DC, 1976, pp. 21–27.

[35] Gibbings, J. C., *Dimensional Analysis*, Springer-Verlag, London, 2011, pp. 83–93.

[36] Szirtes, T. and Rózsa, P., *Applied Dimensional Analysis and Modeling*, Elsevier/Butterworth-Heinemann, Amsterdam, 2nd ed., 2007, pp. 317–320, 463–525.

[37] Buckingham, E., "On Physically Similar Systems; Illustrations of the Use of Dimensional Equations," *Physical Review*, Vol. 4, No. 4, 1914, pp. 345–376.

[38] Wolowicz, C. H., Bowman, J., James S., and Gilbert, W. P., "Similitude Requirements and Scaling Relationships as Applied to Model Testing," NASA 1435, 1979.

[39] White, F. M., *Fluid Mechanics*, McGraw Hill, New York, 5th ed., 2003, pp. 293–340.

[40] Newman, J. N., *Marine Hydrodynamics*, MIT Press, Cambridge, MA, 1977, pp. 8–46.

[41] Ryutov, D. D., Remington, B. A., Robey, H. F., and Drake, R. P., "Magnetohydrodynamic Scaling: From Astrophysics to the Laboratory," *Physics of Plasmas*, Vol. 8, No. 5, 2001, pp. 1804–1816.

[42] Mettler, B., Tischler, M. B., and Kanade, T., "System Identification of Small-Size Unmanned Helicopter Dynamics," *American Helicopter Society 55th Forum,* Montreal, Canada, 1999.

[43] Burk, J., Sanger M. and Wilson, J., Calvin F., "Radio-Controlled Model Design and Testing Techniques for Stall/Spin Evaluation of General-Aviation Aircraft," *SAE National Business Aircraft Meeting,* Wichita, KS, 1975.

[44] Jordan, T. L., Langford, W. M., and Hill, J. S., "Airborne Subscale Transport Aircraft Research Testbed - Aircraft Model Development," *AIAA Guidance, Navigation, and Control Conference,* San Francisco, CA, 2005.

[45] Tennekes, H., *The Simple Science of Flight: From Insects to Jumbo Jets*, The MIT Press, Cambridge, MA, 2009, p. 15.

[46] Lighthill, J., "Introduction to the Scaling of Aerial Locomotion," Pedley, T. J., ed., *Scale Effects in Animal Locomotion*, Academic Press, Inc., London, pp. 365–404, 1977.

[47] Schmidt-Nielsen, K., *Scaling: Why is animal size so important?*, Cambridge University Press, Cambridge, England, 1984, pp. 7–20.

[48] Norberg, U. M., *Vertebrate Flight*, Springer-Verlag, Berlin, 1990, pp. 166–179.

[49] Pennycuick, C. J., *Newton Rules Biology*, Oxford University Press, New York, 1992, pp. 40–62.

[50] Shyy, W., Lian, Y., Tang, J., Viieru, D., and Liu, H., *Aerodynamics of Low Reynolds Number Flyers*, Cambridge University Press, New York, 2008, pp. 14–20, 44–57.

[51] Liu, T., "Comparative Scaling of Flapping- and Fixed-Wing Flyers," *AIAA Journal*, Vol. 44, No. 1, 2006, pp. 24–33.

[52] Phillips, W. H. and Kraft Jr., C. C., "Theoretical study of some methods for increasing the smoothness of flight through rough air," NACA TN-2416, 1951.

[53] McClean, R., "The optimization of an autopilot for an airplane subjected to random atmospheric turbulence," UTIA Technical Note No. 45, Institute of Aerophysics, University of Toronto, Toronto, 1960.

[54] Burris, P. M. and Bender, M. A., "Aircraft load alleviation and mode stabilization (LAMS)," AFFDL-TR-68-164, Air Force Flight Dynamics Laboratory, 1969.

[55] Rynaski, E. G., Andrisani II, D., and Eulrich, B. J., "Gust Alleviation Using Direct Turbulence Measurements," *AIAA Atmospheric Flight Mechanics Conference for Future Space Systems,* Boulder, CO, 1979, pp. 379–386.

[56] Rynaski, E. G., "Gust Alleviation – Criteria and Control Laws," *AIAA Atmospheric Flight Mechanics Conference for Future Space Systems,* Boulder, CO, 1979, pp. 387–392.

[57] Sato, M., Yokoyama, N., and Satoh, A., "Disturbance suppression via robust MPC using prior disturbance data: Low computational complexity method," *IEEE International Conference on Control and Automation,* Shanghai, China, 2009, pp. 2176–2181.

[58] Davison, D. E., Kabamba, P. T., and Meerkov, S. M., "Robustness with Respect to Disturbance Model Uncertainty: Theory and Application to Autopilot Performance Analysis," *Mathematical Problems in Engineering*, Vol. 6, 2000, pp. 267–304.

[59] Dietz, S. G., Scherer, C. W., and Koroglu, H., "Robust control against disturbance model uncertainty: a convex solution," *46th IEEE Conference on Decision and Control,* New Orleans, LA, 2007, pp. 842–847.

[60] Horowitz, I. M., *Quantitative Feedback Design Theory (QFT)*, QFT Publications, Boulder, CO, 1993, pp. 37–78.

[61] Reynolds, O. R., Pachter, M., and Houpis, C. H., "Full Envelope Flight Control System Design Using Qualitative Feedback Theory," *Journal of Guidance, Control, and Dynamics*, Vol. 19, No. 1, 1996, pp. 23–29.

[62] Wu, S.-F., Grimble, M. J., and Wei, W., "QFT-Based Robust/Fault-Tolerant Flight Control Design for a Remote Pilotless Vehicle," *IEEE Transactions on Control Systems Technology*, Vol. 8, No. 6, 2000, pp. 1010–1016.

[63] Richardson, J. R., Atkins, E. M., Kabamba, P. T., and Girard, A. R., "Envelopes for Flight Through Stochastic Gusts," *AIAA Atmospheric Flight Mechanics Conference,* Portland, OR, 2011.

[64] Richardson, J. R., Atkins, E. M., Kabamba, P. T., and Girard, A. R., "Envelopes for Flight Through Stochastic Gusts," *Journal of Guidance, Control, and Dynamics*, accepted Nov., 2012.

[65] Richardson, J. R., Atkins, E. M., Kabamba, P. T., and Girard, A. R., "Scaling of Airplane Dynamic Response to Stochastic Gusts," *Journal of Aircraft*, submitted Mar., 2013.

[66] Kuipers, J. B., *Quaternions and Rotation Sequences: A Primer with Applications to Orbits, Aerospace, and Virtual Reality*, Princeton University Press, Princeton, NJ, 1999, p. 85.

[67] "Dryden Wind Turbulence Model (Continuous)," *MATLAB Reference Pages*, The MathWorks, Inc., Natick, MA, 2010.

[68] Davis, M. H. A. and Vinter, R. B., *Stochastic Modelling and Control*, Chapman and Hall, Cambridge, England, 1985, pp. 87–89.

[69] Jordan, T. L., Foster, J. V., Bailey, R. M., and Belcastro, C. M., "AirSTAR: A UAV Platform for Flight Dynamics and Control System Testing," *25th AIAA Aerodynamic Measurement Technology and Ground Testing Conference,* San Francisco, CA, 2006.

[70] Magnan, A., *La Locomotion Chez Les Animaux I: Le Vol Des Insectes*, Hermann & Cie., Paris, 1934, p. 8.

[71] *Information Manual: Skyhawk SP*, Cessna Aircraft Company, Wichita, KS, 2007, pp. 4-3, 4-43.

[72] Meerkov, S. M. and Runolfsson, T., "Aiming Control," *Proceedings of the 25th Conference on Decision and Control,* Athens, Greece, 1986.

[73] Meerkov, S. M. and Runolfsson, T., "Output Aiming Control," *Proceedings of the 26th Conference on Decision and Control,* Los Angeles, CA, 1987.

[74] Ching, S., Eun, Y., Gokcek, C., Kabamba, P. T., and Meerkov, S. M., *Quasilinear Control*, Cambridge University Press, New York, 2011, pp. 66–113.

[75] "von Karman Wind Turbulence Model (Continuous)," *MATLAB Reference Pages*, The MathWorks, Inc., Natick, MA, 2010.

[76] Rice, S. O., "Mathematical Analysis of Random Noise," *Bell System Technical Journal*, Vol. 24, No. 1, 1945, pp. 46–156.

[77] Leadbetter, M. R., Lindgren, G., and Rootzén, H., *Extremes and Related Properties of Random Sequences and Processes*, Springer-Verlag, New York, 1983, pp. 176, 238, 260.

[78] Feller, W., *An Introduction to Probability Theory and Its Applications*, Vol. 1, John Wiley & Sons, Inc., New York, 3rd ed., 1967, pp. 446–448.

[79] Nguyen, N., Krishnakumar, K., Kaneshige, J., and Nespeca, P., "Dynamics and Adaptive Control for Stability Recovery of Damaged Asymmetric Aircraft," *AIAA Guidance, Navigation, and Control Conference,* Keystone, CO, 2006.

[80] Nguyen, N., Krishnakumar, K., Kaneshige, J., and Nespeca, P., "Flight Dynamics and Hybrid Adaptive Control of Damaged Aircraft," *Journal of Guidance, Control, and Dynamics*, Vol. 31, No. 3, 2008, pp. 751–764.

[81] Cashman, J. E., Kelly, B. D., and Nield, B. N., "Operational Use of Angle of Attack on Modern Commercial Jet Airplanes," *Aero Magazine*, Vol. 12, 2000, pp. 10–22.

[82] Teper, G. L., "Aircraft Stability and Control Data," NASA CR-96008, 1969.

[83] *Navion Operation Manual*, Ryan Aeronautical Company, San Diego, CA, 1950, p. 51.

[84] Heffley, R. K. and Jewell, W. F., "Aircraft Handling Qualities Data," NASA CR-2144, 1972.

[85] MacDonald, R. A., Garelick, M., and O'Grady, J., "Linearized Mathematical Models for de Havilland Canada Buffalo & Twin Otter STOL Transports," DOT-TSC-FAA-71-8, Department of Transportation Transportation Systems Center, Cambridge, MA, 1971.

[86] "Aerosonde® Mark 4.7: Redefining Expeditionary," AAI Coroporation, Hunt Valley, MD, 2010.